Southern Regional Center for Lightweight Innovative Design

Phase IV

Quarterly Report

January – March 2012

For compliance with contract requirements of
Award DE-FC26-06NT42755

Submitted April 30, 2012

MISSISSIPPI STATE UNIVERSITY

Southern Regional Center for Lightweight Innovative Design

Phase IV
Quarterly Report
January – March 2012

For compliance with contract requirements of
Award DE-FC26-06NT42755

TASK 1
MULTISCALE MATERIAL MODELS AND DESIGN FRAMEWORK FOR LIGHTWEIGHT ALLOYS (MAGNESIUM & ALUMINUM)

Submitted April 30, 2012

TABLE OF CONTENTS

Center for Advanced Vehicular Systems, Mississippi State University

Date: April 30, 2012

From: Paul Wang, Mark Horstemeyer

RE: SRCLID Phase IV Quarterly Report – January-March 2012

TASK 1: MULTISCALE MATERIAL MODELS AND DESIGN FRAMEWORK FOR LIGHTWEIGHT ALLOYS (MAGNESIUM AND ALUMINUM)

Principal Investigator: Paul Wang
Associate Director, CAVS
Mississippi State University (MSST)
200 Research Blvd
Mississippi State, MS 39762
(662) 325-5454; fax: (662) 325-5433; e-mail: pwang@cavs.msstate.edu

Carol Schutte: Technology Area Development Manager
e-mail: carol.schutte@ee.doe.gov

Joseph Renk
email: joseph.renk@netl.doe.gov

Contractor: *Mississippi State University (MSST)*
Contract No.: *DE-FC26-06NT42755*

SUBTASK 1.1: MULTIPHYSICS AND MULTISCALE BASED INTERNAL STATE VARIABLE MATERIAL MODEL FOR SIMULATING DIFFERENT MANUFACTURING PROCESSES

***Team Members: P. Wang**, S. Felicelli, M.F. Horstemeyer, D.J. Bammann, E.B. Marin, H. El Kadiri, Y. Hammi, C. Bouvard, A. Oppedal, P. Gullett, P. Wang, Q. Ma, H. Grewal (PhD student), N. Bratton (MS student), S. Hossein (PhD student), R. Potula (MS student), J. Kapil (MS student), PhD student (GRA, Hammi), Z. Mcclelland(UGR), S. Bhandari(GRU), G. Long().*

SUMMARY OF THE PROGRESS

Dynamic Recrystallization Mechanisms Study in AM30 Compressed at 450℃

Due to magnesium extrusion always conducts at high temperatures, e.g. usually at 350-450 °C, the dynamic recrystallization (DRX) certainly occurs during extrusion at high temperature. As such, DRX surely alter final microstructure and texture of the Mg product, and in turn plays vital role on mechanical property of the product. Even extensively DRX nucleation mechanisms have been investigated in literature, how the orientations change in the DRX grains during larger straining still need to deep understand. In this study, we performed uniaxial compression in an extruded AM30 billet along the extrusion direction to large strain levels at strain rate of 0.8 s^{-1}. Due to the typical {0001} rod texture

in the extruded AM30, at small strain, the prismatic slip dominated plasticity in the parent grain based on EBSD technique as shown in Figure 1. Figure 1 clearly shows that prismatic dominates plasticity in AM30 alloy at 450 °C, 0.8 s^{-1}. The profuse prismatic slip configuration in an extruded ZK60 was also observed by Li et al. (2008) using TEM. In addition, the pyramidal slip has to activate around parent grain to accommodate the strain compatibility of polycrystal due to the prismatic slip just has two independent slip systems. The activation of pyramidal surely promote the nucleation in the vicinity of parent grain and result in "necklace" DRX grains as shown in figure 1.

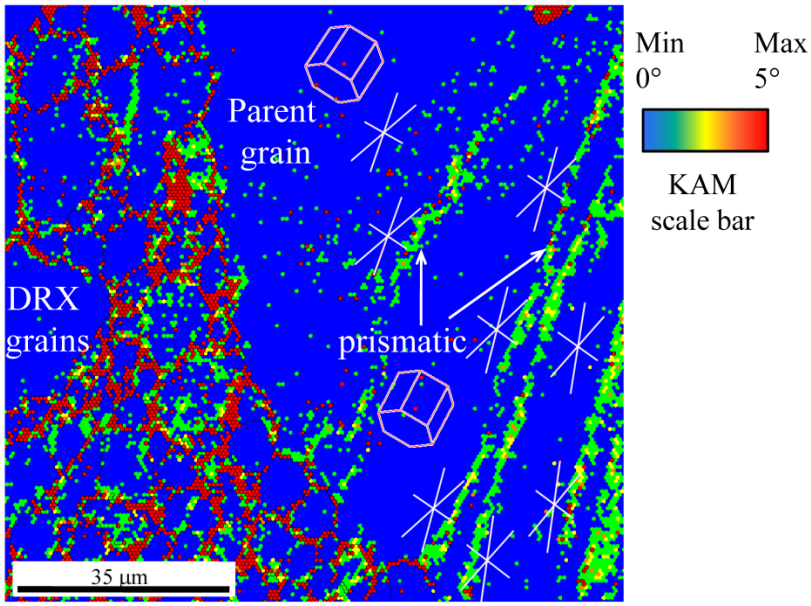

Figure 1. EBSD Kernel average misorientation (KAM) map and prismatic <a> slip trace analysis in ED sample at 450°C 0.8 s^{-1}, ε=-0.04. The red hexagons show the parent grain orientation; the white stars represent the $\{10\bar{1}0\}$ plane traces and the thin black lines are the large angle grain boundaries with misorienation >15°. The slip traces prove the prismatic slip mainly activated in the parent grain

At larger strain level, prismatic no longer dominate the plasticity. Basal and two kinds of pyramidal slips, namely $\{10\bar{1}1\}<10\bar{1}2>$ first pyramidal slip and $\{11\bar{2}2\}<11\bar{2}\bar{3}>$ second pyramidal slip, dominate the plasticity in the DRX grains. Figure 2 presents the DRX grains' inverse pole figure map and the simulation texture based on different kinds of pyramidal slips and basal slip. As shown in Figure 2, combination of pyramidal slips and basal slip could activate and result in the specific texture in the inverse pole figure. The combination of basal and the secondary pyramidal slip dominate plasticity in the <0001> ED grains, while the combination of basal and the first pyramidal slip should activate in other grains. In comparison with the measured and predicted inverse pole figures of ED in Figure 2, the active slip systems in the DRX indeed govern the DRX texture evolution. In addition, twinning also occurred at high temperature of 450 °C as shown in the EBSD IPF map in Figure 2 (the red "island" is the twin). Twinning propagated also at initial strain and then twins were invaded by DRX grains. Thus, heavy in-coherent twin boundaries can be observed in this study (Figure 2a). Twinning and the active slip systems dominate the texture evolution in the DRX grains. Based on these observations, the strain induced boundary migration (SIBM) is the main DRX grains growth mechanism in this AM30 simply compressed at 450 °C.

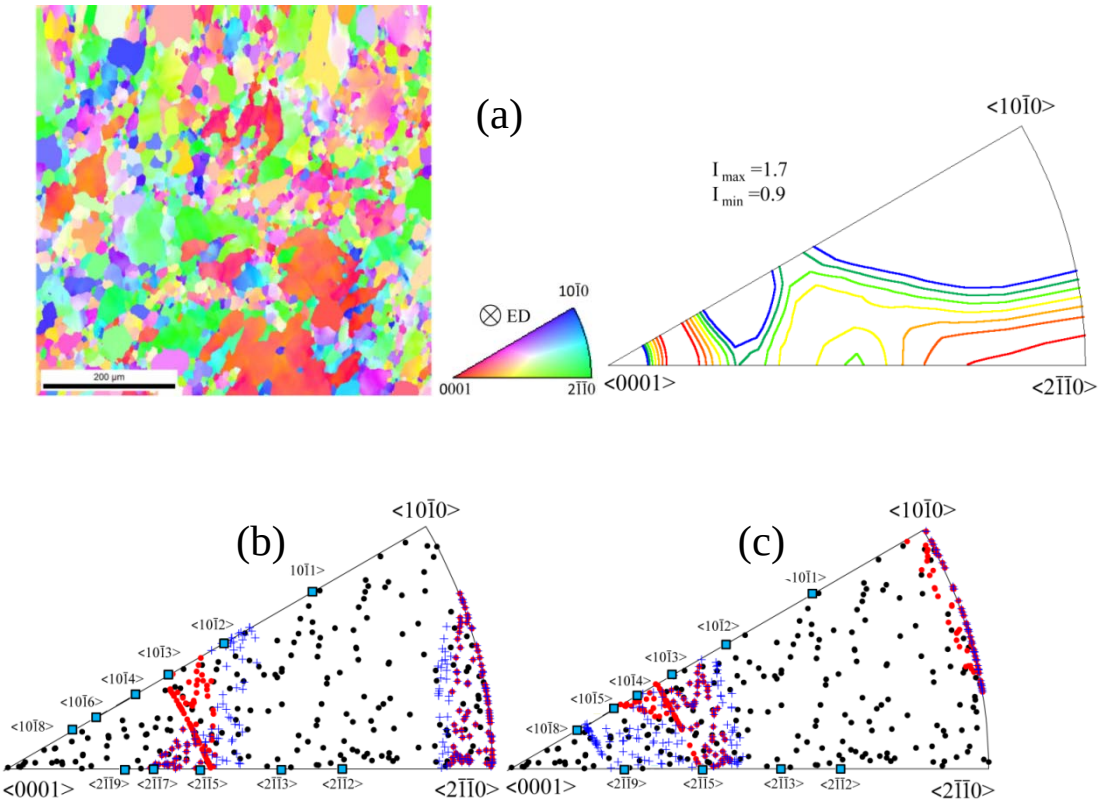

Figure 2. (a) Microtexture and inverse pole figure of compression direction in AM30 compression along the extrusion direction at 450 °C, 0.8 s^{-1}, ε=-0.60; (b) the initial representative 200 grains and the simulated deformation orientations using Sachs model after compression ε=-0.5 using the combination of basal and {10$\bar{1}$1}<10$\bar{1}$2> first pyramidal slip and a step size of -0.001; and (c) the simulated deformation orientations based on Sachs model after compression ε=-0.5 using the combination of basal and {11$\bar{2}$2}<11$\bar{2}\bar{3}$> second pyramidal slip and a step size of -0.001. The black dots are the initial orientations; the red dots represent the deformed orientations with CRSS ratio of <c+a> and basal is 1:1; the blue cross represent the case of CRSS ratio of <c+a> and basal is 2; and the squares are the typical crystal directions

Post Forming Analysis on AM30

To further develop our extrusion and simulation capabilities, a laboratory-scale indirect-extrusion process was used to form AM30 extrudate to mechanically test the stress-strain behavior and analyze the texture via x-ray diffraction. Samples were extruded in a circular profile 0.25 and 0.50 in. diameter. The results presented here are the 0.50 in. diameter; previous quarterly reports documented the 0.25 in. Testing was possible in the ED (extrusion direction) and ERD (extrusion radial direction) because of the larger sample size.

In addition to the mechanical tests to failure, interrupted testing at intermediate strain levels were conducted. The interrupted strain levels correspond roughly to half the failure strain levels. In the case of the ED loading, corresponding to deformation by profuse twinning, the interrupted strain level corresponds to the strain level where twinning has saturated, and rapid hardening by slip deformation occurs.

The ram speeds (20 and 40 mm/min) were selected to provide an average strain rate comparable to the production extrusion. Following Atwell and Barnett [2], the average extrusion rate is:

$$\dot{\varepsilon} = \frac{9.6R^{0.6}V_R}{D_b} = 0.15 \qquad 1)$$

where R is the extrusion ratio, V is the ram speed, and D_b is the diameter of the billet. The mechanical testing in these results correspond to extrusion ratio R = 6.

The extrudate was mechanically tested at strain rate = 0.001/s in uniaxial compression, at room temperature. The results are found in Figure 3. The ED loading direction produced a "sigmoidal" shaped curve, typical of deformation by profuse twinning. The yield point and initial loading were similar for each strain rate, but the strain hardening rate was higher after approximately 5% plastic strain, which corresponds to the maximum deformation that can be accommodated by twinning. Within each selected ram speed, higher strain hardening was observed at higher strain rates. The extrudate produced at the higher ram speed (40 mm/min) showed a higher overall saturation stress in each case. Samples of the unstrained materials were also analyzed by x-ray diffraction (Rigaku SmartLab) to obtain macro-texture information (Fig. 3). The recalculated pole figures are "prismatic", typical of extrusion process. The texture analysis was obtained using the MTEX software [3].

Work to simulate the mechanical testing by the VPSC (Visco-Plastic Self-Consistent) model [4] is in process. Interrupted strain tests will be performed to obtain texture measurements at intermediate strain levels to validate texture evolution simulations.

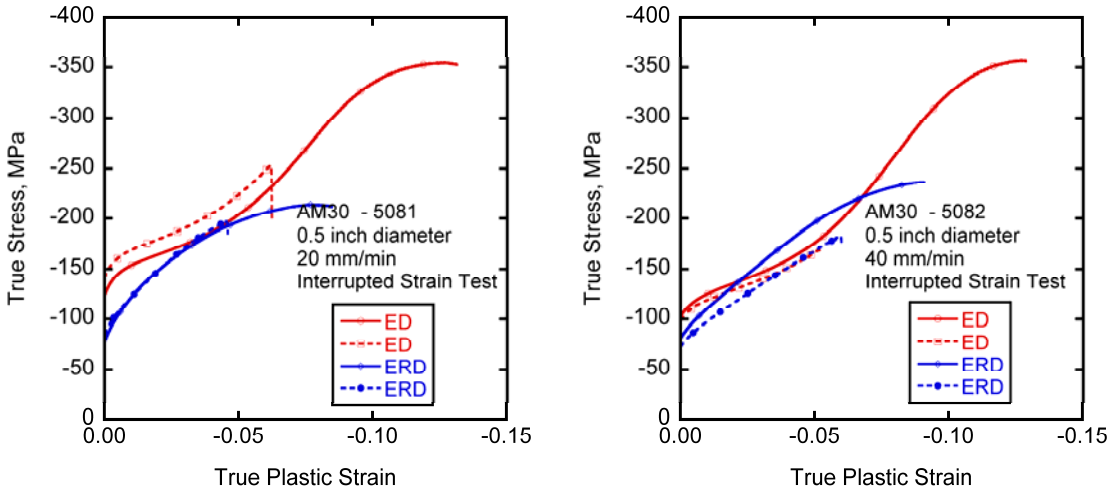

a) b)

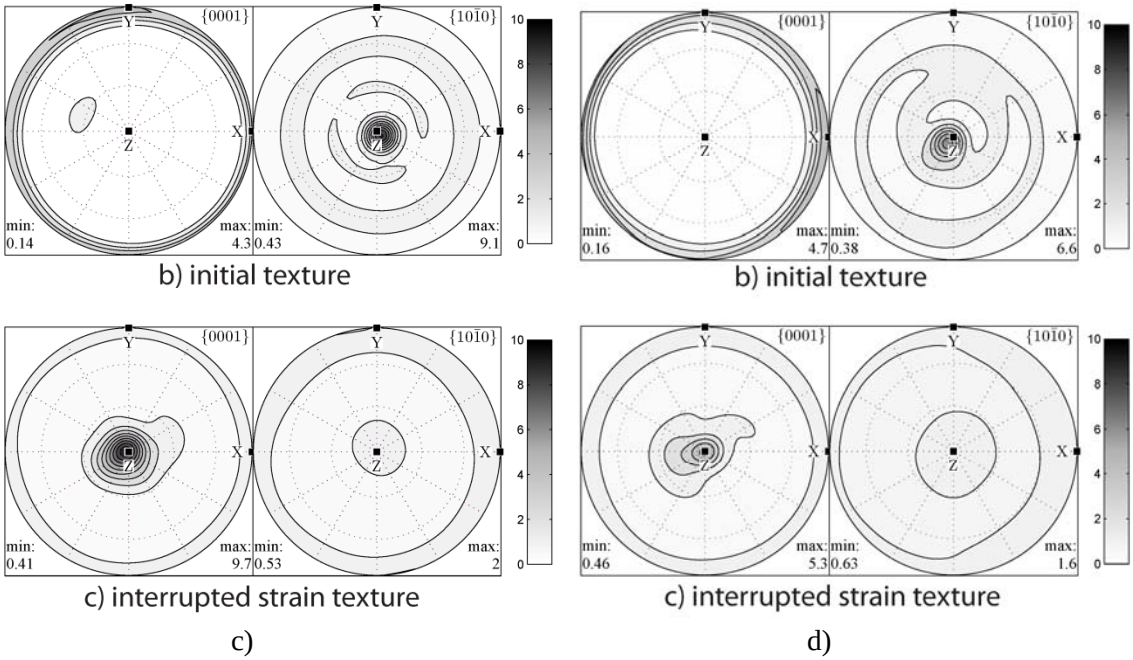

Figure 3. Stress-Strain behavior of AM30 Magnesium at strain rate = 0.001 /s and T= RT for two different ram speeds: a) ram speed = 20 mm/min and b) 40 mm/min. The x-ray diffraction pole figures of initial measured sample, and for interrupted testing in the ED direction (profuse twinning) for c) 20 mm/min and d) 40 mm/min.

Demo: Extruded Rail

The purpose of this chapter is to describe the ongoing work on the demo components. Regarding the extruded and as stated in previous quarterly reports, in the absence of the Computer Aided Design (CAD) of tooling for the extruded rail, we focus our work on the modeling of the extrusion process that lead to the double hat profile, also named Timminco Die. We will present a potential tooling CAD for the extruded rail of the demo structure next quarter.

Using the streamlines in the three representative positions in the double hat and VPSC dislocation density model and the corresponding hardening parameters which were obtained by stress-strain curves fitting can predict the texture and extrusion flow stress during extrusion using the Timmco double hat extrusion process simulation presented last quarter. The VPSC predicted texture and EBSD measured texture in the three positions in the double hat are shown in Figure 4.

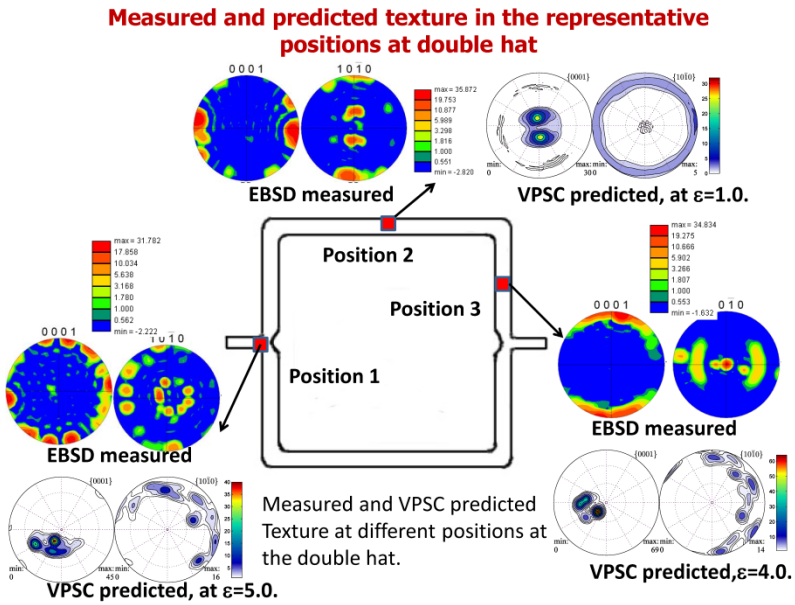

Figure 4. EBSD measured and VPSC predicted texture in different positions at the AM30 double hat.

In Figure 4, even if both measured and predicted texture intensity is very strong due to the severe plasticity during this double hat extrusion, the measured and predicted texture is different. In contrast to the case of flat die extrusion of AM30 in which the main predicted texture components by VPSC are in good agreement with EBSD measured texture. The main reason regarding the marked deviation is the non-consideration of the dynamic recrystallization in the present VPSC code even it has taken into the effect of temperature and strain rate. In the simple case of flat die, the effect of dynamic recrystallization may not be significant; however it could play marked roles during severe deformation, like the double hat extrusion case. This should be the future work to solve this problem.

Demo: Cast Shock Tower - AZ91

During this last quarter our main effort was dedicated to experimentally and numerically validate the cast shock tower received at CAVS. The goal was to numerically determine the failure location using a validated microstructure-property based material model [1].

An ABAQUS finite element (FE) mesh based on CAD (Computer Aided Design) data was provided by Optimal Inc. For the most of the part, the mesh was built by extruding the inner skin of the shock tower towards the exterior skin. The number of three elements in the thickness was maintained throughout the part. The provided CAD described an “ideal” part in terms of geometrical features.

After receiving the physical part, discrepancies between the CAD and the physical part were measured and further actions were taken to modify the FE mesh to account for these differences. The thickness in the “legs” was decreased to the thickness measured in these areas.

Figure 5 shows the load direction and boundary conditions on the shock tower. To get to these boundary conditions, several iterations revealed that without adding rotational freedom, the model was over constrained and highly stressed in the clamping areas. The two free rotations represented by the green arrows allowed a larger portion of the component to work under loading. No translations are

allowed along these two rotational axes. The load type applied to this structure is a displacement along the axis that is perpendicular to the rotational axes. The experimental fixture was considered to be rigid and was not modeled using FE.

The goal of this study is to determine failure location and load to failure using these boundary conditions, the magnitude is the one to failure.

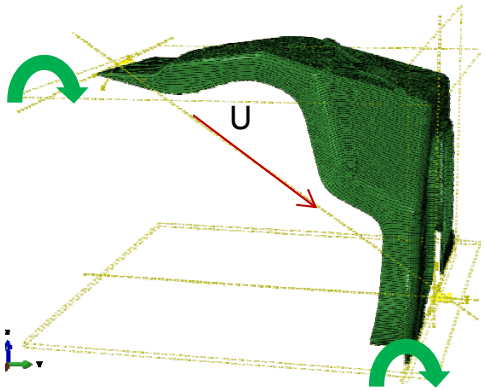

Figure 5. Load and boundary conditions on shock tower.

Regarding the material model, Table 1 shows the constants for the AZ91 magnesium alloy. These constants were determined in previous studies carried out at CAVS. Three constants were calibrated using a uniaxial tensile test on specimen extracted from the shock tower. These constants were related to the nucleation phenomena. Ref [1] describes specifically the meaning of each of these parameters.

Table 1. Plasticity-Damage State Dependent Variables (SDV) of user material subroutine UMAT.

Constant Definition	Value	Constant Definition	Value
Shear Modulus G_0	1.656E+04	Initial Temperature T_0	297
a	0	Heat generation coefficient	0.34
Bulk modulus K_0	49670	McClintock Damage Constant n	0.01
b	0	Initial Void Radius	2.00E-04
Melting Temperature	3000	Torsional constant a (nucleation)	0
BCJ Plasticity Parameters c_{01}	0	Tens/Comp constant b (nucleation)	0
BCJ Plasticity Parameters c_{02}	0	Triaxiality constant c (nucleation)	0
BCJ Plasticity Parameters c_{03}	42.9	Coeff. constant c (nucleation)	0
BCJ Plasticity Parameters c_{04}	349.4	Fracture Toughness K_{IC} (nucleation)	1
BCJ Plasticity Parameters c_{05}	1.00E-05	Average particle size (nucleation)	1
BCJ Plasticity Parameters c_{06}	0	Part. Vol. Fraction (nucleation)	1
BCJ Plasticity Parameters c_{07}	6.061E-03	Nearest Neighbor Distance (coalescence)	12
BCJ Plasticity Parameters c_{08}	43950	Chi exponent (coalescence)	1
BCJ Plasticity Parameters c_{09}	3220	Reference Dendrite Cell size DCS_0	30

BCJ Plasticity Parameters c_{10}	6.790	Dendrite Cell size DCS	30
BCJ Plasticity Parameters c_{11}	0	Dendrite Cell size zz	0.0509
BCJ Plasticity Parameters c_{12}	0	Initial Void Volume Fraction for CA	0.05
BCJ Plasticity Parameters c_{13}	3.983	BCJ Plasticity Parameters c_{21}	0
BCJ Plasticity Parameters c_{14}	39.02	BCJ Plasticity Parameters c_{22}	0
BCJ Plasticity Parameters c_{15}	12670	BCJ Plasticity Parameters c_{23}	0
BCJ Plasticity Parameters c_{16}	1.815	BCJ Plasticity Parameters c_{24}	0
BCJ Plasticity Parameters c_{17}	0	BCJ Plasticity Parameters c_{25}	0
BCJ Plasticity Parameters c_{18}	0	BCJ Plasticity Parameters c_{26}	0
BCJ Plasticity Parameters c_{19}	0	Nucleation Temperature Dependence	0
BCJ Plasticity Parameters c_{20}	0	Elastic Modulus Porosity Exponent β	0
BCJ Plasticity Parameters c_a	0	Flag to use vvfr.dat file	0
BCJ Plasticity Parameters c_b	0	Cacon	30

Ford provided the cooling time contours of the shock tower during its casting process. These maps were generated using the casting process simulation code MAGMA. Figure 6 shows these contours, the highest cooling time being yellow and the lowest being blue.

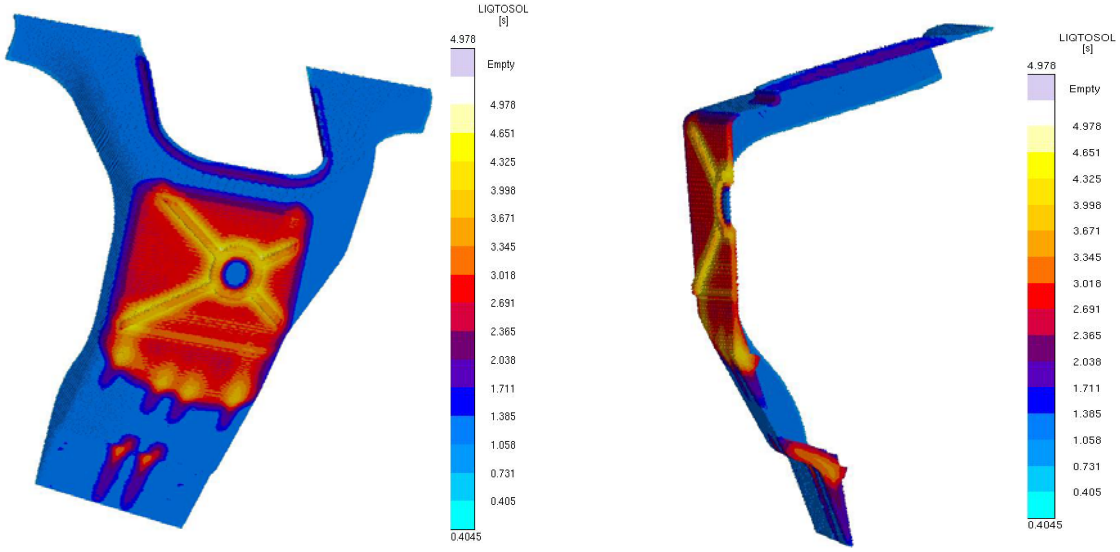

Figure 6. Simulated solidification time contours from Ford Inc.

It was also assumed that the longer it takes to cool, the higher the porosity fraction was. Based on this, the map in Figure 7 was built. The outer skin of the shock tower (in black) is considered to have very little porosity as it is a surface that was first in contact with the die during the casting process. The porosity measurements made in the ribs area (high porosity in orange and red) and in the fracture area (green) were also used to build this map. Finally the inner skin was set to a baseline initial porosity. Specifically, the map was built by the selection of various elements sets and the attribution of a porosity value to each of them.

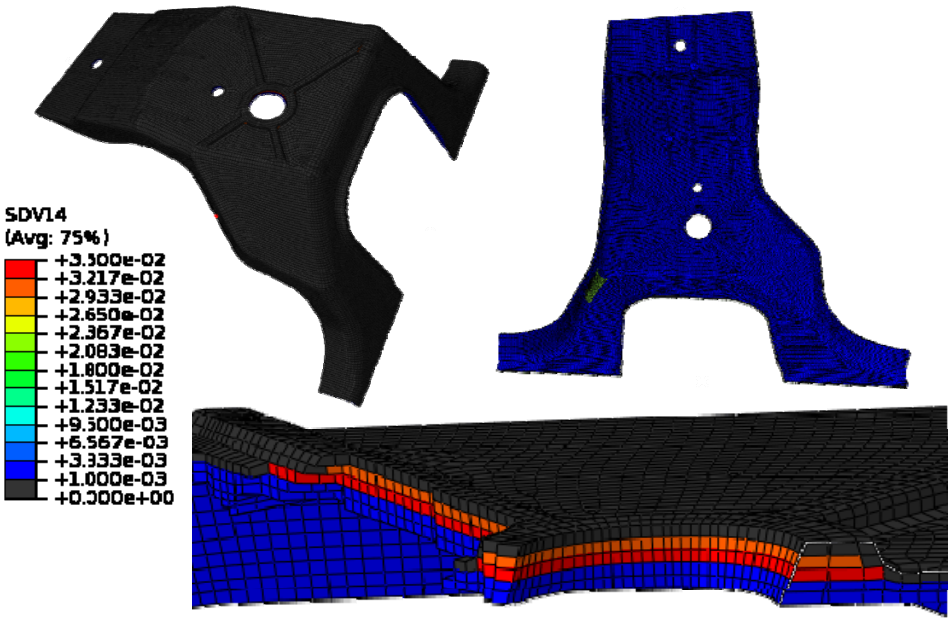

Figure 7. Porosity initial distribution through the thickness.

Figure 8 shows the damage contours in the shock tower at failure. The highest damage value is situated in one of the corner leg while the other side of the shock tower is less damaged.

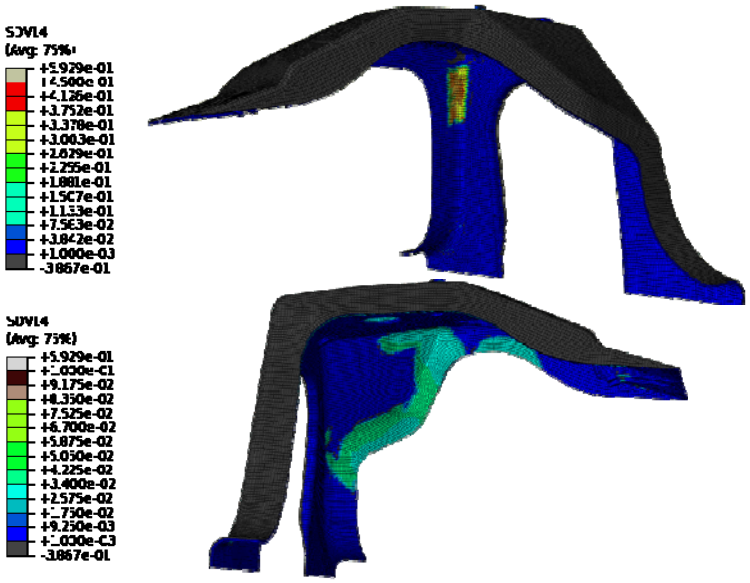

Figure 8. Damage contours of the shock tower.

Figure 9 shows a summary of the results in terms of initial porosity value, damage results and Von Mises results. Four key locations have been picked to describe the uniqueness of the results thanks to the internal state variable material model used in the simulation. In table 3 are the important features of these locations. Location A has the highest damage value under monotonic loading, location B has the

highest initial porosity fraction, location C has the highest stress concentration and location D is situated in an average range of value for strain, stress, porosity measurement and damage.

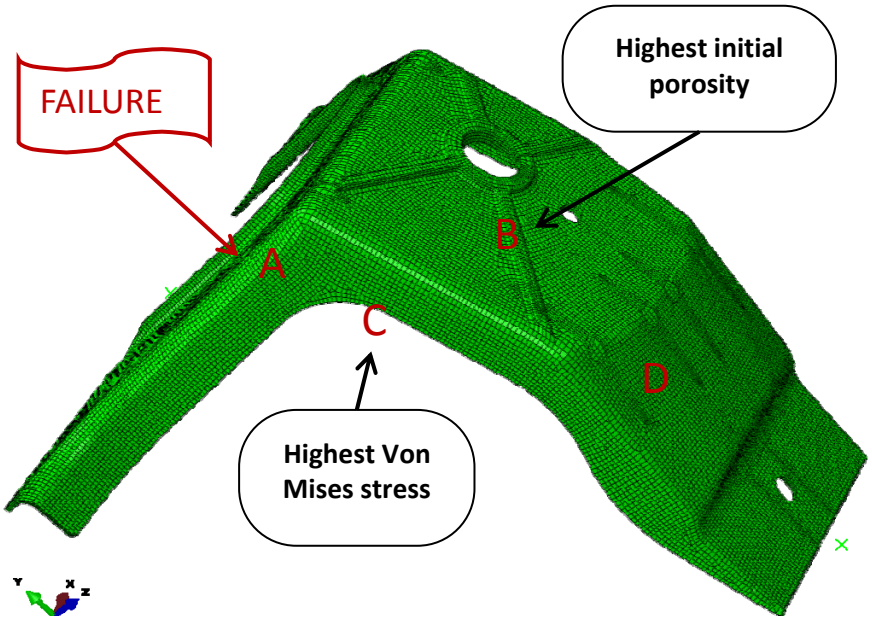

Figure 9. Locations of interest.

Table 2 shows a classification of these location based on output values of interest such at Von Mises Stress and Damage and initial porosity distribution. As we can see, depending on the variables we take into consideration, the failure location can drastically vary. For instance, from a material science point of view, we could assume that the failure location will be at the highest porosity area, hence B. After running a FEA and analyzing the stress distribution one can conclude that the failure location will be in the area of highest stress, hence C. But by using a material model that accounts for the initial microstructure of the material and has a damage evolution capability the failure location is in a very different place, hence location A.

Table 2. Results on shock tower.

	Mises Stress	Initial Porosity	Damage
Highest	**C**	**B**	**A**
↓	A	D	C
	B	A	D
Lowest	D	C	B
	↑	↑	↑
	Standard FEA answer	Standard Material Science Answer	Truth!

Due to the limited number of part available at CAVS, two shock towers were tested and both of the experiments provided good load and displacement data. Also, the failure locations were consistently situated in the same part area.

In terms of load-displacement behavior, Figure 10 shows the two plots from simulation results and experimental results respectively. As we can see, the physical testing of the part validated the simulated results.

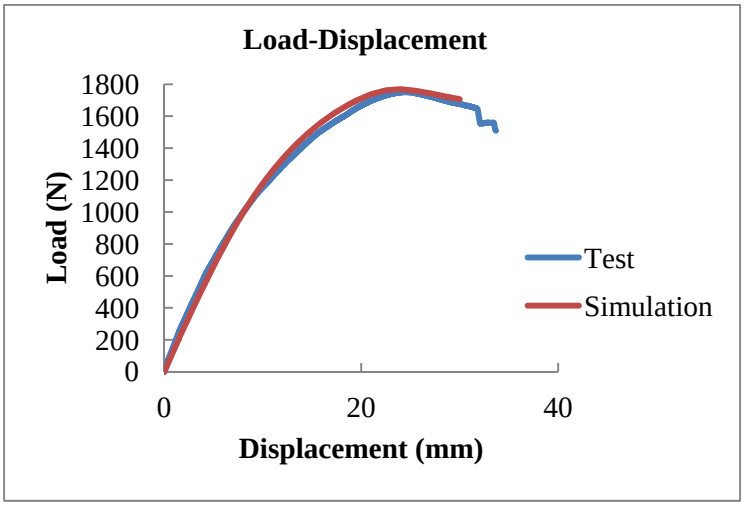

Figure 10. Load displacement curves from numerical and experimental testing of the shock tower

Finally, Figure 11 shows the comparison between simulated and physically tested results, we can see that the failure location predicted by FE analysis was validated by experimental results.

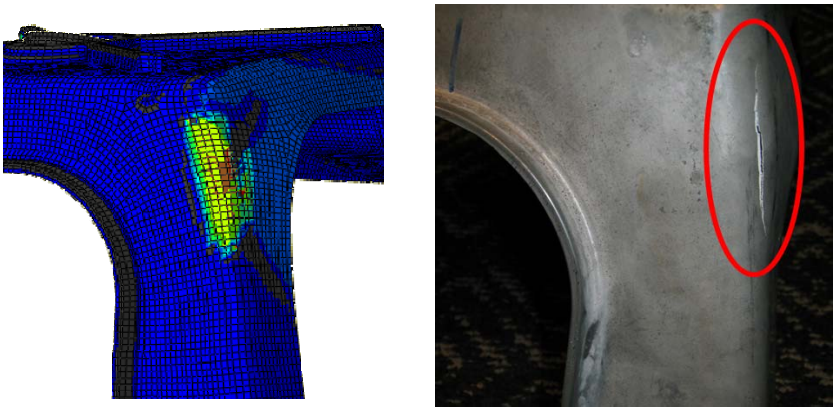

Figure 11. Failure location from FE analysis and experimental testing

As a conclusion, the microstructure-property material model was able to predict the failure location of a magnesium alloy component under monotonic loading. The simulated results correlated the experimental ones in terms of load and displacement but in terms of failure location as well providing that the initial porosity mapping and geometrical feature of the CAD were respected. For this load case, the accuracy of the thickness in the failure area and the fidelity of porosity mapping were first order parameters for a successful and accurate failure location prediction.

References

[1]: M.F. Horstemeyer, D. Oglesby, J. Fan, P.M. Gullett, H. El Kadiri, Y. Xue, C. Burton, K. Gall, B. Jelinek, M.K. Jones, S. G. Kim, E.B. Marin, D.L. McDowell, A. Oppedal, N. Yang, USCAR MSU CAVS CMD 2007-R0001: From Atoms to Autos: Designing a Mg Alloy Corvette Cradle by Employing Hierarchical Multiscale Microstructure-Property Models for Monotonic and Cyclic Loads.

[2] D.L. Atwell, M.R. Barnett, Extrusion limits of magnesium alloys, Metallurgical and Materials Transactions A. 38 (2007) 3032–3041.

[3] R. Hielscher, H. Schaeben, A novel pole figure inversion method: specification of the MTEX algorithm, Journal of Applied Crystallography. 41 (2008) 1024–1037.

[4] R.A. Lebensohn, C.N. Tomé, A self-consistent anisotropic approach for the simulation of plastic deformation and texture development of polycrystals: application to zirconium alloys, Acta Metallurgica Et Materialia. 41 (1993) 2611-2624.

SUBTASK 1.2: CYBERINFRASTRUCTURE

Team Members: Tomasz Haupt, Raghu Chinni (student), Nitin Sukhija (student)

SUMMARY OF THE PROGRESS

1. No substantial funding has been assigned to develop new features for the Cyberinfrastructure in Phase IV. Our activities have been reduced to the maintenance of the system that has been developed in Phases I through III, that is, the Engineering Organization for Cyber Design (EVOCD). The leave of our previous EVOCD administrator (Igor Zhuk) forced us to introduce many changes and improvements of the EVOCD deployment procedures, in order to get more support from MSU HPCC system administrator, as in this phase of the project, the position of EVOCD administrator is left vacant. In addition we continue providing support for adding new content to the EVOCD Wiki (N. Sukhija). In addition, we are finalizing the improved Web interface to the Image Analyzer model calibration tool together with its documentation (R. Chinni).
2. The EVOCD Wiki has been visited 6092 times (Jan. 1 – March 31, 2012), recently reaching over 600 visits per week. Still the most popular pages are those describing the use of LAMMPS.
3. We also continue to maintain the ICME collaborative portal for the participants of the Magnesium Front End Research and Development (MFERD) tree-nation pilot program.
4. We (Haupt, Sukhija) continue research towards providing cyberinfrastructure support for reliable performing multistage simulations. The research is twofold:
    a. We continue the research on autonomic computing towards developing the support for executing complex workflows as required by multiscale simulations. The research resulted in two scholarly, peer-reviewed publications:
        i. T. Haupt, N. Sukhija, I. Zhuk, “Autonomic Execution of Computational Workflows”, GSTF International Journal on Computing, Vol. 1, No. 4, pp-10-17 (2012)
        ii. T. Haupt, “Towards Mediation-Based Self-Healing of Data-Driven Business Processes”, accepted to SEMS’12 (7th International Symposium on Software Engineering for Adaptive and Self-Managing Systems), Zurich, Switzerland
    b. We started an effort to integrate Multiphysics Object Oriented Simulation Environment (MOOSE), developed at DOE Idaho National Laboratory, into our Cyberinfrastructure. To this end:
        i. We have obtained the MOOSE license that would allow us to install it at CAVS.
        ii. T. Haupt attended the three-day MOOSE workshop organized by the MOOSE developers in Boston, MA (January 10-12, 2012)

ACTIONS PLANNED FOR THE NEXT QUARTER

In the next quarter, in addition to the continuation of efforts described above, we will aggressively populate the repository of data to capture most of the experimental data generated at CAVS in order to use these data for the independently funded research on material informatics. As a byproduct, we

expect this activity significantly improve the quality of contents of the EVOCD data repository (the unexpected maintenance effort described in point 1 above prohibited us to perform this task in this quarter, as planned).

SUBTASK 1.3: FATIGUE PERFORMANCE OF LIGHTWEIGHT MATERIALS

***Team Members: Mark. F. Horstemeyer**, M. Lugo, J.B. Jordon, M.F. Horstemeyer, J. Bernard (PhD student), and D. Rayborn (undergraduate)*

SUMMARY OF THE PROGRESS

The experiments on the selected magnesium alloys (AZ31, AZ61, and AM30) will be performed with the intent to determine fatigue behavior of magnesium alloys and components. In addition, structure-property analysis will be conducted to determine relations between microstructural features and fatigue life. In-situ scanning electron microscope (SEM) experiments will be conducted to determine fatigue crack incubation and microstructurally/physically small fatigue crack stages. Experiments will also be performed to determine the fatigue performance of several different types of joints.

Based on the experiments performed in this task, a multi-stage model will be developed. The approach will be based on the experimental results and observations and multi-scale numerical work. The results of lower length scale simulations of fatigue of magnesium alloys will be integrated into the fatigue model developed here. The fatigue model to be developed in this task is adapted from an existing fatigue model for various cast and wrought aluminum alloys [1-4]. The existing MultiStage fatigue (MSF) model uses a microstructure-based approach that is developed from the observations of the three stages of fatigue damage evolution at various scales [1]: incubation, microstructurally small/physically small crack growth, and long crack growth. The fatigue damage driving mechanisms for each stage varies with the interaction of microscale-loading and microstructural features. As such, the total fatigue life can be decomposed as

$$N_{\text{Total}} = N_{\text{Inc}} + N_{\text{MSC/PSC}} + N_{\text{LC}}$$

where, N_{Total} is the total fatigue life. N_{Inc} is the number of cycles to incubate a crack at a micronotch formed by an inclusion, which can be a relatively large constituent particle, a large pore, or a cluster of each or both. The incubated crack extends from the inclusion into the matrix and propagates through a region of the micronotch root influence. $N_{\text{MSC/PSC}}$ is the number of cycles required for propagation of a microstructurally small/ physically small crack. Finally, N_{LC} is number of cycles required for long crack (LC) propagation to final failure, which depends on the amplitude of loading and the corresponding extent of microplasticity ahead of the crack tip. This multistage framework will be evaluated for the prediction of fatigue damage in magnesium alloys and magnesium welded joints. The MSF will also be implemented into commercial FEA codes and validated by solving specific problems concerning the mechanical response and reliability/safety aspects of magnesium alloys used in automotive applications.

References

[1] D.L. McDowell, Ken Gall, M.F. Horstemeyer, and J. Fan. Microstructure-Based Fatigue Modeling of Cast A356-T6 Alloy. Engineering Fracture Mechanics, Vol. 70, pp. 49-80, 2003.

[2] Y. Xue, D.L. McDowell, M.F. Horstemeyer, M.H. Dale, and J.B. Jordon.Microstructure-based Multisatge Fatigue Modeling of Aluminum Alloy 7075-T651, Vol. 74, pp. 2810-2823, 2007.

[3] J.B. Jordon, J.B. Gibson, M.F. Horstemeyer, H. El Kadiri, J.C. Baird, A.A. Luo, 2011, Effect of twinning, slip, and inclusions on the fatigue anisotropy of extrusion-textured AZ61 magnesium alloy, Material Science and Engineering A, 528, p 6860-6871.K.

[4] J.B. Jordon, M.F. Horstemeyer, N. Yang, J.F. Major, K.A. Gall, J. Fan, 2010, Microstructural Inclusion Influence on Fatigue of a Cast A356 Aluminum Alloy, Metall Mater Trans A. 41A, p 356-363.

Fatigue Damage and Microstructure Properties in an AM30 Extruded Magnesium Alloy

Introduction

A strain controlled fatigue test program was conducted to quantify and to evaluate the mechanisms of fatigue and the fatigue life in an extruded AM30 magnesium alloy. A multistage fatigue (MSF) model was developed to predict the fatigue behavior. The MSF model comprises three scales of cyclic damage; crack incubation, microstructurally small crack (MSC) and physically small crack (PSC), and long crack growth. The multistage fatigue model (MSF) will predict when a crack develops in a component.

Materials and Experiments

The material employed in this research was an extruded AM30 magnesium alloy. The material was provided in the form of an automotive crash rail profile with a thickness of approximately 2.5 mm. Samples for this study were taken in the extrusion direction (ED) and in the transverse direction (ETD) as shown in Figure 1. Fatigue specimens were designed in conformity with ASTM standard E-647 with a gage length of 15 mm. Fatigue tests were conducted on a servo-controlled electro-hydraulic system. These tests were performed under strain control mode, constant strain amplitude, and fully reversed. Tests were conducted at room temperature and a sinusoidal cyclic loading was applied with a frequency of 5 Hz. A 50% drop of the peak stress load was used to determine failure of the sample. The amplitude levels tested ranged from 0.2 to 0.6 % of strain.

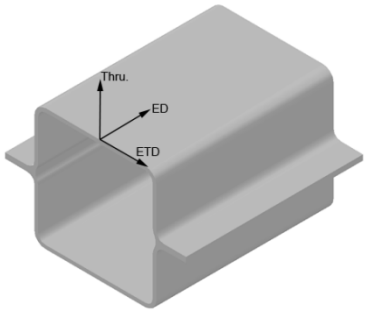

Figure 1. Profile of the material under study, and location and orientation of samples.

Experimental Results

Monotonic behavior of AM30

Figure 2 shows the stress-strain curves for tension along both the ED and the ETD directions. These curves show the anisotropic and asymmetric mechanical behavior. The yield strengths, hardening rates, and ultimate strengths are different in each orientation as well as in compression. The yield strength in

tension was found to be about (180 MPa) while that the strength along the transverse direction was found to be about (60 MPa). The yield stress under the ETD was approximately 1/3 of that under the ED.

The monotonic properties reported by Begum et al. 2008 [1] differ from that results shown here for the same alloy. These differences could be attributed to differences in texture, and grain size variations due to the extrusion process. By the other hand, the differences observed in the stress-strain behavior between extrusion and transverse directions can be attributed to the different deformation modes activated in each direction. In tension along the extrusion direction slip deformation is formed through the prismatic and basal planes, consequently slip is the predominant mechanism. While that along the transverse direction the predominant mechanism is twining.

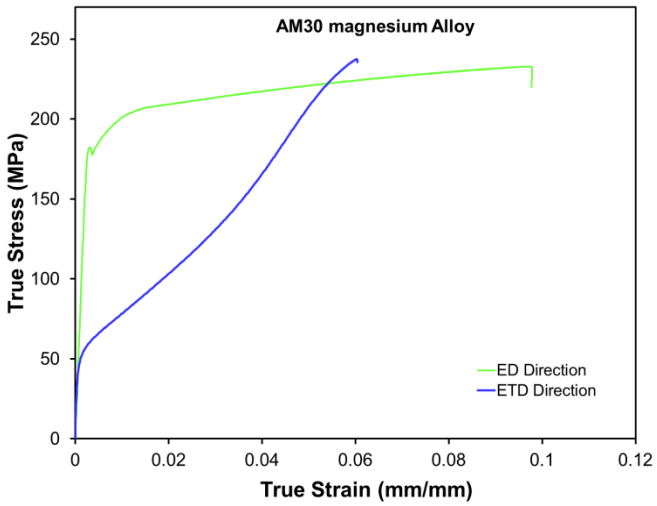

Figure 2. Stress-strain monotonic behavior of an AM30 magnesium alloy in the extrusion direction, in the transverse direction, and compression in the extrusion direction.

Strain-Life

Figure 3 shows the strain-life for extruded AM30 magnesium alloy in the extrusion and transverse directions, for strain controlled, constant strain amplitude and completely reversed loading conditions. Fatigue tests for higher strain amplitudes in the transverse directions were unsuccessful due to the significant plasticity undergone by the specimens. The strain-life curve in the log-log domain shows a pattern from 0.6 to close to 0.3 %, then the slope changes drastically below of a strain amplitude of 0.3%.

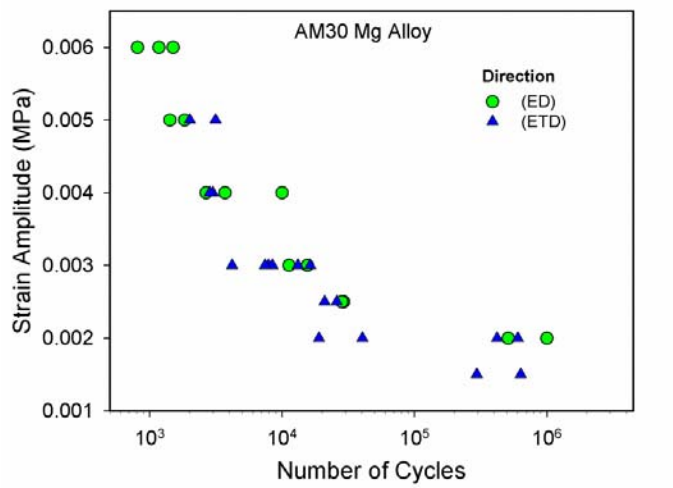

Figure 3. Total strain life of an AZ31 magnesium alloy

Cyclic Deformation Response

Figure 4 shows the stress-strain hysteresis loops for the ED at strain amplitudes of 0.6, 0.4, 0.3, and 0.2 percent. An asymmetric pattern in the cyclic deformation is observed for the first cycle for all the strain amplitudes. This asymmetry is more pronounced at higher strain levels. This asymmetry is more pronounced for the first cycle, and at higher strain levels. The hysteresis loops show that hardening take place at lower strain amplitudes under tensile loading, and hardening under compressive loading. For lower strain amplitudes the tensile and compressive stress was almost the same. The asymmetry from tensile to compressive is larger as the strain amplitude increases. For lower strain amplitudes the tensile and compressive stress was almost the same. The asymmetry from tensile to compressive is larger as the strain amplitude increases. The cyclic stress-strain asymmetry observed in AM30 magnesium alloy is due to twinning activation during unloading in compression, and detwinning during loading in tension [2-4]. A typical plateau is observed in the stress-strain response during compression loading and is observed in other magnesium alloys reported elsewhere [2-4]. The mid-life hysteresis loops remained relatively asymmetric at higher strain amplitudes while nearly symmetric patterns are seen at lower strain amplitudes.

Cyclic stress-strain hysteresis curves for the ETD at strain amplitude of 0.5, 0.4, 0.3, and 0.2 percent are shown in Figure 5. The first cycle show a highly asymmetric behavior for all strain amplitudes. A tenuous plateau is observed during compression loading for the first cycle markedly at high strain amplitudes, which is a clear indication of twining. These curves show a slight asymmetry for all strain amplitudes. In addition it is observed that the hysteresis loop began with twinning in tension, and pseudo-elasticity during unloading, while reloading in compression marked an inflection point, which is an indication of detwinning.

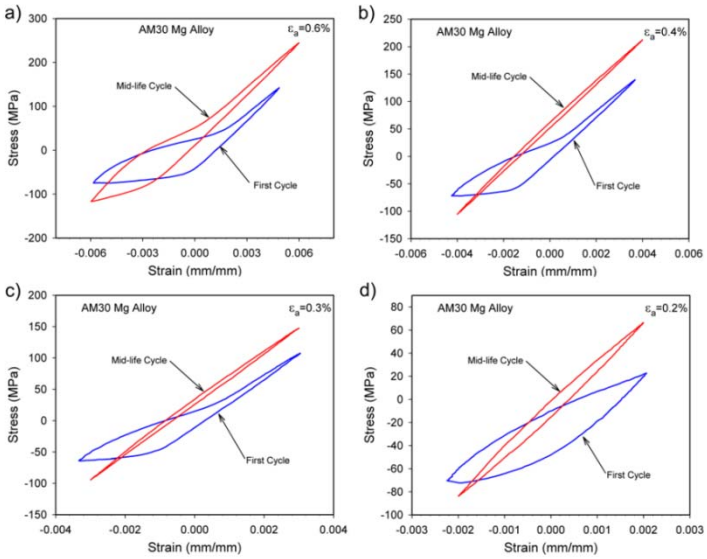

Figure 4. Hysteresis curves of AM30 extruded Mg alloy in the extruded direction at the strain amplitudes of a) 0.6%, b) 0.5%, c) 0.3% and d) 0.2%

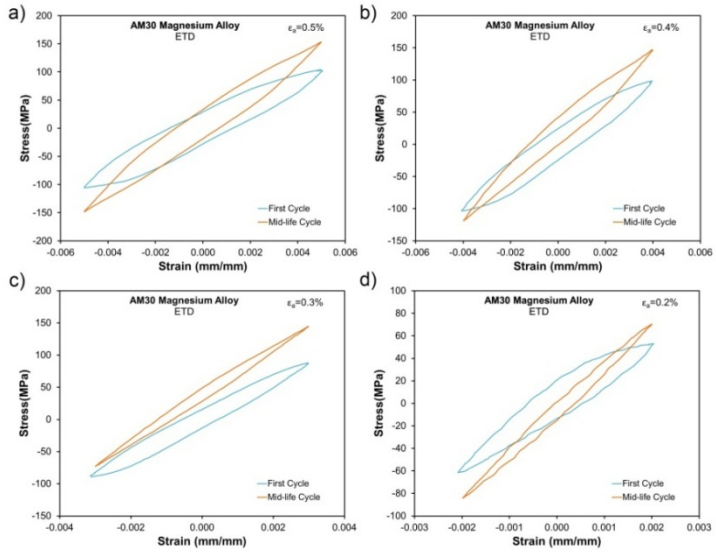

Figure 5. Hysteresis curves of AM30 extruded Mg alloy in the transverse direction at the strain amplitudes of a) 0.5%, b) 0.4%, c) 0.3% and d) 0.2%

Figures 6 and 7 show the evolution of stress amplitude as a function of number of cycles for the ED at the strain amplitudes from 0.2% to 0.6%. It is observed an increase in the stress amplitude as the number of cycles increased. The strain amplitudes ranging from 0.3% to 0.6% showed a greater hardening effect than the others strain amplitude levels.

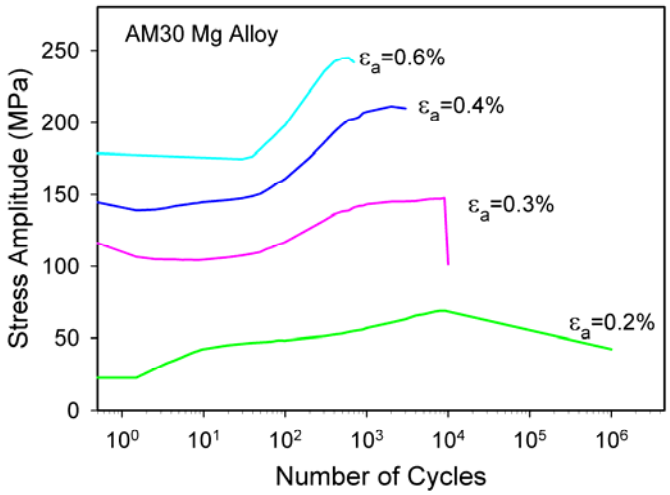

Figure 6. Stress amplitude response of AM30 magnesium alloy

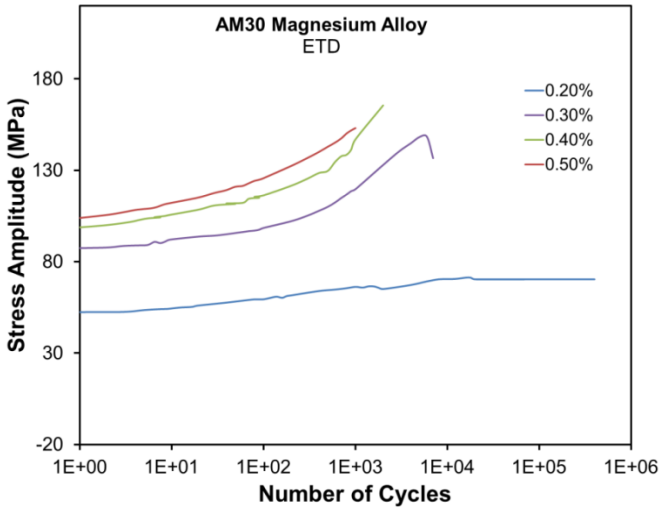

Figure 7. Stress amplitude response of AM30 magnesium alloy

Fatigue Fractured Surfaces

Fractured surfaces of the magnesium AM30 magnesium alloy that were observed showed typical indications of fatigue damage. River marks flowing outward from a single location at the surface were observed on all specimens. Figures 8 and 9 show typical fracture surfaces of both ED and ETD directions, in which are observed that a particle initiated the crack. In addition, the SEM images revealed evidence of twinning on the fatigue fracture surfaces similar to that has been reported in the literature [5-6].

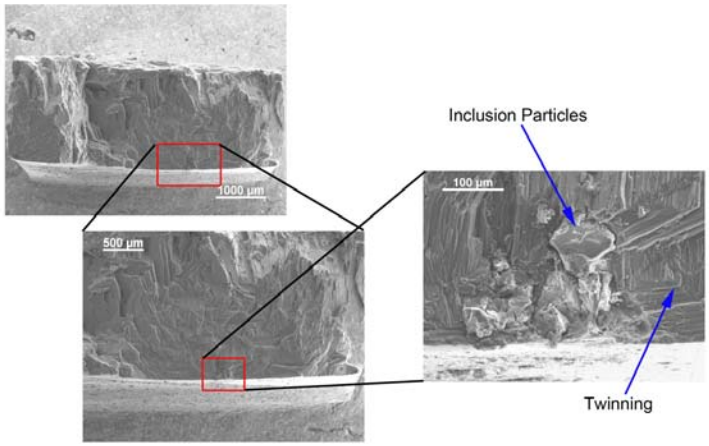

Figure 8. Typical fractured surface for an AM30 magnesium Alloy in the ED direction. The crack developed at a small inclusion. In addition, twinning is observed near the crack site.

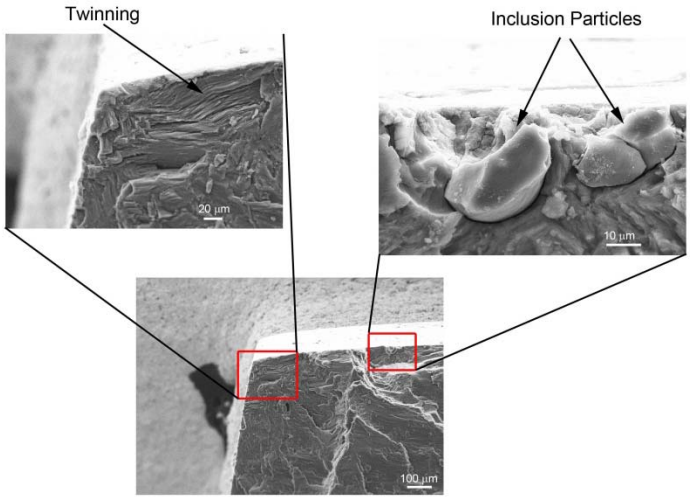

Figure 9. Typical fractured surface for an AM30 magnesium Alloy in the ETD direction. The crack developed at a small inclusion. Twinning is also observed on the fracture surface.

Multistage Fatigue Modeling

Figure 10 shows the correlations of the MSF model to experimental data for both ED and ETD. Table 1 lists the model constants used to correlate the model to fully-reversed uniaxial strain life results for the extruded AM30 magnesium alloy in the extrusion and transverse direction. It is important to note that the basic material constants were identical regardless of the orientation of cyclic loading, but the microstructural features and mechanical properties were the only items that were different.

As shown in Figure 10, MSF model appears to correlate to the general trend of the fatigue life in both direction (ED and ETD). In the model the effect of twinning is captured through the cyclic stress-strain response.

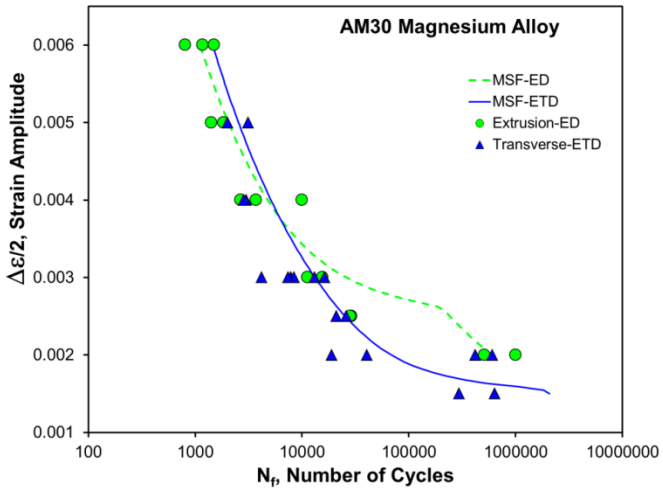

Figure 10. Multistage fatigue (MSF) model and strain-life results for AM30 magnesium alloys

Table 1. MSF Parameters for extruded AM30 magnesium alloy.

	Constant	ED	ETD	Description
Crack Incubation	C_n	*0.95*	*0.95*	Constant related to Cm constant (CNC)
	C_{inc}	*0.55*	*0.55*	Ductility coefficient in Modified Coffin Manson Law
	α	-0.64	-0.64	Ductility exponent in Modified Coffin Manson Law
	q	*2.23*	*2.23*	Exponent in remote strain to local plastic shear strain
	y_1	*120*	*120*	Constant in remote strain to local plastic shear strain
	y_2	*0*	*0*	Linear constant in remote strain to local plastic shear strain
	ξ	4.5	4.5	Geometric factor in micromechanics study
	r	*0.2*	*0.2*	Exponent in micromechanics study
Small Crack (MSC/PSC)	*ω*	0.15	0.15	Omega
	ai	0.625	0.625	Initial crack size contribution
	θ	0.135	0.135	Load path dependent and loading combination parameter
	ζ	1.2	1.2	Exponent in Small crack growth
	C_I	300000	300000	HCF constant in small crack growth
	C_{II}	0.0001	0.0001	LCF constant in small crack growth
	χ	0.32	0.32	Crack growth rate constant
	CTDH	0.00032	0.00032	CTD threshold value

Conclusions

The cyclic behavior of extruded magnesium AM30 alloy were investigated based on the microstructural properties. A multistage fatigue (MSF) model was used to capture the strain-life behavior. In regards of the research conducted here the following conclusions can be made:

- Monotonic tensile tests revealed a difference in yield strength between the extrusion direction and transverse direction. The transverse orientation showed lower yield strength.
- Hysteresis loops showed an asymmetric pattern for all the observed strain amplitudes. The asymmetry was more emphatic for the first cycle of the cyclic process.

- Compression twinning and detwinning were observed in the hysteresis loops for the extrusion direction. Conversely, the hysteresis loops for the extrusion transverse direction showed tensile twinning and detwinning.
- For the ED the asymmetric cyclic behavior remained for all the cyclic life as was revealed by the mid-life cycles. This asymmetry was less pronounced for the 0.2% strain amplitude.
- Strain hardening was observed for all the strain amplitudes but more significant for the higher strain levels.
- Fatigue cracks incubated from fractured particles near the free surface of the specimens for both directions. Fracture surfaces showed twinning for most of the specimens studied.
- For high cycle fatigue region a small difference is noted in the fatigue between the extrusion and extrusion transverse directions.
- The multistage fatigue model incorporated the differences in grain orientation, grain size, particle size, and cyclic hardening parameters in order to capture the differences in fatigue behavior in the extrusion direction and the extrusion transverse direction. We note that the other material constants were not changed for the incubation and MSC regimes.

References

[1] J.B. Jordon, M.F. Horstemeyer, N. Yang, J.F. Major, K.A. Gall, J. Fan, 2010, Microstructural Inclusion Influence on Fatigue of a Cast A356 Aluminum Alloy, Metall Mater Trans A. 41A, p 356-363.

[2] J.B. Jordon, J.B. Gibson, M.F. Horstemeyer, H. El Kadiri, J.C. Baird, A.A. Luo, 2011, Effect of twinning, slip, and inclusions on the fatigue anisotropy of extrusion-textured AZ61 magnesium alloy, Material Science and Engineering A, 528, p 6860-6871.K.

[3] S. Begum, D.L Chen, S. Xu, and Alan Luo, "Strain-Controlled Low-Cycle Fatigue Properties of a Newly Developed Magnesium Alloy", *Metallurgical and Materials Transactions A*, 39A, 3014, 2008.

[4] D.W. Brown, A. Jain, S.R. Agnew, and B. Clausen, "Twinning and Detwinning During Cyclic Deformation", *Materials Science Forum*, Vol. 539-543, pp. 3407-3414, 2007.

[5] F. Yang, S.M. Yin, S.X. Li, and Z.F. Zhang, "Crack Initiation Mechanism of Extruded AZ31 Magnesium Alloy in the Very High Cycle Fatigue Regime", *Materials Science and Engineering A*, 491, pp. 131-136, 2008.

[6] S. Morita, S. Tanaka, N. Ohno, Y. Kawakami, and T. Enjoji, "Cyclic Deformation and Fatigue Crack Behavior of Extruded AZ31B Magnesium Alloy", *Materials Science Forum*, Vols 638-642, pp. 3056-3061, 2010.

Modeling of Small Fatigue Crack Behavior of an Extruded AZ61 Magnesium Alloy

Introduction

Several techniques have been used in order to make observations of small fatigue cracks, such as *in-situ* tests with scanning electron microscope (SEM) observations [1-3]. Observations by replication using ac paper [4] and other means [5-6] have also been employed in order to characterize fatigue crack growth on a small scale. Recently, Jordon *et al.* [7] introduced a new technique for the replicating method, which was also utilized in this study with the ambition of measuring the small crack fatigue regime for the wrought AZ61 magnesium alloy. The object of this research is to make small fatigue crack growth observations of an extruded AZ61 magnesium alloy with the purpose of quantifying this fatigue regime for the given material.

Materials and Experimental Methods

The material used in this study was an AZ61 magnesium alloy extruded into an automotive crash rail, as shown in Figure 1. Note in Figure 1b the layout of the transverse specimens.

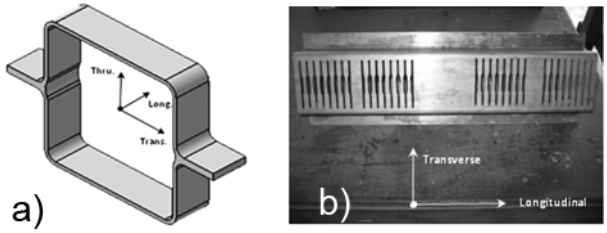

Figure 1. a) Cross-sectional geometry of the as received, extruded AZ61 magnesium alloy crash rail and b) Transverse specimen layout.

In order to conduct fatigue tests upon the material, flat dog-bone specimens were machined from the rail in the transverse (as shown in Figure 1b) and longitudinal orientations. Since a location favorable for crack growth was required for consistent scrutiny, a notch with a radius of 35 mm was machined into the face of the gage to a depth of 300 µm. The specimen layout is illustrated in Figure 2. This was similar to methods found in literature [4, 8]. In order to reduce surface contaminants and premature failure due to specimen machining, the surfaces of the shoulder, gage, and notch of each specimen were hand ground along the loading direction using 800grit sandpaper.

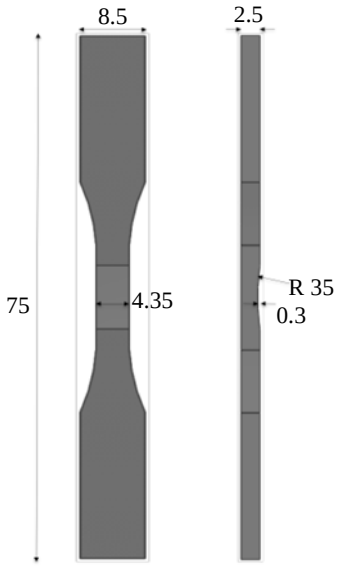

Figure 2. Fatigue specimen geometry with the crack-initiating notch. All dimensions are in millimeters.

In addition to sanding with 800grit sand paper, a number of specimens were also polished with a series of 1200grit, 9µm, 6µm, 1µm, and 0.25µm diamond pastes before finally being polished with OPS. OPS is a silicon dioxide (SiO_2) suspension that served a dual purpose. In addition to polishing the specimen surfaces, it also mildly etched them as observed by Gall *et al.* [1-2]. Ethanol was used to

degrease all surfaces after polishing. Fully reversed, load-controlled tests were then conducted to failure on these notched specimens. Several specimens that were fatigue tested were interrupted at set intervals in order to take replicas of the notch. The specimen was held at zero load while replicating. These replicas were made by using a dual-part silicone based compound, called Repliset®. Upon specimen failure, the fracture surfaces were cut off from the specimen and mounted for SEM or optical examination for further fractography analysis.

Small Fatigue Crack Behavior

Using SEM and three-dimensional profiling microscope imaging and optical imaging of the replicas, the locations of fatigue crack initiation and subsequent growth on the notch surfaces were identified. After identifying the crack initiation site illustrated in Figure 3, crack lengths were measured starting with the last replica prior to failure then progressing backwards until the crack was no longer visible.

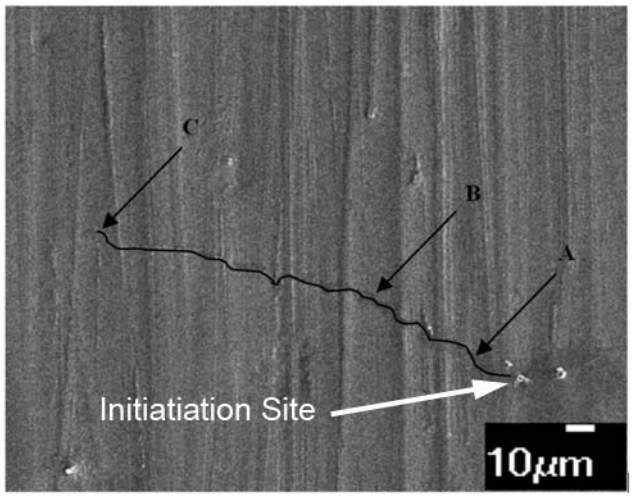

Figure 3. Replica image illustrating the path of the dominant failure-inducing crack.

Crack growth rate was calculated utilizing a point-by-point calculation previously utilized by Jordon *et al.* [7] and is illustrated in Equation 1, where a is the crack length and N is the number of cycles.

$$\frac{da}{dN} = \frac{a_{i+1} - a_i}{N_{i+1} - N_i} \qquad (1)$$

Analysis of Repliset replicas for both longitudinal and transverse orientations has rendered the following results in terms of crack growth rate versus crack length. Subsequent examination of transverse-oriented specimen fracture surfaces has also produced crack growth rates based upon striation measurements. These results are shown below in Figure 4.

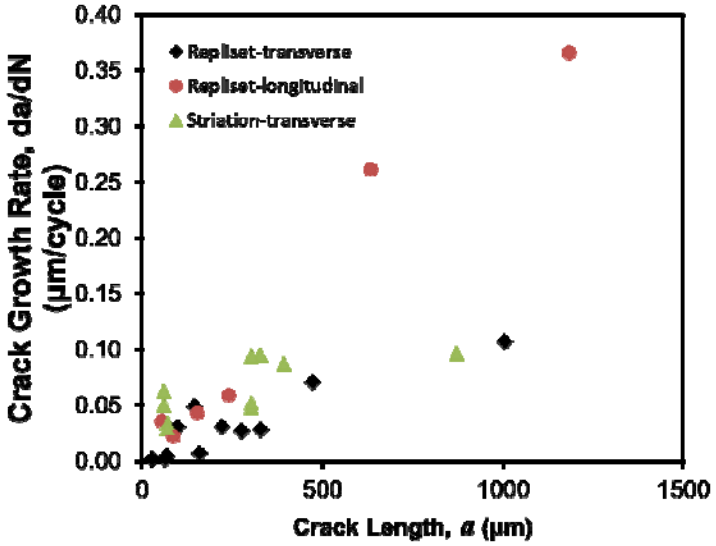

Figure 4. Crack growth rates compared to crack lengths for longitudinal and transverse specimens. Striation measurements showing fracture surface crack growth rates are also shown.

Preliminary fitting of the crack growth data for the transverse orientation has been conducted using the multi-stage fatigue (MSF) model. By adjusting the effects of grain orientation upon crack growth, upper and lower bounds were produced and were able to capture the range of marked acceleration/deceleration of the crack as it propagated throughout the material. Figure 5 shows the bounding of the transverse data with the model-predicted limits.

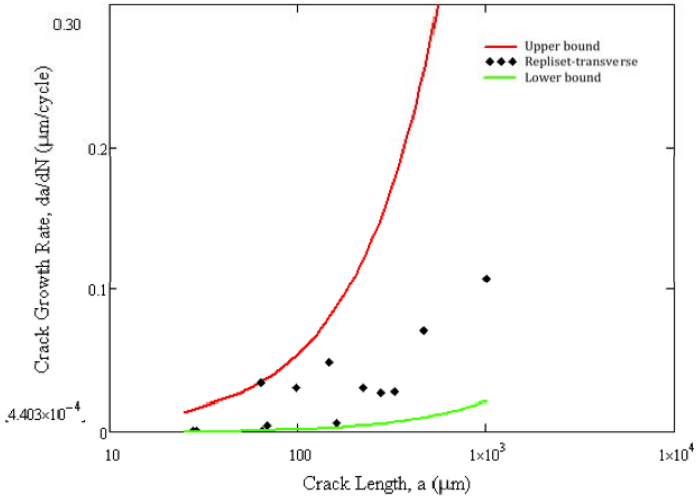

Figure 5. Crack growth rate of the transverse orientation illustrating the upper and lower bounds as calculated from the multi-stage fatigue (MSF) model.

Conclusions

Based on the small fatigue crack experiments and modeling presented here, the following summary is given:

1. Surface preparation and replicas taken of the notch were observed to have no notable impact on the fatigue life of the alloy.

2. The crack growth rates for the microstructurally small crack regime could be quantified by using the replica process shown here.

3. The crack growth rate equation from the MSF model was applied to the MSC regime of the experimental data with a high degree of accuracy simply by manipulating the grain orientation constant, which was tabulated here.

References

[1]. K. Gall, G. Biallas, Hans J. Maier, P. Gullett, M. F. Horstemeyer, D. L. McDowell, and J. Fan, "*In-Situ* Observations of High Cycle Fatigue Mechanisms in Cast AM60B Magnesium in Vacuum and Water Vapor Environments," *International Journal of Fatigue*, 26 (2004) 59-70.

[2]. K. Gall, G. Biallas, H. J. Maier, P. Gullett, M. F. Horstemeyer, and D. L. McDowell, "*In-Situ* Observations of Low-Cycle Fatigue Damage in Cast AM60B Magnesium in an Environmental Scanning Electron Microscope," *Metallurgical and Materials Transactions* A, 35 (2004) 321-331.

[3]. K. Gall, G. Biallas, H. J. Maier, M. F. Horstemeyer, and D. L. McDowell, "Environmentally Influenced Microstructurally Small Fatigue Crack Growth in Cast Magnesium," *Materials Science and Engineering A*, 396(2005) 143-154.

[4]. J.F. Lei, Q.J. Wang, Y.Y. Liu, S.X. Guan, Z.G. Wang, D. Li, and Z.Q. Hu, "Fatigue Crack Initiation at Nd-Rich Particles in an Nd Containing High Temperature Titanium Alloy,"*Journal of Materials Research*, 12 (10) (1997)2571-2574.

[5]. A.N. Chamos, C.A. Charitidis, A. Skarmoutsou, and SP.G. Pantelakis, "An Investigation on the High Stress Sensitivity of Fatigue Life of Rolled AZ31 Magnesium Alloy Under Constant Amplitude Fatigue Loading,"*Fatigue and Fracture of Engineering Materials and Structures*, 33 (2009) 252-265

[6]. A.N. Chamos, SP.G. Pantelakis, V. Spiliadis, "Fatigue Behavior of Bare and Pre-Corroded Magnesium Alloy AZ31,"*Materials and Design*, 31 (2010) 4130-4137.

[7]. J.B. Jordon, J.D. Bernard, J.C. Newman Jr.,"Quantifying Microstructurally Small Fatigue Crack Growth in an Aluminum Alloy Using a Silicon-Rubber Replica Method,"*International Journal of Fatigue*, 36 (1) (2012) 206-210.

[8]. K. Tokaji, M. Kamakura, Y. Ishiizumi, N. Hasegawa, "Fatigue Behavior and Fracture Mechanism of a Rolled AZ31 Magnesium Alloy," *International Journal of* Fatigue, 26 (11) (2004) 1217-1224.

ACCOMPLISHMENTS

1. We have an updated multistage fatigue (MSF) Model for an AM30 magnesium alloy in both extrusion and transverse direction.
2. We have conducted small crack fatigue tests on AZ61 in both longitudinal and transverse direction using the Repliset method to determine crack incubation lifetimes.
3. Micrographs of AZ61 have been performed using optical and SEM techniques to determine crack length and crack growth rates for the microstructurally small crack fatigue stage.
4. Continue development of fatigue model for friction stir welds.

Actions Planned for the Next Quarter

1. We will continue the small crack fatigue testing on AM30.
2. We will continue the small crack fatigue testing on AZ61.
3. Continue development of fatigue model for friction stir welds.

SUBTASK 1.4: MULTISCALE MODELING OF CORROSION

***Team Members: Holly Martin**, C. Walton (GRA), W. Song (GRA)*

SUMMARY OF THE PROGRESS

Last quarter dealt with the development of a continuum damage model that can begin to accurately predict competing corrosion rates of general corrosion (weight and thickness), pitting corrosion (pit number density, in-plane pit area, pit volume, nearest neighbor distance), and intergranular corrosion (intergranular corrosion area fraction). The following conceptual model wass presented in order to theoretically place the different mechanisms in a framework for future mathematical modeling following the work of Horstemeyer et al. as follows:

$$\phi = \phi_{GC} + \phi_{PC} + \phi_{IC} \tag{1}$$

where ϕ is the total damage, which is the area fraction or volume fraction of material lost, from all forms of corrosion; ϕ_{GC} is the area or volume fraction lost due to general corrosion; ϕ_{PC} is the area or volume fraction lost due to pitting corrosion; and ϕ_{IC} is the area or volume fraction lost due to intergranular corrosion.

The associated rate equations and the expanded rate equations for pitting corrosion were provided, as shown here in Equations 2-3.

$$\dot{\phi} = \dot{\phi}_{GC} + \dot{\phi}_{PC} + \dot{\phi}_{IC} \tag{2}$$

where $\dot{\phi}_{GC}$ is the time rate of change of the volume fraction (or thickness change) related to general corrosion and is chemically a function of a reaction between water and magnesium (no chlorine is involved) so it affects both the grain and eutectic regions; $\dot{\phi}_{PC}$ is the time rate of change of the volume fraction related to pitting corrosion where chlorine is required for nucleation, growth, and coalescence and it affects the grain interior moreso than the eutectic region; and $\dot{\phi}_{IC}$ is the time rate of change of the volume fraction related to intergranular corrosion and is solely a function of water and a reaction between two dissimilar metals (a microgalvanic cell) and thus affects the eutectic region moreso than the grain interior.

$$\dot{\phi}_{PC} = \dot{\phi}_{\eta_p} + \dot{\phi}_{v_p} + \dot{\phi}_{c_p} \tag{3}$$

where $\dot{\phi}_{\eta_p}$ is the time rate of change of the volume fraction related to nucleation of pits; $\dot{\phi}_{v_p}$ is the time rate of change of the averaged volume fraction related to the growth of pits; $\dot{\phi}_{c_p}$ is the time rate of change of the averaged volume fraction related to the coalescence of pits.

While last quarter focused on pit growth, this quarter focused on developing the rate equation for pit coalescence, as shown in Equation 4. The pit coalescence rate, $\dot{\phi}_{c_p}$, is given as follows:

$$\dot{\phi}_{v_p} = \eta v \dot{c} \tag{4}$$

where $\dot{c}$ is the time rate of change of the volume fraction related to nucleation of pits and is given as follows:

$$\dot{c} = k_e \left(\frac{\dot{q}_1 q_2}{r^2} + \frac{q_1 \dot{q}_2}{r^2} + \frac{q_1 q_2}{\dot{r}^2} \right) \tag{5}$$

where k_e is the proportionality constant, a value determined from the corrosion data collected for each magnesium alloy, $\dot{q}_1$ is the idealized point charge caused by chloride ions, $\dot{q}_2$ is the idealized point charge caused by magnesium ions, and $\dot{r}$ is the distance separating the neighboring pits, i.e. the nearest neighbor distance. The data obtained from the various magnesium alloys will be used in these formulations as a starting point to develop a continuum damage model detailing corrosion.

References

M.F. Horstemeyer, J. Lathrop, A.M. Gokhale, M. Dighe, Modeling stress state dependent damage evolution in a cast Al–Si–Mg aluminum alloy, Theor. Appl. Fract. Mech. 33 (2000) 31–47.

Horstemeyer, M.F., Gall, K.A., Dolan, K., Haskins, J., Gokhale, A.M., and Dighe, M.D., "Numerical, Experimental, and Image Analyses of Damage Progression in Cast A356 Aluminum Notch Tensile Bars," *Theoretical and Applied Fracture Mechanics*. v 39, n 1, p 23-45, 2003.

ACCOMPLISHMENTS

1. Submitted a journal article on AM30 corrosion findings to *Corrosion Science*
2. Continued writing a journal article on AZ91 corrosion findings – will be completed before Q2

PUBLICATIONS

1. W. Song, H.J. Martin, A. Hicks, M.F. Horstemeyer, P.T. Wang. "Quantification of Corrosion Pitting Under Immersion and Salt-Spray Environments on an Extruded AM30 Magnesium Alloy." *Corrosion Science*, In Review.
2. H.J. Martin, C. Walton, J. Danzy, M.F. Horstemeyer, P.T. Wang. "Quantification of Corrosion Mechanisms Under Immersion and Salt-Spray Environments on an As-Cast AZ91 Magnesium Alloy." In Preparation.
3. H.J. Martin, R.B. Alvarez, J. Danzy, M.F. Horstemeyer, P.T. Wang. "Structure-Property Quantification of Corrosion Pitting Under Immersion and Salt-Spray Environments on an As-Cast AM60 Magnesium Alloy." Invited *NACE-Corrosion* Special Edition, In Press.
4. C. Walton, H.J. Martin, M.F. Horstemeyer, P.T. Wang. "Quantification of Corrosion Mechanisms Under Immersion and Salt-Spray Environments on an Extruded AZ31 Magnesium Alloy." *Corrosion Science,* 56 (2012) 194-208.
5. H.J. Martin, M.F. Horstemeyer, P.T. Wang. "Structure-Property Quantification of Corrosion Pitting Under Immersion and Salt-Spray Environments on an Extruded AZ61 Magnesium Alloy." *Corrosion Science*. 53 (2011) 1348-1361.
6. H.J. Martin, M.F. Horstemeyer, P.T. Wang. "Comparison of Corrosion Pitting Under Immersion and Salt-Spray Environments on an As-Cast AE44 Magnesium Alloy." *Corrosion Science*. 52 (2010) 3624-3638.

7. H.J. Martin, M.F. Horstemeyer, P.T. Wang. "Effects of Salt-Spray, Humidity, and Drying on an As-Cast AE44 Magnesium Alloy." *International Journal of Corrosion*. 2010 (2010) 1-10 doi: 10.1155/2010/602342.
8. R.B. Alvarez, H.J. Martin, M.F. Horstemeyer, M.Q. Chandler, N. Williams, P.T. Wang, A. Ruiz. "Structure-Property Corrosion Relationships of a Structural AE44 Magnesium Alloy." *Corrosion Science.* 52 (2010) 1635-1648.

ACTIONS PLANNED FOR THE NEXT QUARTER

1. Finish the manuscript for AZ91
2. Complete creep experimentation for extruded AZ31 using creep cradles
3. Begin fatigue experimentation for extruded AM30
4. Begin creep experimentation for a magnesium alloy (AE44, AM30, AZ91, AZ61, AM60)

SUBTASK 1.5: MATERIAL DESIGN OF LIGHTWEIGHT MG ALLOYS

***Team Members: Seong-Gon Kim**, Sungho Kim, Amitava Moitra, M. F. Horstemeyer, M. I. Baskes*

NON-PLANAR {$10\bar{1}2$} TWINNING NUCLEATION IN MG SINGLE CRYSTAL

We observed nucleation of radially growing {$10\bar{1}2$} twinning under tensile loading in magnesium rectangular wire system without artificial creation of an twinning in atomistic molecular dynamic simulation. The twinning nucleation mechanism is very different from the conventional twinning mechanism in that the twin nucleates from a point source rather than the fault plane following the partial dislocation line in FCC crystal. The wire axis is normal to basal plane of Mg crystal. The tensile deformation in c-axis nucleates {$10\bar{1}2$} twinning starting at the corner of square of cross section of the wire. The twin boundary is spherical at the beginning and becomes linear boundaries in {10-12} planes as time goes by.

Figure 1 shows the system configuration we used in the simulation. The systems of different sizes give the same result such as 11520 atoms in 9.33 nm X 5.51 nm X 5.09 nm, 92160 atoms, 336960 atoms, 1516320 atoms in 56 X 25 X 25 nm simulation box. A significant size dependence is not observed in those systems. The embed atom method magnesium potential of Sun et. al.[4] is used. No periodic boundary conditions are used in x, y, and z directions. The atoms in 1 nm of left and right ends of the simulation box are fixed after incremental strains are applied. The rest of atoms are free to move after the strain applications. The constant NVE thermodynamics are applied where N represents the total number of atoms in the system, V represents the volume of the system, and E represents the total energy of the system. The Initial temperatures are set to 100 K by assigning the Gaussian random distribution of velocities on atoms. It takes about 5 ps for the system to reach the equilibrium condition. The ramping velocities are applied to all atoms correstponding to the strain rate of 1G/s.

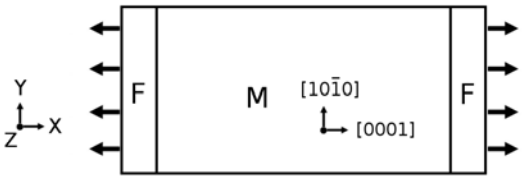

Figure 1. The schematic of the simulation configuration. Tensile strains are applied on Mg crystal in [0001] direction. No periodic boundary conditions are applied in all x, y, and z directions. The letter F indicates that atoms in the region are fixed and M indicates that atoms are mobile in the region in molecular dynamic steps after strains are applied.

Ackland method[5] is used to identify the local atomic structures and a corresponding index is assigned to each atom --- 0 for unknown, 1 for BCC, 2 for FCC, 3 for HCP, and 4 for icosahedral structure relation with neighbor atoms. The blue, cyan, green, yellow, red colors are assigned for the unknown, BCC, FCC, HCP, and icosahedral structures, respectively, in the figures.

When the strain reach about 0.0535, the defect surface of quad sphere shape nucleates from the edge in the middle and propagates away from the nucleation point. The defect surface leaves behind a HCP crystal structure which has different crystal orientation from the parents.

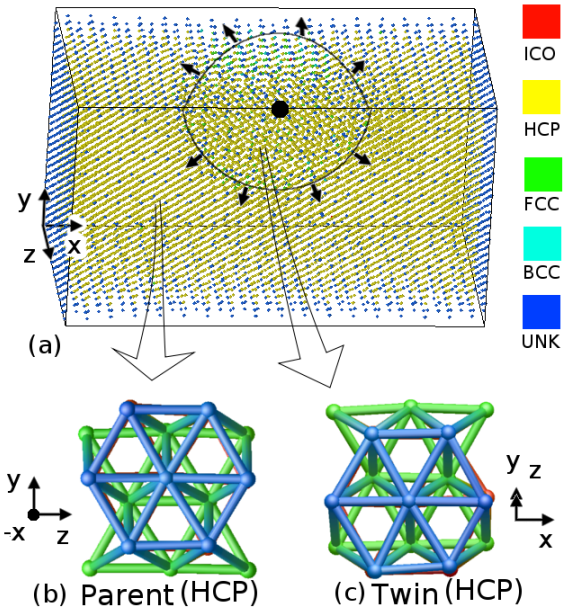

Figure 2. (Color online) (a) Twin nucleation and spherical growth of twin region from the edge in the middle indicated by a black dot. The colors of atoms represent different atomic structures classified by Ackland method[3]. The ICO represent icosahedral structure and the UNK unknown. The twin structures are HCP indicated by yellow as well as parent. (b) The structures of parent is magnified and viewed from x direction. The basal planes of parent is normal to x-axis. (c) Twin region is magnified at specific view points to show the basal planes of twin. The colors in (b) and (c) represent depth.

Fig. 2 shows three dimensional nucleation of a twin. The colors represent the different structures classified by Ackland method[5]. The twin structure has the same HCP as the parent and has a different crystal orentation. The twin boundary is distinguished by different colors. The nucleated twin grows spherically from the nucleation point of the edge in the middle of the simulation box indicated by a black dot in the figure.

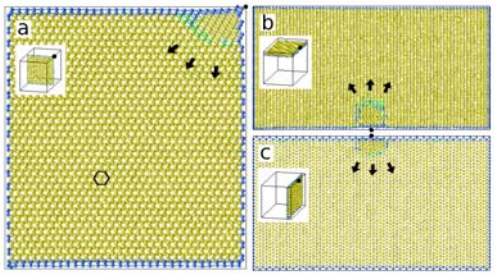

Figure 3. (Color online) Left side view (a), top view (b), front view (c) of a few layers of slab cuts containing the twin nucleation point colored by Ackland method. The inner figures show the slab cuts for each view. Black dots represent the twin nucleation point. Black arrows indicate the twin growth directions.

Fig. 3(a) shows the side view of slab cut containing the twin nucleation point. The inset figure shows how the slab is cut in the whole simulation box. The black dots indicate the twin nucleation points. The black arrows indicate the twin growth directions. The twin boundary The front, top, and side view of slab cuts containing the twin nucleation point show in Figure 3 that the twin grow spherically in early stage of twin nucleation. The twin nucleates from top right conner and propergates spherically toward bottom left conner. As the twin region grows, two prismatic planes in parent region are aligned and form one basal plane in twin region. The angle between parent basal plane and twin basal plane look like right angle. The angle between parent and twin basal planes in $\{10\bar{1}2\}$ twin are 87° according to theory. The twin boundary in the –z direction is faster in speed and wider in width than –y direction.

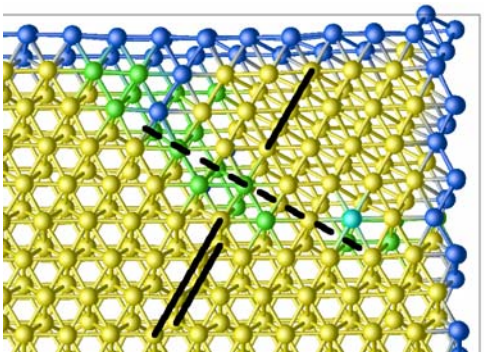

Figure 4. A shuffle motion of the parent basal planes, colored by Ackland method. Dotted line represents the plane of shear.

Fig. 4 shows the magnified left side view of twin boundary structure. The dotted black line indicates the twin boundary which is propagating from the right top conner to the bottom left corner. A pair of black solid lines in parent will be aligned with the black solid line in the top right conner of the twin region. The black solid line in the twin region is the basal plane of the twin structure. The prismatic planes in the parent hcp structure transform to the basal planes in the twin structure. The twinning boundary in the z direction is much thicker than the others.

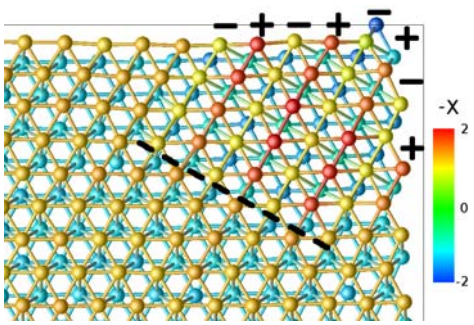

Figure 5. A shuffle motion of twin basal planes, colored by Ackland method. Dotted line represent plane of shear. Colors represent position in (-x)-direction out of paper. The + signs indicate upward movements, the - signs downward.

In Fig. 5 atoms are colored by x positions of each atom. The red color and + sign indicate that the atoms are close, and the blue color and – sign indicate that the atoms are far. The plus and minus signs indicate the corrogation of layers in the twinning region. The basal plane of the parent becomes the corrogated prismatic plane of the twin.

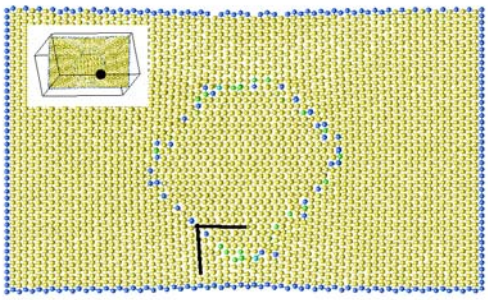

Figure 6. A few layers of $(11\bar{2}0)$ plane slicing the twinning structure are colored by Ackland method[3].

Fig. 6 shows a few layers of $(11\bar{2}0)$ planes sliced to reveal the plane of shear for $\{10\bar{1}2\}$ twinning colored by Ackland method[5]. The twinning boundary in the plane of shear forms a retangle starting from a circle. The retangle consists of four twinning planes which are straight in the figure.

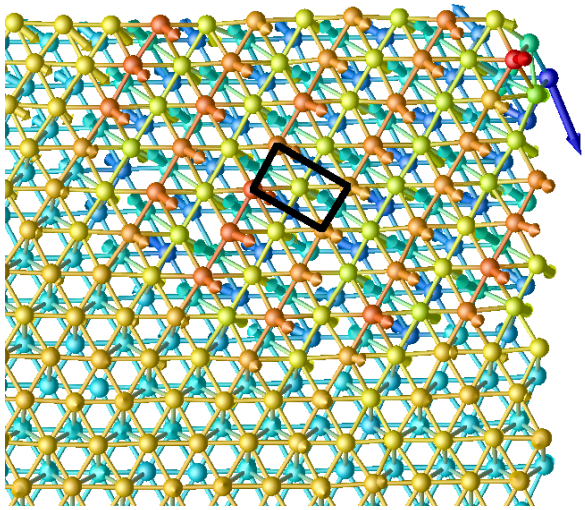

Figure 7. Slip vectors on a few layers of parent basal planes.

Slip vectors are shown in Fig. 7 for the atoms on a few layers of (0001) basal planes. The slip vector shows the movement of an atom relative to the neighbor atoms. Burger vector is the displacement vector of an atom to create a dislocation. Shuffling also causes the slip vector change as well as the Burger vector.

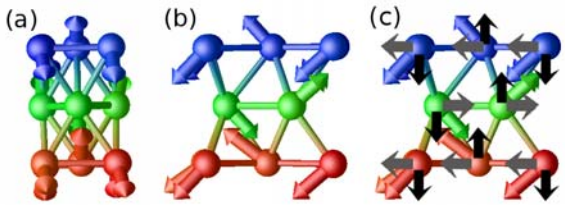

Figure 8. The slip vectors in rectangle region in previous figure is magnified (a) and its right side is viewed (b). The slip vectors are decomposed as two components (c).

Fig. 8 shows the slip vectors in the region indicated by black solid line rectangle in Fig. 7. Fig. 8(B) is the right side view of Fig. 8(A) and the prismatic plane of the parent crystal structure. Fig. 8(C) shows the decomposition of the slip vectors. The gray arrow represents a shuffling in c-direction. The black arrow represents shuffling on the second prismatic plane. The displacement due to dislocation is very small so that it is not noticable with bare eyes. The $\{10\bar{1}2\}$ twinning is shuffling dominant.

Our early twin structure just after nucleation is very different from a commonly expected one where a certain number of atomic layers of twin structure nucleate at a time by twinning dislocations[6]. The twin boundary shape is spherical. The twin nucleation point is always at the edge of the retangular rod. The thermal Brownian motion of atoms at the edge creates twin nucleation point because the atoms at edge have more freedom to move away from the crystal lattice position and form nucleation points. The spherical shape of the twin boundary surface doesn't continue because the growing speeds of the twin boundaries are not same. Each part of the twin boundary grows with a different velocity which depends on the boundary structures and the growing direction. As the twin region grows it might form the experimentally observed lenticular shape of twins.

Our overall simulation results suggest a surprising idea that the driving force to $\{10\bar{1}2\}$ twinning is tensile stress rather than shear stress. The $\{10\bar{1}2\}$ twinning forms by shearing and shuffling. The Burgers vector of twinning dislocation is extremely small and the shuffling is dominant. The shuffling lowers the energy of the system which is increased by applied tensile load. When the shear stress is applied to a crystal, dislocations are nucleated to accomadate the loading stress instead of the shear deformation of the the entire crystal. In hcp $\{10\bar{1}2\}$ twinning, the shearing load is not the main contribution to twinning nucleation but the tensile load is. The shear-dominant twinning nucleates and grows by resolved shearing load. The shuffling-dominant twinning nucleates and grows by the resolved loading stress which induces shuffling to lower the system energy, as, for example, the tensile loading stress in the current system does. More evidences will be investigated in the future.

References

[1] S.J. Plimpton: J. Comput. Phys., 1995, vol. 117, pp. 1-19, http:// lammps.sandia.gov/index.html.

[2] S. M. Foiles, M. I. Baskes, and M. S. Daw, Phys. Rev. B **33**, 7983 (1986).

[3] G. Voronoi, Reine Angew. Math. 134, 199 (1908).

[4] D. Y. Sun, J. W. Liu, X. G. Gong, and Zhi-Feng Liu, "Empirical potential for the interaction between molecular hydrogen and graphite," *PRB*, 75, 075424, 2007.

[5] G. J. Ackland and A. P. Jones, "Applications of local crystal structure measures in experiment and simulation," *PRB*, 73, 054104, 2006.

ACTIONS PLANNED FOR THE NEXT QUARTER

1. Perform the simulations of carbon nanotubes embedded in Mg matrix under tensile loading.
2. Study the twin nucleation dependence on temperature in Mg single crystal.
3. Investigate the twin nucleation process from surface corner.
4. Study the effects of temperature on twinning nucleation.

SUBTASK 1.6: DESIGN OPTIMIZATION

Team Members: Masoud Rais-Rohani, *K. Motoyama, M. Kiani (PhD Student), M. Islam (MS Student), and I Gandikota (MS Student)*

SUMMARY OF THE PROGRESS

Application of Carbon Fiber Reinforced Plastic (CFRP) in Auto Body Structure

In order to investigate the effect of material replacement to CFRP, two new models for crash and eigenvalue analyses have been developed by changing the material of the crash rail boxes of Dodge Neon from steel to CFRP. The CFRP crash rail box is made of Toray T700 carbon fiber UD that used by 2510 epoxy resin, and contains 20 layers as $[0/45/90/-45/0/0/0/45/90/-45]_{2S}$. The original full-scale model of Dodge Neon was developed by National Crash Analysis Center (NCAC) for the crash analysis, and in this study the Body In White (BIW) model has been developed in LS-DYNA and MSC Nastran. All the spot-welds and Rigid Body Elements for the Nastran model have been redesigned and changed, as the converted model introduced errors regard to the definition of these two special connector elements in each software. Table 1 shows the results of first 6 modes' (after 6 rigid modes) in eigenvalues of the BIW of Dodge Neon that the crash rail boxes have been steel and CFRP, the results have been obtained in LS-DYNA and MSC Nastran.

Table 1. Natural frequencies obtained from LS-DYNA and MSC Nastran for full-scale BIW of Dodge Neon with steel and CFRP crash rail boxes.

Mode Number	Frequency, Hz (LS-DYNA)		Frequency, Hz (MSC Nastran)	
	BIW-Steel Crash Rail Box	BIW-CFRP Crash Rail Box	BIW-Steel Crash Rail Box	BIW-CFRP Crash Rail Box
1	29.60	30.03	35.40	36.05
2	30.84	31.46	36.23	36.90
3	32.33	33.74	38.39	40.22
4	35.14	35.48	43.31	43.44
5	38.06	38.16	49.68	49.92
6	41.88	42.00	50.76	51.05

As general tendency, calculated frequencies of CFRP structure are higher than steel structures', and the weight of the crash rail boxes reduces from 13.12 kg to 5.12 kg.

In the next step of the weight reduction in auto body structure, besides the idea of replacing steel by CFRP, the body structure of Dodge Neon will be treated for optimization of both crash and vibration characteristics. For this reason, MSC Nastran will be used to perform the eigenvalue analysis of the BIW of Dodge Neon, and LS-DYNA for crashworthiness parameters. This activity is going on, and the needed information is being processed.

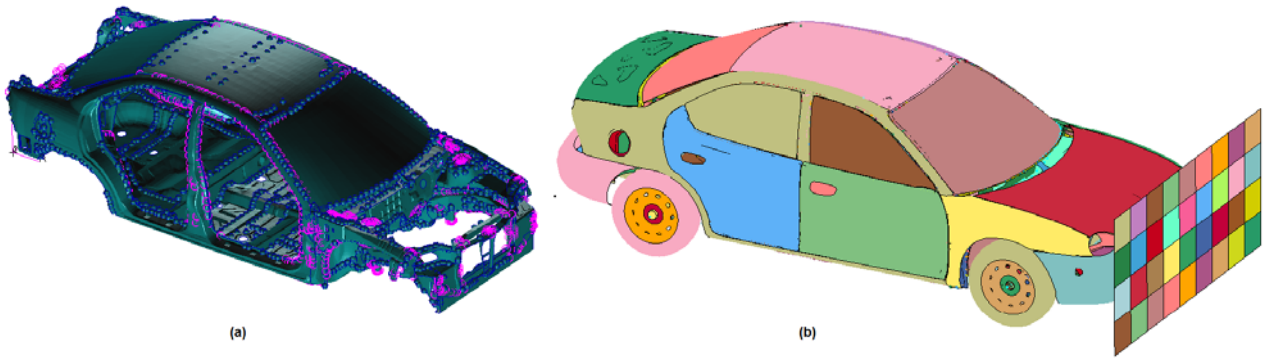

Figure 1. BIW of Dodge Neon converted from LS-DYNA to MSC Nastran (a); Crash model of Dodge Neon in LS-DYNA (b).

Welding Simulations and Validation

In continuation of our previous year's work, we have updated our finite element model for welding simulation of the Gas Metal Arc Welding (GMAW) of our simple lap joined experimental model. Also we have achieved good accuracy and established correlation between Finite Element(FE) simulation and experiment. The updated simulation model has been shown in Figure 1.

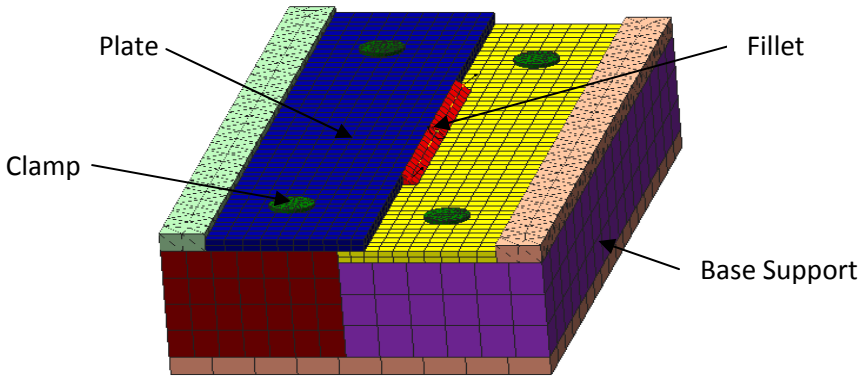

Figure 2. Updated Simulation model of simple plate lap joint.

The geometric model has been kept same as the previous one. However, major modifications have been done in heat source modeling and imposing boundary conditions. The heat input has been modeled as a moving heat source and the heat source dimensions have been determined based on the experimental weld cross sectional properties. Also, the release time of four clamps and cooling time have been adjusted to match the actual experimental conditions. Then we achieved good accuracy in temperature distribution over the plate. But we could not achieve good deformation result with the current version of Simufact.welding software. Thus, we conducted collaborative discussion with a software expert from our collaborator Simufact-Americas LLC to identify the problem. The software company has adjusted the threshold value of internal release force based on our test results in the latest

version of the software which will allow to obtain good deformation results including reasonable plate separation and bending.

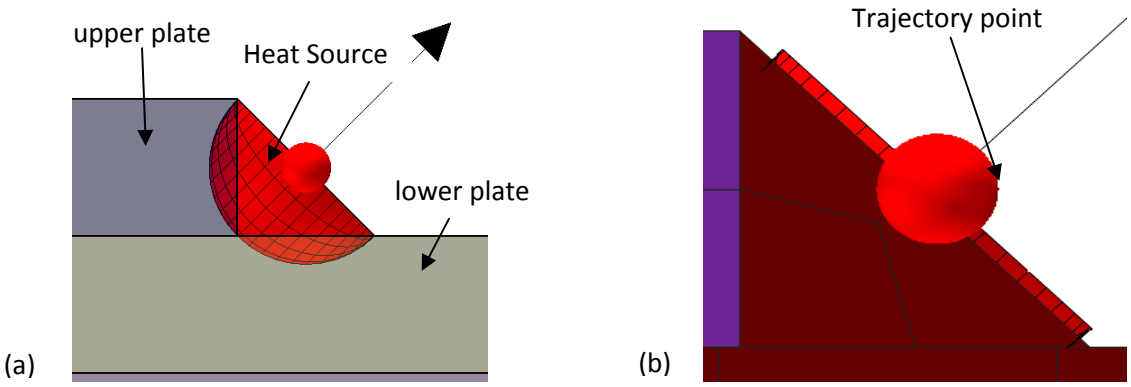

Figure 3. (a) Heat source shape covering entire fillet (b) Trajectory point of heat source across the fillet.

The initial simulation model has been updated in several steps for good agreement between simulation and experimental results. The correlation has been established for heat distribution, heat affected zone and weld induced deformation. Temperature result comparison has been shown in Figure 2. The experimental temperature measuring system can only measure temperature in the range from 80 ^{o}c to 1300 ^{o}c . For this reason, there is slight discrepancy between experimental and simulation results during the initial welding process.

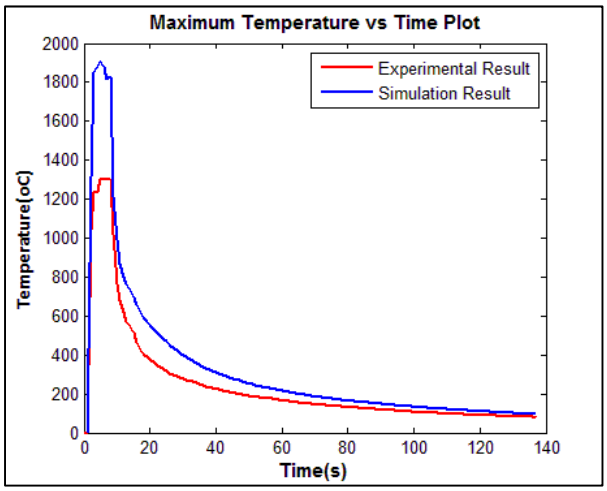

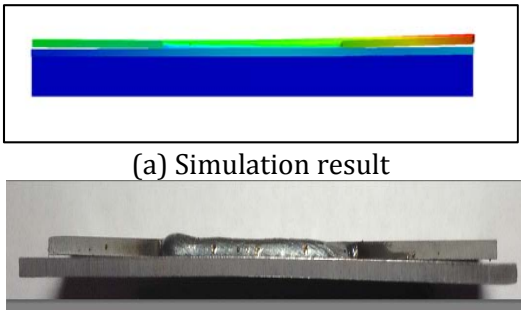

(a) Simulation result

(b) Experimental results

Figure 4. Plot of maximum temperature result plot. Figure 5. Comparison of plate bending pattern.

Correlation of weld induced deformation between experimental and simulation has been shown in the Figure 4 and Figure 5. It is observed that the deformation pattern of the upper plate is quite similar to that of experimental one. But the accuracy is poor for the lower plate. However, we had good discussion with simufact software expert from our collaborating company Simufact-Americas LLC. He has confirmed that it is possible to obtain good deformation correlating by using the latest version of Simufact welding.

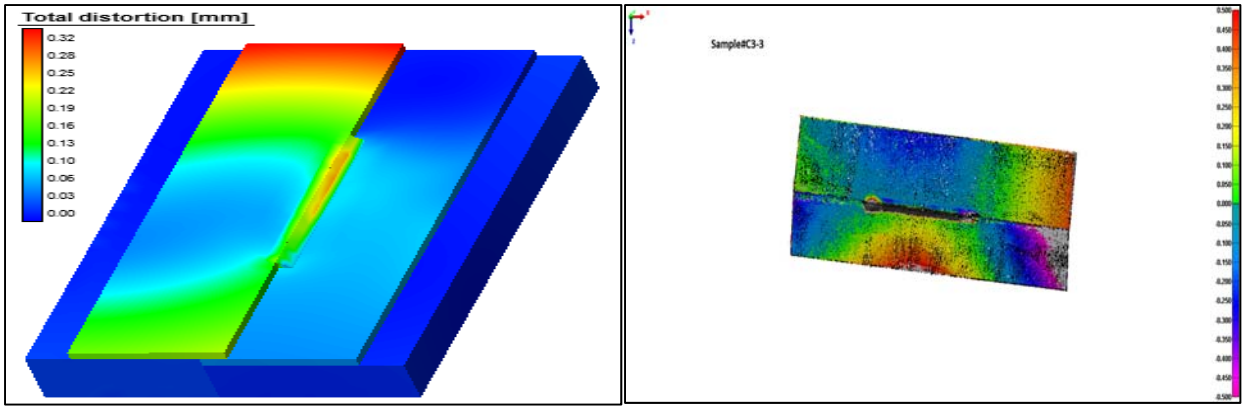

(a) Simulation result of deformation (b) Experimental result of deformation

Figure 5. Contour plot of weld induced deformation.

Collaboration with Simufact

We have conducted collaborative discussion with our collaborator Simufact-Americas LLC to improve simulation accuracy. They assigned a welding software expert to study our problem and identify the reasons of inaccuracy. We along with the software expert worked as a collaborative team to improve our accuracy. The collaboration has led to two important decisions:-

1. The base support of the setup must not be defined as 'component' or allowed to take part deformation. It's because if the base support is defined as 'component' , plates will be unable to undergo bending in bottom direction.

2. Comparison of simulation results and experiments has become difficult due to unavailability of all data such as clamping stiffness and origin point of distortion results.

ACCOMPLISHMENTS

1. Prepared and submitted DOE Quarterly and Annual reports.
2. Papers submitted for conference publication:
3. Kiani, M., Shiozaki, H., and Motoyama, K., “Using Experimental Data to Improve Crash Modeling for Composite Materials,” SEM XII International Congress & Exposition on Experimental and Applied Mechanics, 2012.
4. Completed the detailed modification of the 1996 Dodge Neon Model (LS-DYNA) with several thousand spotwelds for vibration analysis in MSC Nastran.
5. Replace crash rail boxes of Dodge Neon, and prepare appropriate model for both crash and vibration analysis in LS-DYNA and MSC.NASTRAN.
6. A correlation between FE simulations and experimental results has been established for plate lap joint model.
7. Prepared and submitted paper abstract for conference presentation:

E. Namazi, M. Islam , J. Rohbrecht, A. Buijk , T. Kurosu , B. Liu, K. Motoyama , " *Correlation of Finite Element Simulations and Experiments for Shielded Metal Arc Welding Processes*" , SMWC XV , 2012.

8. Conducted collaborative discussion with Simufact to improve simulation accuracy. They assigned a software expert to study our problem and identify the reasons of inaccuracy

ACTIONS PLANNED FOR THE NEXT QUARTER

1. Vibration and crashworthiness analysis of vehicle structures.
2. Multi-Objective optimization for Dodge Neon body structure by considering crashworthiness and vibration criteria.
3. Conduct simulation of lower arm and validate the simulation results with experimental results
4. Conduct large scale welding simulation using parallel computing facility of CAVS (Paper work to obtain license for CAVS has been done already.)
5. Implement GA based optimization scheme to optimize the welding process.

SUBTASK 1.7: SOLIDIFICATION MICROSTRUCTURE MODELING IN STEEL AND MG ALLOYS

Team Members: Sergio Felicelli, *Liang Wang*

SUMMARY OF THE PROGRESS

1. The 2D version of the lattice-Boltzmann – Cellular Automaton (LB-CA) model of solidification of dendritic microstructures was parallelized for execution in parallel processing HPC machines. A proposal for supercomputer computational time was submitted to the Extreme Science and Engineering Discovery Environment (XSEDE) project, funded by NSF. The proposal was accepted and we were awarded a startup allocation of 200,000 supercomputer units.
2. The parallelized version of the 2D code was run in Gordon and Kraken supercomputers of the XSEDE project, obtaining simulated dendritic microstructures of 1000+ dendrites growing under convection, which is unprecedented in current state of the art.
3. A 3D version of the code was developed to perform simulations of a 3D cubic dendrite growing in a solute field. The results were submitted for publication to Journal of Crystal Growth.

PUBLICATIONS/PRESENTATIONS

1. M. Eshraghi and S.D. Felicelli, "An implicit lattice Boltzmann model for heat conduction with phase change", *International Journal of Heat and Mass Transfer*, vol. 55, pp. 2420-2428 (Jan 2012)
2. M. Asle Zaeem, H. Yin, S.D. Felicelli, "Comparison of cellular automaton and phase field methods to simulate dendrite growth in hexagonal systems", *Journal of Materials Science and Technology*, in press (Jan 2012)
3. M. Eshraghi and S. Felicelli. Three dimensional simulation of solutal dendrite growth using lattice Boltzmann and cellular automaton methods. Journal of Crystal Growth (Under Revision), 2012.

ACTIONS PLANNED FOR THE NEXT QUARTER

1. Continue development of parallel versions of the dendrite growth model for execution in XSEDE resources. Improve performance and scalability.
2. Work on the 3D version of the code; solve mesh-induced anisotropy issue. Implement parallel version.
3. Submit publication on 2D parallel simulations

MISSISSIPPI STATE UNIVERSITY

Southern Regional Center for Lightweight Innovative Design

Phase IV
Quarterly Report
January – March 2012

For compliance with contract requirements of
Award DE-FC26-06NT42755

TASK 2
MULTISCALE MATERIALS MODELING AND CHARACTERIZATION OF STEEL ALLOYS

Submitted April 30, 2012

TABLE OF CONTENTS

Center for Advanced Vehicular Systems, Mississippi State University

Date: April 30, 2012

From: Paul Wang, Mark Horstemeyer

RE: SRCLID Phase IV Quarterly Report – January-March 2012

TASK 2: MULTISCALE MATERIALS MODELING AND CHARACTERIZATION OF STEEL ALLOYS

Principal Investigator: Hongjoo Rhee
Associate Director, CAVS
Mississippi State University (MSST)
200 Research Blvd
Mississippi State, MS 39762
(662) 325-9221; fax: (662) 325-5433; e-mail: hrhee@cavs.msstate.edu

Carol Schutte: Technology Area Development Manager
e-mail: carol.schutte@ee.doe.gov

Joseph Renk
email: joseph.renk@netl.doe.gov

Contractor: *Mississippi State University (MSST)*
Contract No.: *DE-FC26-06NT42755*

SUBTASK 2.1: MATERIALS DESIGN OF LIGHTWEIGHT ALLOYS

Team Members: Seong-Gon Kim, *H. Rhee, S. Kim, M.F. Horstemeyer, M.I. Baskes (LANL), L. Liyanage (PhD), M. Jones (MS)*

SUMMARY OF THE PROGRESS

The objectives were met by accomplishing the following:

1. Performed large scale molecular dynamics simulations with a new MEAM potential for Fe-C alloys to validate the thermal and mechanical properties.
2. Performed high strain rate tensile tests on the thermo-mechanically treated TRIP steel specimens followed by fractographical study to characterize the pre-straining and bake-hardening effects on the mechanical behavior of AHSS.
3. Carrying out heat treatments (*i.e.*, intercritical annealing followed by isothermal bainitic transformation), structure observation, and mechanical tests on TRIP steels to characterize the effect of altered microstructure on the strength-ductility combination of AHSS.

Structural and Elastic Properties of Cementite

We tested the present MEAM potential further by computing the structural properties of cementite including the equilibrium lattice parameters, the equilibrium volume per atom, and the heat of formation. These properties are presented in Table 1 with comparison to DFT, experiment, and interatomic potentials by Ruda et al [Ruda09] and Henriksson et al [Henr09]. MEAM prediction of the heat of formation of cementite is in excellent agreement with DFT and experimental data. Henriksson's potential also predicts a value in good agreement with DFT and experiment, while Ruda's potential predicts a much larger value. Lattice constants of the present MEAM and literature potentials [Ruda09, Henr09] agree well with experiment, while DFT predicts lower values. As a test of validity, the variation of cohesive energy with volume was calculated. Fig. 1 compares the energy vs volume curves for cementite generated by the present MEAM potential with DFT and experimental curves. During volume variation of cementite, the ratios between a, b and c lattice parameters were held constant. DFT overestimates the cohesive energy and underestimates the volume. Therefore, the DFT curve sits to the left of the experimental curve, and it is shifted vertically to the experimental cohesive energy at equilibrium volume to aid the comparison with the experimental curve. The experimental curve was generated by Murnaghan's equation of state [Murn44, Murn67] with the experimental bulk modulus, volume, and cohesive energy [Hagl91]. The experimental single-crystal bulk modulus of cementite has not yet been determined; therefore, the polycrystalline bulk modulus of cementite was used to generate the experimental curve.

Table 1. Material properties of cementite: the heat of formation $\Delta \boldsymbol{H_f}$ (eV/atom); the equilibrium volume $\boldsymbol{\omega_0}$ (Å^3/atom); the lattice parameters a, b, and c (Å). The predictions from the present work (MEAM) are compared with those from DFT and other interatomic potentials [Ruda09, Henr09]. Experimental values are given in parentheses.

Property	DFT (Expt.)	MEAM	Ruda	Henriksson
ΔH_f	0.01(0.05)	0.06	0.18	0.03
ω_0	8.49 (9.71)	9.49	9.11	9.33
a	4.91 (5.09)	5.05	5.14	5.09
b	6.63 (6.74)	6.69	6.52	6.52
c	4.38 (4.53)	4.49	4.35	4.50

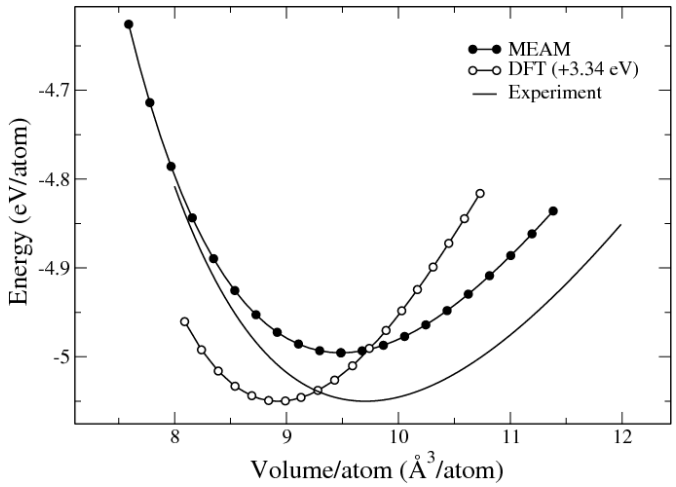

Figure 1. Comparison of energy vs volume curves for cementite. The solid curve is constructed from experimental values of the cohesive energy, polycrystalline bulk modulus, and equilibrium volume of cementite. For comparison, the DFT curve is shifted vertically to the experimental cohesive energy at the equilibrium volume.

Single-Crystal Elastic Properties

The elastic moduli of cementite were calculated and compared to DFT and the interatomic potentials by Ruda et al. [Ruda09] and Henriksson et al. [Henr09] as presented in Table 2. We used both $\delta = 0.5\%$ and $\delta = 0.1\%$ that produced the same result. These results show that the present MEAM potential for Fe-C alloy predicts cementite to be stable (positive elastic constants) and their values are reasonably close to those predicted by DFT. However, the present MEAM—and other interatomic potentials in the literature—could not reproduce the low value of C_{44} reported by DFT [Jian08].

Table 2. Single-crystal elastic moduli, C_{xy} (GPa) of cementite. The predictions from the present work (MEAM) are compared with those from DFT [Jiang2008] and other interatomic potentials [Ruda09, Henr09].

Property	DFT	MEAM	Ruda	Henriksson
C_{11}	395	303	263	363
C_{22}	347	216	219	406
C_{33}	325	307	247	388
C_{12}	158	126	176	181
C_{23}	163	110	143	130
C_{13}	169	157	146	166
C_{44}	18	249	77	91
C_{55}	134	236	95	125
C_{66}	135	227	123	134

Polycrystalline Elastic Properties

Theoretical upper and lower bounds for the polycrystalline bulk modulus (*B*) and shear modulus (*G*) were calculated using the single-crystal elastic constants according to methods by Reuss and Voigt [Jiang2008]. The true polycrystalline *B* and *G* were then estimated using Hill's average [Hill52, Jiang2008]. Polycrystalline elastic moduli predicted by our MEAM potential are presented in Table 3, in comparison with DFT, experiment, and interatomic potentials by Ruda et al. [Ruda09] and Henriksson [Henr09]. The elastic constants predicted by DFT are in excellent agreement with experiment. The present MEAM gives the best agreement with experiment among the three interatomic potentials for B; however, the present MEAM prediction of ν is significantly lower than its experimental value. Ruda's potential predicts the best agreement with experiment for *G* and ν.

Table 3. Polycrystalline cementite properties: bulk modulus *B* (GPa), shear modulus *G* (GPa), Young's modulus *Y* (GPa), and Poisson's ratio ν. The predictions from the present work (MEAM) are compared with those from DFT [Jiang2008], and other interatomic potentials [Ruda09, Henr09]. Experimental values are given in parentheses.

Property	DFT (Expt.)	MEAM	Ruda	Henriksson
B	224 (175±4)	174	183	234
G	72 (74)	146	69	114
Y	194 (200)	343	184	293
ν	0.36 (0.36)	0.17	0.33	0.29

Surface Energies

Calculations were performed on (001), (010), and (100) surfaces to determine the surface formation energy. Table 4 compares the surface formation energies of the present MEAM to DFT and the interatomic potential by Ruda et al. [Ruda09]. The atoms near the surfaces are fully relaxed to allow reconstruction if necessary. The predicted surface energies have the same order of magnitude as DFT results. However, the present MEAM gives a wrong order of stability among the three surfaces.

Table 4. Surface energies (J/m^2) of cementite. The predictions from the present work (MEAM) are compared with those from DFT [Chiou2003] and other interatomic potentials [Ruda09].

Surface	DFT	MEAM	Ruda
(001)	2.05	2.30	1.96
(010)	2.26	1.81	2.00
(100)	2.47	1.79	2.34

Phase Distribution of As-Received TRIP Steel

Area fraction analysis on different phases of the as-received TRIP steel was performed with Beraha's color etchant and in-house image analysis software. The specimens were etched for nearly 45 seconds and then observed through an optical microscope with UV-filtered light projection. The microscopic image obtained is depicted in Figure 2 and the phase volume fraction analysis result is shown in Figure 3, respectively. The outcome of the area fraction analysis was as expected as typical TRIP steels having ferrite as the dominant phase with approximately 7~15% retained austenite.

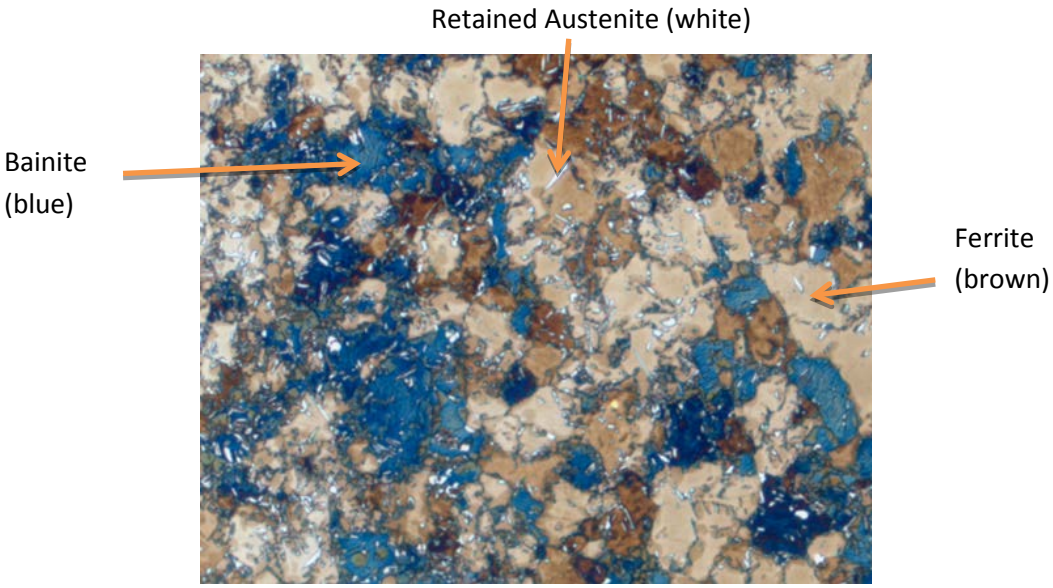

Figure 2. Optical microscopic image of as-received TRIP steel etched with Beraha's color etchant revealing distinctive constituent phases.

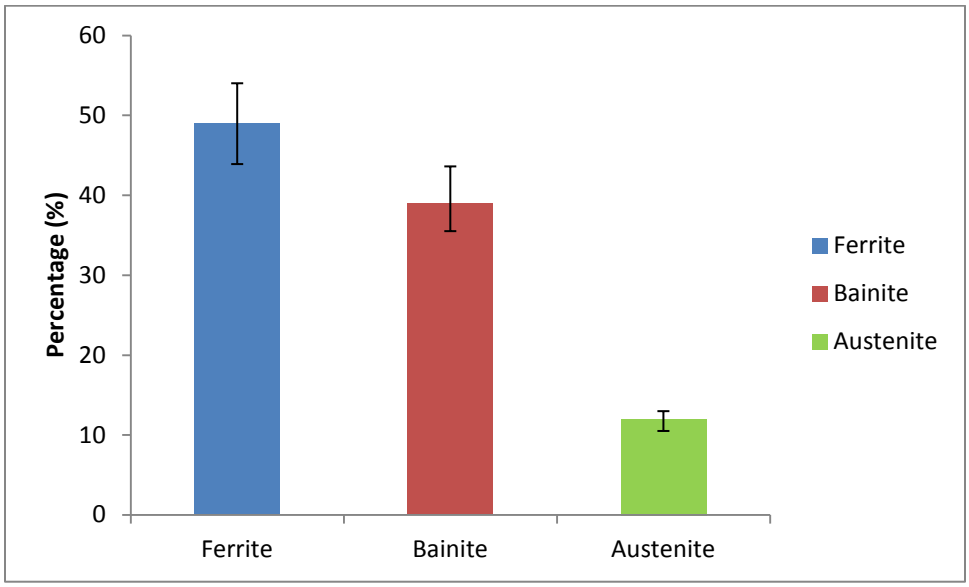

Figure 3. Area fraction analysis results on as-received TRIP steel.

Effects of Thermomechanical Treatments

High strain-rate (approx. 500/s) tensile Hopkinson Bar tests were performed on the TRIP steel specimens in order to investigate the effects of the phase volume fraction change on the mechanical behavior of the TRIP steel under higher strain rate regime. With specimens subjected to five different pre-conditioning protocols (i.e., as-received; 0, 1, 2, and 5% pre-strained and then baked), comparisons of the different cases are evident as illustrated in Figure 4. The higher pre-strained specimens were noted to have much higher flow stress. However, larger pre-strained specimens showed significant drop

in total elongation. It is also worth noting that the even paint-baking with no pre-straining simulation increased the strength of the material (e.g., bake-hardening).

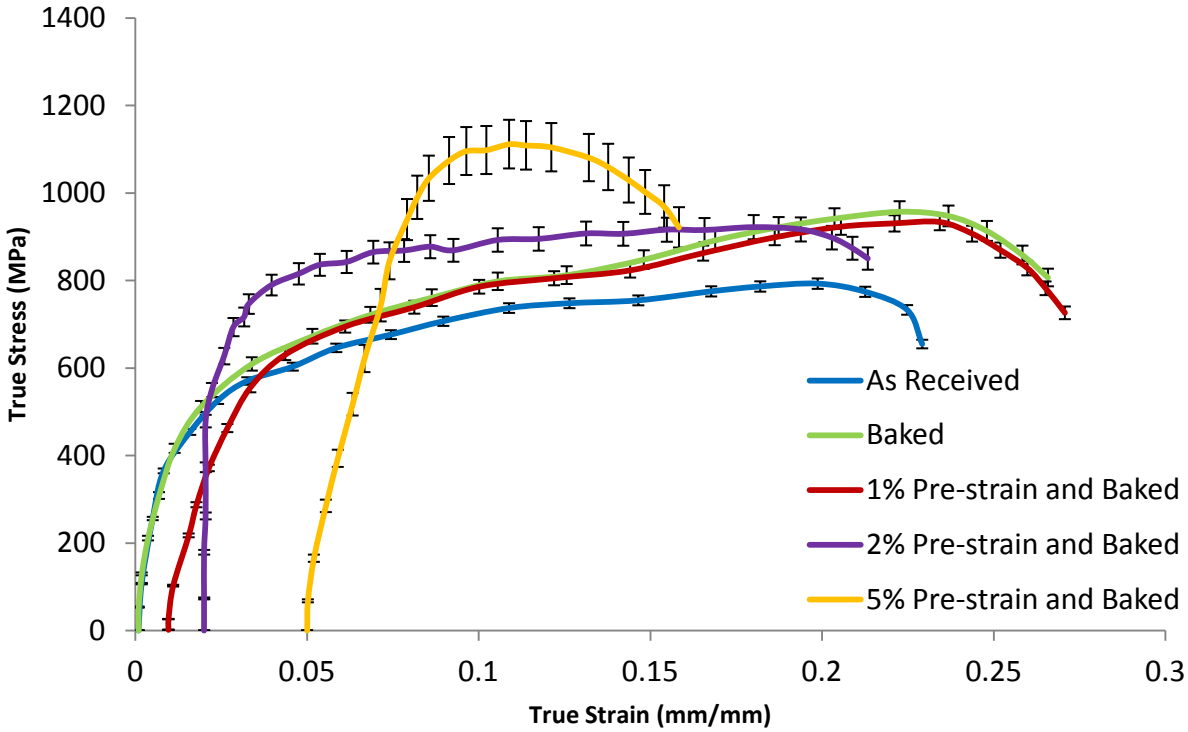

Figure 4. High strain-rate tensile Hopkinson bar tests at approx. 500/s strain-rate.

References

[Ruda09] M. Ruda, D. Farkas, and G. Garcia, Computational Materials Science 45, 550 (Apr. 2009), ISSN 09270256, http://linkinghub.elsevier.com/retrieve/pii/S0927025608005053.

[Henr09] K. Henriksson and K. Nordlund, Physical Review B 79, 1 (Apr. 2009), ISSN 1098-0121, http://link.aps.org/doi/10.1103/PhysRevB.79.144107

[Murn44] F. D. Murnaghan, Proceedings of the National Academy of Science 30, 244 (Sep. 1944).

[Murn67] F. Murnaghan, Finite deformation of an elastic solid (Dover New York, 1967).

[Hagl91] J. Haglund, G. Grimvall, and T. Jarlborg, Phys. Rev. B 44, 2914 (Aug 1991), http://link.aps.org/doi/10.1103/PhysRevB.44.2914.

[Jian08] C. Jiang, S. G. Srinivasan, a. Caro, and S. a. Maloy, Journal of Applied Physics 103, 043502 (2008), ISSN 00218979, http://link.aip.org/link/JAPIAU/v103/i4/p043502/s1&Agg=doi

[Hill52] R. Hill, Proceedings of the Physical Society. Section A 65, 349 (1952), http://stacks.iop.org/0370-1298/65/i=5/a=307

ACTIONS PLANNED FOR THE NEXT QUARTER

1. Construct and validate reliable interatomic potentials to model various phases of high-strength steel alloys
    a. MEAM potentials for V
    b. MEAM potentials for various combinations of elements for steel alloys (Fe-C-V).
2. Carry out heat treatments (*i.e.*, intercritical annealing followed by isothermal bainitic transformation), structure observation, and mechanical tests on TRIP steels to characterize the effect of altered microstructure on the strength-ductility combination of AHSS.

SubTask 2.2: Solidification and Phase Transformation in Steel Alloys

Please refer to Task 1, Subtask 1.7 Report.

SUBTASK 2.3: DESIGN OPTIMIZATION

Please refer to Task 1, Subtask 1.6 Report.

SUBTASK 2.4: CYBERINFRASTRUCTURE

Please refer to Task 1, Subtask 1.2 Report.

Southern Regional Center for Lightweight Innovative Design

Phase IV

Quarterly Report

October – December 2011

For compliance with contract requirements of
Award DE-FC26-06NT42755

TASK 3

MULTISCALE MATERIAL MODELS AND PROCESSING DESIGN FOR POLYMERIC MATERIALS

Submitted January 30, 2012

TABLE OF CONTENTS

Center for Advanced Vehicular Systems, Mississippi State University

Date: April 30, 2012

From: Paul Wang, Mark Horstemeyer

RE: SRCLID Phase IV Quarterly Report – January-March 2012

TASK 3: MULTISCALE MATERIAL MODELS AND PROCESSING DESIGN FOR POLYMERIC MATERIALS

Principal Investigator: Jean-Luc Bouvard
Associate Director, CAVS
Mississippi State University (MSST)
200 Research Blvd
Mississippi State, MS 39762
(662) 325-5575; fax: (662) 325-5433; e-mail: jeanluc@cavs.msstate.edu

Carol Schutte: Technology Area Development Manager
e-mail: carol.schutte@ee.doe.gov

Joseph Renk
email: joseph.renk@netl.doe.gov

Contractor: *Mississippi State University (MSST)*
Contract No.: *DE-FC26-06NT42755*

SUBTASK 3.1: POLYMER RESINS

***Team Members: J.L. Bouvard**, S. Nouranian, M. Tschopp*

SUMMARY OF THE PROGRESS

This quarterly report describes ongoing research in the multiscale modeling of polymers:

This section describes continuing efforts to understand the relevant molecular deformation mechanisms and quantify the internal structure evolution responsible for the different regimes (elasticity/yield/strain softening/strain hardening) observed during deformation of entangled polymers. There were several projects in this quarter and we will briefly discuss these.

- The ***first project*** continued our efforts to explore how deformation of amorphous polyethylene is influenced by the choice of ensemble and thermostat/barostat rates for the directions lateral to the loading direction, which can introduce overall stress state differences. Again, while there are a wide range of potential rates for the thermostat and barostat in the lateral directions, we focused on the four extreme cases: isothermal-isobaric (NPT) ensemble, isenthalpic-isobaric (NPH) ensemble, canonical (NVT) ensemble, and microcanonical (NVE) ensemble. Several conclusions can be drawn from this study:

1. The following analysis concentrates on the pressure dissipation boundary conditions (NPT, NPH). The bond length and bond angle distributions do not change significantly as a function of strain. For the case of increased temperature, there is a slight broadening of the symmetric distributions but no increase or decrease of the distribution. Rather, the large contribution of bond stretching and bond bending to the macroscopic stress are due to the re-orientation of the polymer chain segments in the direction of loading, which results in a larger force being resolved in the direction of loading. The increase in temperature for the NPH case results in a faster rate of re-orientation of the polymer chain segments, which results in a higher stress in the direction of loading, but this is offset by the stress contribution of the kinetic energy component in molecular dynamics simulations.
2. The chain entanglement decreases as a function of strain with a large rate of decrease in the strain hardening regime (strain>0.5). The entanglement is not affected very much by the thermostat (NPT versus NPH) but does show some variation between the twelve instantiations studied for each condition.
3. The conformational changes from *gauche* to *trans*, and vice versa, result in non-negligible changes to the energy, but very little change to the macroscopic stress. In other words, conformational changes contribute more to the deformation kinematics (i.e., texture) and the ability of the polymer chains to align in the direction of loading than to the actual load carrying capacity. The change in the dihedral angle distribution as a function of strain is a result of both *gauche->trans* and *trans->gauche* changes at different rates (~2.5-3.0 times faster for *gauche->trans*). The increase in temperature for the NPH case results in a faster rate of change for the *gauche* and *trans* conformations.

Additionally, we have assembled a simulation test matrix (Table 1) for investigating strain rate effects and size effects for amorphous polyethylene. Different polymer configurations were cooled from 500K to 100K, equilibrated and stretched with different strain rates until 100% extension. Using information from simulation the stress-strain and energy partitioning graphs were plotted. The table of conducted simulations is provided below (with ok meaning that the simulations were run). The chain length for these simulations was 1,000 monomers, so 500 chains is equivalent to 500,000 united atoms. In this set of tests, we examined both the stress-strain response and energy evolution as a function of strain (Figure 1).

Table 1. Test matrix for exploring strain rate and size effects

		Number of chains					
		10	20	50	100	200	500
Strain Rate, 1/s	10^9	ok	ok	ok	ok	ok	ok
	10^{10}	ok	ok	ok	ok	ok	ok

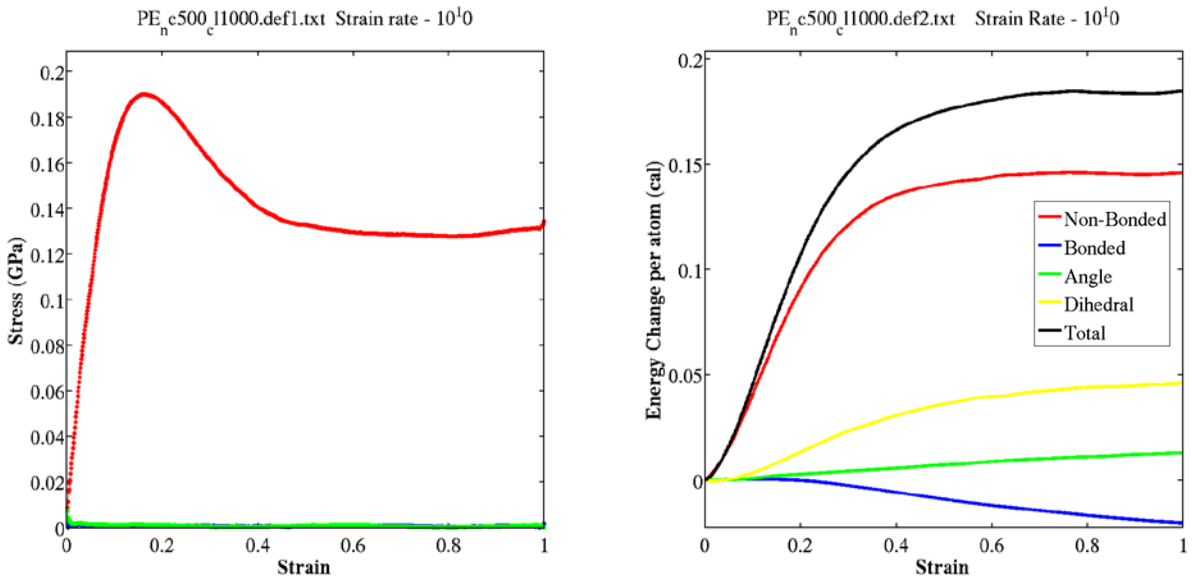

Figure 1. Example plots of stress-strain behavior (left) and energy evolution (right) for 500 1000-mer chains at a true strain rate of 10^9 s^{-1} and 100 K. The characteristic yield peak of thermoplastic polymers is clearly evident, which mainly corresponds to increases in non-bonded and total energy.

These simulations will be used to find the appropriate chain numbers and strain rates for subsequent molecular dynamics simulations of mechanical testing under tension and compression, including unloading and thermomechanical cycling. Interestingly, low temperatures (glassy state) and large sizes allowed us to recreate the characteristic experimentally-observed yield peak of glassy polymers at lower strain rates (e.g., Fig. 1). This is important for follow-up studies under different stress states.

- The ***second project*** focuses on developing a potential for polymer systems (starting with an interatomic potential for hydrocarbons) using a modification to the modified embedded atom method (MEAM) formalism. This semi-empirical many-body potential, which is based on the density functional theory and pair potentials, was parameterized for the homologous series of alkanes up to *n*-octane including select isomers. It was validated and tested for complex alkane structures and polyolefins, i.e., polyethylene and polypropylene. Although the MEAM formalism has traditionally been applied to atomic systems with predominantly metallic bonding, the current work demonstrates, ***for the first time***, the possibility of extending the applicability of the potential to complex molecular systems, such as hydrocarbons and polymers. Since the MEAM potential has already been parameterized for a large number of metallic unary, binary, ternary, carbide, and hydride systems, it can now be applied to complex systems involving, for example, polyolefin-metal interfaces.

  The MEAM formalism requires fourteen independent model parameters for each element: four parameters for the universal equation of state, 8 parameters for the electron densities and the embedding function, and 2 parameters for the screening factor. In this work, elements

carbon (*C*) and hydrogen (*H*) and the diatomic *CH* were parameterized for hydrocarbons. The reference structures were diamond for carbon, the diatomic H_2 for hydrogen, and the diatomic *CH* representing the characteristic *CH* bond in hydrocarbons. The parameters were fit to the experimental bond distances, bond angles, and atomization energies of the alkane homologous series up to *n*-octane with their select isomers. Some of the fittings were done to the calculated atomization energies by first principles. The parameterization procedure involved Monte Carlo simulations of the equilibrium energies, bond distances and bond angles for the hydrocarbon structures. All energy minimizations and molecular dynamics simulations were performed using an atomistic simulation software package (DYNAMO) first developed by Daw and Baskes.

The development of the interatomic potential for the atomistic simulations of polymers based on the modified embedded-atom method (MEAM) has been ongoing. The initial set of parameters, fitted to the first-principles and experimental data for the homologous series of alkanes during the previous quarter, was able to capture the energetics and structures (bond distances and angles) of these molecules as well as those of the polyolefins (polyethylene and polypropylene). To further validate and test these parameters, a series of molecular dynamics simulations were performed on different gaseous and liquid methane, ethane, propane, and butane systems using NVT and NPT ensembles (constant N=number of molecules, V=volume, P=pressure, and T=temperature). The simulations were run on DYNAMO, a custom serial code, first developed by Daw and Baskes, for atomistic simulations based on the MEAM potential. The simulations were performed at different temperatures and densities to generate the pressure-volume-temperature (PVT) data for the saturated hydrocarbon systems. After system equilibration, the PVT behavior (determined by the simulations) was compared to the experimental data. Further fine-tuning of the MEAM parameters was necessary to match MEAM results with experimental results. The PVT behavior is influenced by the intermolecular van der Waals interactions and the MEAM potential was parameterized for them. Finally, at the current stage, the MEAM potential has been parameterized to capture all the necessary energetic, structural, and physical features of saturated hydrocarbons. In Figure 2, snapshots of the final NVT-equilibrated systems for methane and propane are shown. The methane system was composed of 100 molecules (500 atoms) and the propane system comprised 80 molecules (880 atoms).

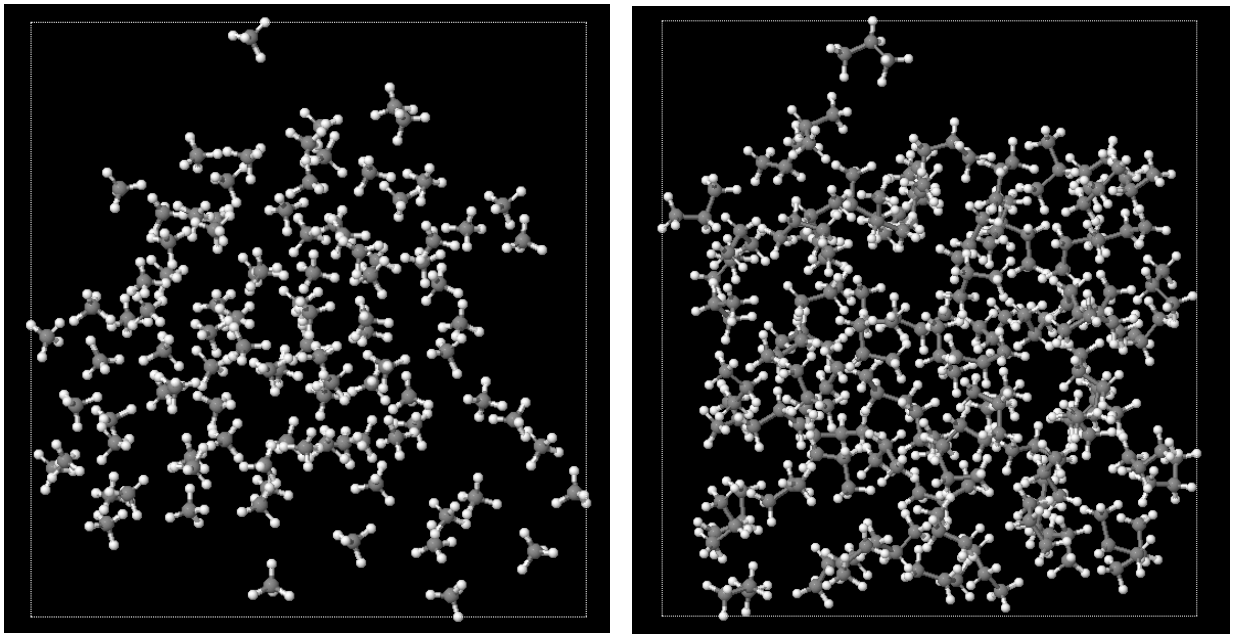

Figure 2. a) A snapshot of the NVT-equilibrated methane system with 100 molecules (500 atoms) at T=298 K and ρ =0.401 g/cm^3. b) A snapshot of the equilibrated propane system with 80 molecules (880 atoms) at T=280 K and ρ =0.521 g/cm^3. Both systems were equilibrated for 30 ps.

Next, the new set of MEAM parameters will be used to generate the stress-strain response of a representative polypropylene system. The mechanical properties, such as Young's modulus and Poisson's ratio will be calculated by NPT dynamics simulations using the MEAM potential. These results will be compared to the experimental data. Once the MEAM potential is fully parameterized for saturated hydrocarbons, it will be parameterized for double and triple C-C bonds (unsaturated hydrocarbons) and new elements (O and N) and their respective bonds with carbon will be introduced into the MEAM potential. The final objective is to be able to perform dynamics simulations of complex polymer systems (one-, two-, or multiphase), such as thermoset vinyl ester and its nanocomposites, and study complex failure phenomena at the molecular scale. The MEAM potential is capable of handling defects and interfaces smoothly, which makes it a strong tool for the future studies of complex polymer failure phenomena, polymer/metal interfaces, polymer nanocomposites, etc.

Future work will refine the MEAM potential by testing and validating using a variety of dynamics simulations for different material systems.

Actions Planned for the Next Quarter

1. The parameters of the ISV model will be calibrated with experimental data on VE available.
2. Future work will investigate the evolution of the internal structure of thermosetting polymer resins using MD simulations.

SUBTASK 3.2: STRUCTURAL NANOCOMPOSITES

***Team Members:* T.E. Lacy**, *H. Toghiani, C.U. Pittman Jr., J. Yu (postdoc), S. Nouranian (postdoc), C. Jang (PhD student), J. Nall (undergraduate student)*

SUMMARY OF THE PROGRESS

This quarterly report reflects ongoing research in the multiscale modeling of vapor-grown carbon nanofiber (VGCNF)/vinyl ester (VE) nanocomposites:

1. Molecular dynamics (MD) simulations were performed to create a series of crosslinked vinyl ester matrices with a larger repeating unit cell using Materials Studio® v5.5 [1]. This larger cell (40.6×40.6×40.6 $Å^3$) contained twice the number of monomer molecules of the smaller unit cell (32.2×32.2×32.2 $Å^3$) considered previously. The purpose of these simulations was to compare the volume shrinkage, glass transition temperature (T_g) and elastic moduli to those predicted from the simulations of crosslinked network structures performed in the smaller cell. If both simulations led to comparable results, then the smaller cell could be reliably used to generate representative predictions. These simulations were also based on the VE curing reaction through specification of the key aspects of the free radical polymerization such as region-selectivity (head-to-tail chain propagation), determination of the appropriate reaction distances, monomer relative reactivity ratios, and growing radical site concentrations as shown in Figure 1.

Figure 1. A graphical display of the RRV algorithm for vinyl ester free radical polymerization employing regioselectivity, the close distance criteria, and monomer relative reactivity ratios. Two reactive tail atoms (M_1 and M_2) are found from a styrene growing radical within the reaction cutoff distances (R_{11} and R_{12}).

Volume shrinkage, T_g, and tensile elastic constants of the equilibrated structures were also calculated for the larger repeating unit cell. The T_g (Figure 2) and the isotropic Young's moduli (Table 1) were compared with the values for the smaller unit cell and available experimental data. The T_g for the VE cured to four chain ends in a large repeating unit cell was also close to that for two chain ends in a smaller repeating unit cell. The crosslinking density of four chain ends in a larger repeating unit cell was the same as that for two chain ends in a smaller repeating unit cell. The Young's modulus is higher (8.98 GPa) at the highest crosslinking density simulated (larger unit cell, 98% conversion, and two chain ends) as shown in Table 1. The simulated resin with four chain ends in the larger cell gave a modulus of 6.90 GPa. This is in close agreement with the modulus of 7.05 GPa

predicted for two chain ends in the smaller unit cell, where these two resins have the same density of crosslinks.

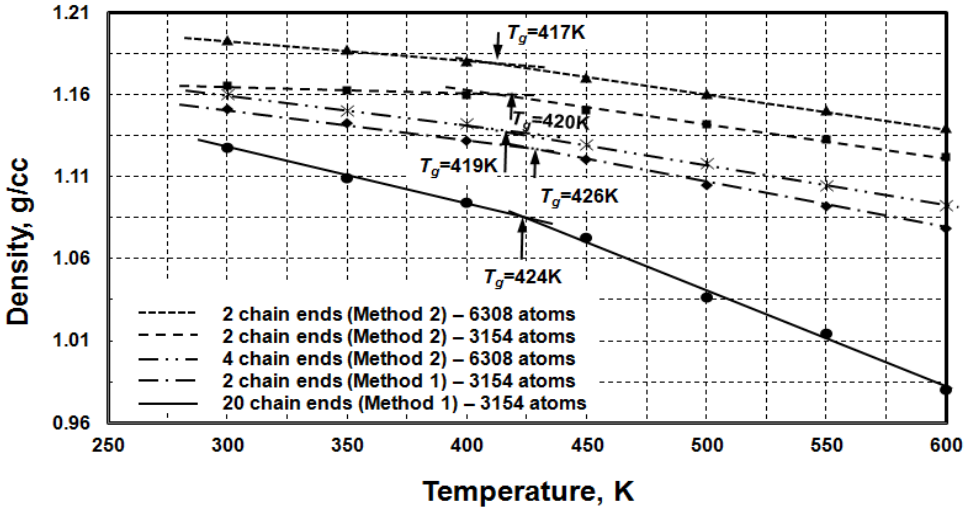

Figure 2. Glass transition temperatures (T_g) for cured VE resins simulated by multiple chain growth and single chain growth (Methods 1 and 2, respectively) at 98% conversion. T_g values from Method 1 with different crosslinking densities are very close to each other and also close to that predicted by Method 2. The experimental T_g for Derakane 441-400 VE resin is 410 K. Glass transition temperature (T_g) for the VE cured to four chain ends in a large repeating unit cell is also close to that of two chain ends in a smaller repeating unit cell simulated by Method 2. The crosslinking density of these two VE resins is the same.

Table 1. Young's modulus of VE resins[a] cured by multiple chain (Method 1) and single chain (Method 2) growth methods to 98% conversion.

Repeating Unit Cell	Curing Method	Chain Ends Present	Young's Modulus (GPa)
$[32.2\ Å]^3$	1	20	3.95
$[32.2\ Å]^3$	1	16	4.11
$[32.2\ Å]^3$	1	8	4.94
$[32.2\ Å]^3$	1	2	5.79
$[32.2\ Å]^3$	2	2	7.05
$[40.6\ Å]^3$	2[b]	4	6.90
$[40.6\ Å]^3$	2[b]	2	8.98
—	Experiment[c]	—	3.40

[a]The VE resins in this work mimicked those in Derakane 441-400 VE resin. The multiple chain (Method 1) and single chain (Method 2) growth methods used here were performed to the point where the number of chain ends was two.
[b]These simulations were performed with a larger repeating unit cell containing 6308 atoms.
[c]Ashland Co. The lower experimental value is due to the fact that a 98% conversion to equivalent crosslink densities, particularly those represented by two and four chain ends, are not, in general, experimentally achieved.

2. The Effective Continuum Micromechanics Analysis Code (EC-MAC) was modified and extended to predict the effective thermal and electrical conductivities of composites containing multiple distinct nanoheterogeneities (fibers, spheres, platelets, voids, etc.) each with an arbitrary number of coating layers based upon either the modified Mori-Tanaka method (MTM) or self-consistent method

(SCM). A parametric study was performed to investigate the effect of nanoreinforcement-resin interphase properties and voids on calculated effective electrical conductivities ($\bar{\sigma}$) of VGCNF/VE composites. Figure 3 contains a plot of the effective electrical conductivities as a function of heterogeneous volume fraction, calculated using the modified MTM module within EC-MAC, for VGCNF/VE composites containing three-dimensional (3D) randomly oriented nanofibers with/without coating and voids. The coating thickness used was one-tenth of the nominal nanofiber outer radius (i.e., t/R = 0.1). For composites containing 2v% of VGCNFs, application of a thin highly conductive coating to the outside of the primary reinforcement phase can lead to a substantial increase in $\bar{\sigma}$. At 2v% of VGCNFs, 0.49v% of synthetic diamond coating (corresponding to t/R = 0.1) led to a 22% improvement in $\bar{\sigma}$. Hence, it may be possible to coat reinforcements with extremely thin electrically conductive layers to enhance PMC performance. Also included in the figure is a plot of $\bar{\sigma}$ for composites containing equal volume fractions of VGCNFs and spherical voids (i.e., $c_f = c_v$). As expected, the presence of 2v% of voids led to roughly a 2% decrease in $\bar{\sigma}$. Figure 4 includes a plot of effective electrical conductivities for carbon black rod/ polyaniline composites. In the figures, both the modified MTM and SCM were employed in the calculations. These results, in combination with previous results for mechanical properties, suggest that EC-MAC is well suited for tailoring composite materials for multifunctionality.

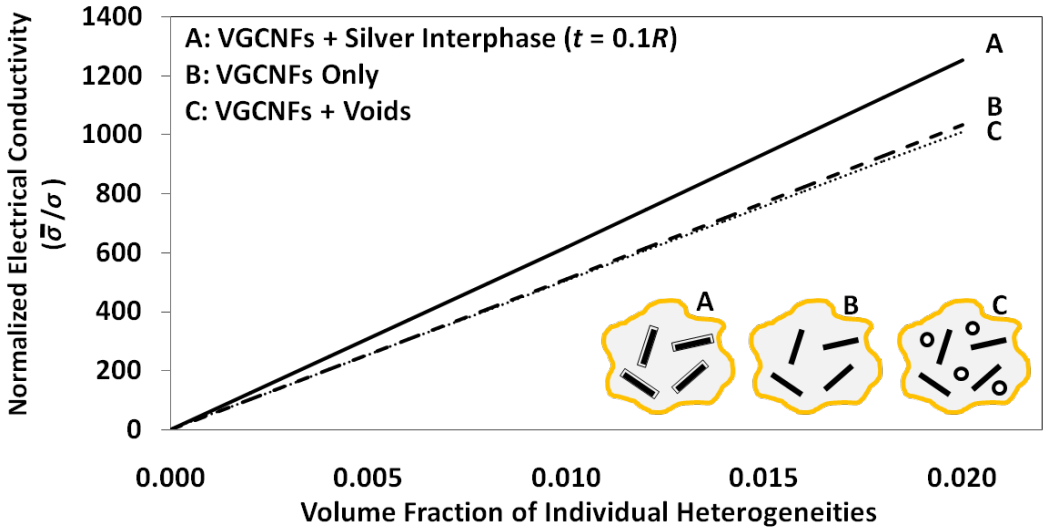

Figure 3. Predicted effective electrical conductivities for composites containing 3D randomly oriented VGCNFs (L/D = 1000) with and without a silver interphase, and voids ($c_f = c_v$).

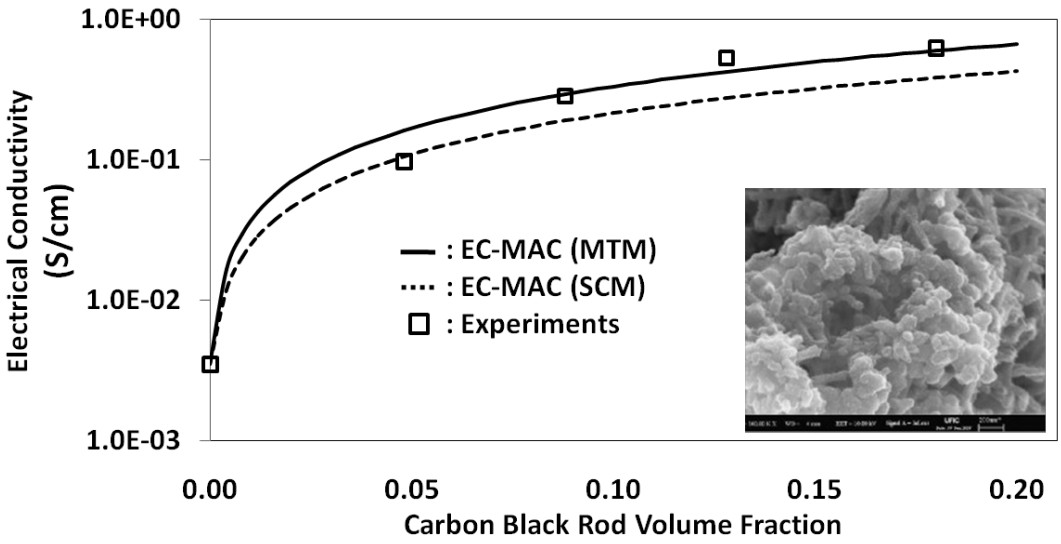

Figure 4. Measured [2] and predicted effective electrical conductivities for carbon black rod /polyaniline composites (inset adapted from [2]).

3. A multiscale modeling methodology was developed that incorporates a statistical distribution of fiber strengths into coupled micromechanics/finite element (FE) analyses. A parametric study using the NASA Micromechanics Analysis Code with the Generalized Method of Cells (MAC/GMC) was performed to assess the effect of variable fiber strengths on global composite failure at the repeating unit cell (RUC) level for an SCS-6/TIMETAL 21S material system. Five different doubly-periodic RUCs were analyzed in this study with each RUC having 1, 4, 9, 25, and 49 fiber subcells, respectively, while maintaining a constant fiber volume fraction of 25%. Figure 5 shows the 2x2 and 10x10 RUCs recognizing that the 10x10 RUC can be subdivided into 25 2x2 RUCs. Through randomly distributing fiber strengths to individual subcells based upon a two parameter Weibull cumulative distribution function obtained from vendor fiber strength data, the progressive failure behavior of an RUC was simulated. By increasing the number of fiber subcells while maintaining a constant fiber volume fraction, a strength distribution within the RUC more consistent with experimental observations was simulated resulting in a lower RUC-averaged maximum stress. Through incorporating random fiber strength values into a global FE framework using the hybrid code, FEAMAC, which couples MAC/GMC with ABAQUS Standard or Explicit, the effect of a stochastic distribution of fiber strengths at the FE level was also investigated for a SCS-6/TIMETAL 21S tensile dogbone specimen using 2x2 and 4x4 RUCs. While a constant strength value for all fiber subcells resulted in a symmetrical failure behavior inconsistent with typical experimental observations (Figure 6a), by incorporating random strength variations into the micromechanics calculations that feed into global FE simulations, a more distributed and progressive failure occurs as shown in Figures 6b-6c. When a strength distribution is employed, fiber failures initiate in a random fashion throughout the specimen and progress until the ultimate strength is reached. Elements continue to experience increased fiber failures until localization occurs leading to ultimate failure of the entire cross-section. With the 4x4 RUC FE simulations, some load shedding within an element is possible once initial fiber failure occurs. However, once fiber failure initiates in a 2x2 RUC (1 fiber subcell), the load is shed to neighboring elements, increasing the likelihood of localization. This will serve to

reduce the predicted composite ultimate strength which explains why the 4x4 RUC obtained a higher average strength than the 2x2 RUC as well as more global fiber subcell failures. Regardless of RUC architecture, stress/strain results agreed well with experimental data as shown in Figure 7. Furthermore, this methodology developed in this work could be employed for any fiber strength distribution, and could be readily used to model unidirectional, woven, and/or braided fiber composites. This work is currently being extended to simulate the progressive failure behavior of E-glass/vinyl ester composite flexure specimens.

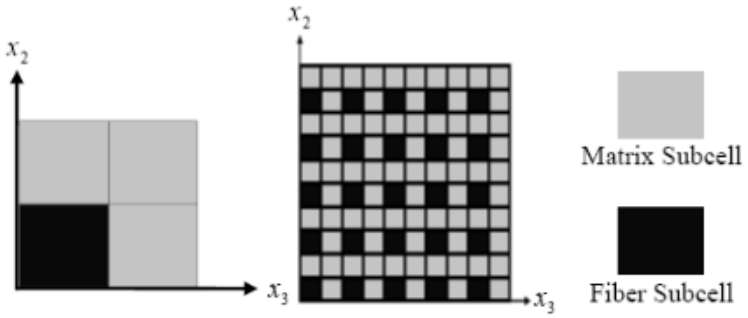

a) b)

Figure 5. Microstructural representation of a unidirectional SiC/Ti composite for a) a 2x2 subcell RUC and b) a 10x10 subcell RUC.

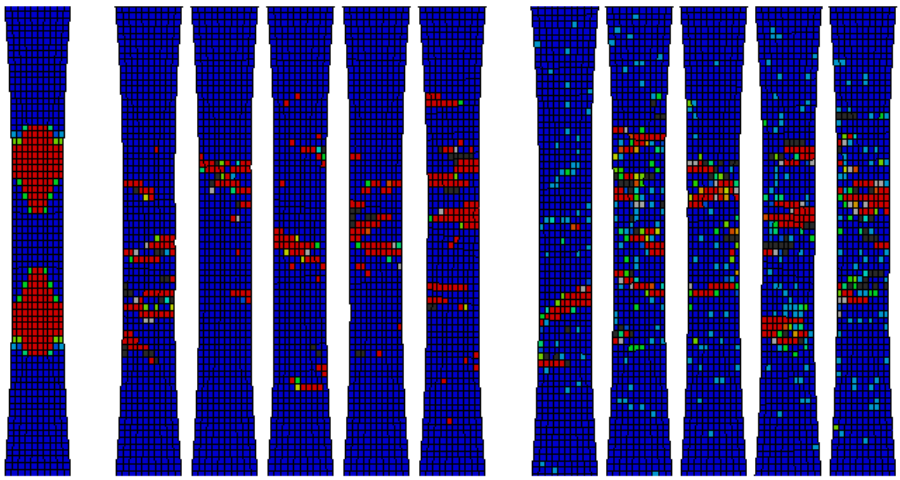

a) b) c)

Figure 6. Distribution of fiber failures within the global FE mesh after the onset of localization for a) 2x2 RUC with a constant strength value for all elements and b) five 2x2 RUC and c) five 4x4 RUC distributed strength simulations where blue represents no failure and red indicates complete fiber subcell failure for a given element.

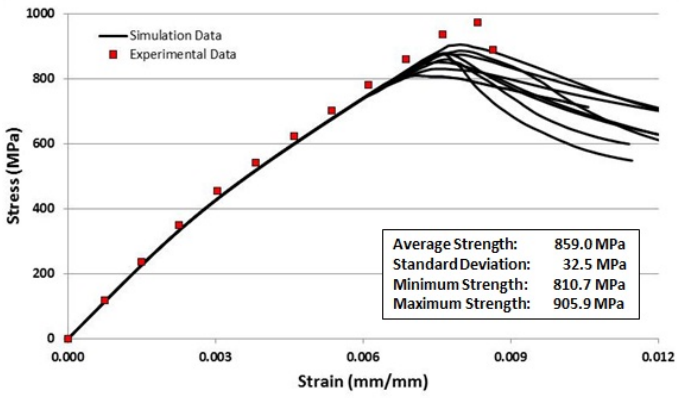

a)

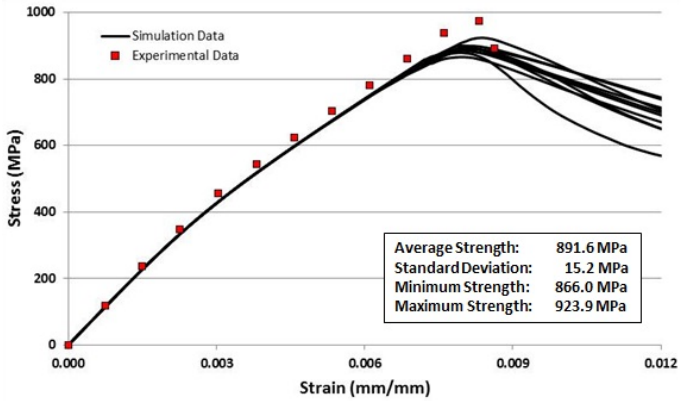

b)

Figure 7. Global stress-strain response of a longitudinally reinforced MMC for simulations using an a) 2x2 RUC (one fiber subcell) and b) 4x4 RUC (4 fiber subcells)

4. In a continuing effort, continuous E-glass woven fabrics were infused with either neat VE resin or with VE resin reinforced with 0.5 phr VGCNFs using a Vacuum Assisted Resin Transfer Molding (VARTM) process. One goal of this work is to minimize the VGCNF filtering by the woven fabric. Several techniques have been employed to improve the distribution of carbon nanofibers throughout the hybrid composite. These include incorporation of a layer of resin transfer medium adjacent to the mold surface to improve liquid nano-phased resin flow during the infusion process, reducing the amount of VGCNFs, and addition of more styrene to liquid resin. The latter two modifications are aimed at reducing the nano-phased resin viscosity. Based upon visual inspection of cured laminates, such improvements in fabrication and processing lead to better nanofiber dispersion. Scanning electron microscopy (SEM) images and other techniques will be used to quantify the degree of VGCNF filtering. Three-point bend flexural specimens are being fabricated from E-glass/VE and E-glass/VGCNF/VE laminates in accordance with ASTM D7264.

5. The effect of a methacrylate-based coupling agent in combination with oxidized VGCNFs (PR24-XT-LHT-OX, Applied Sciences, Inc.) on nanocomposite tensile and compressive properties was investigated. Nanocomposite specimens were fabricated with Derakane 441-400 VE resin incorporating 0.5 parts per hundred parts (phr) of oxidized VGCNFs. Other specimens were made with 0.5 and 1.0 phr of surface-functionalized oxidized VGCNFs. These VGCNFs had been

functionalized previously with 3-(trimethoxysilyl) propyl methacrylate (coupling agent). After surface functionalization, the VGCNFs dispersed better when stirred in hexane or tetrahydrofuran (THF). The methacrylate groups of the coupling agent were to be reacted during curing with the VE resin forming strong covalent bonds. Nanocomposites properties were normalized with those for the neat VE specimens. Dogbone-shaped tensile specimens were fabricated and tested according to ASTM D638 to determine stiffness, strain at failure, and ultimate strength. Cylindrical compression specimens were fabricated and tested according to ASTM D695 to determine yield strength and ultimate strength.

References

1. Accelrys, Inc. http://accelrys.com/products/materials-studio/ (date accessed: March 1, 2012).
2. Reddy, K.R., Sin, B.C., Ryu, K.S., Noh, J., and Lee, Y. 2009, "In situ self-organization of carbon black-polyaniline composites from nanospheres to nanorods: synthesis, morphology, structure and electrical conductivity," *Synthetic Metals*, 159, 1934-1939.

PUBLICATIONS/PRESENTATIONS

Journal Publications

1. Jang, C., Nouranian, S., Lacy, T.E., Gwaltney, S.R., Toghiani, H., and Pittman, Jr., C.U., 2012, "Molecular Dynamics Simulations of Oxidized Vapor-Grown Carbon Nanofiber Surface Interactions with Vinyl Ester Resin Monomers," *Carbon*, 50(3), 748-760.
2. Yu, J., Lacy, T., Toghiani, H., and Pittman Jr., C.U. "Effective Property Estimates For Composites Containing Multiple Nanoheterogeneities: Part I Nanospheres, Nanoplatelets, & Voids," *Journal of Composite Materials*, Pre-published online, DOI: 10.1177/0021998312442557.
3. Yu, J., Lacy, T., Toghiani, H., and Pittman Jr., C.U., 2012, "Effective Property Estimates for Composites Containing Multiple Nanoheterogeneities: Part II Nanofibers and Voids," *Journal of Composite Materials* (In Press).
4. Jang, C., Lacy, T.E., Gwaltney, S.R., Toghiani, H., and Pittman, Jr., C.U., 2011, "A Relative Reactivity Volume Criterion for Crosslinking: Application to Vinyl Ester Resin Molecular Dynamics Simulations," Submitted to *Macromolecules* (Under Review – Revised version submitted).
5. Nouranian, S., Toghiani, H., Lacy, T.E., Pittman, Jr., C.U., and DuBien, J.L., 2012, "Effects of Formulation, Processing, and Temperature on the Viscoelastic Properties of Vapor-Grown Carbon Nanofiber/Vinyl Ester Nanocomposites," Submitted to *Polymer Testing* (Under Review).
6. Nouranian, S., Lee, J., Lacy, T.E., Toghiani, H., Pittman, Jr., C.U., 2012, "Effects of Molding and Curing Atmosphere on the Flexural Properties of Vinyl Ester," Submitted *Polymer Testing* (Under Review).
7. Torres, G.W., Nouranian, S., Lacy, T.E., Toghiani, H., DuBien, J.L., Pittman, Jr., C.U., 2012, "Statistical Characterization of the Impact Strengths of Vapor-Grown Carbon Nanofiber/Vinyl Ester Nanocomposites Using a Central Composite Design," Submitted to *Journal of Applied Polymer Science* (Under Review).
8. Yu, J., Lacy, T.E., Toghiani, H., and Pittman Jr., C.U., 2011, "Effective Thermal Conductivity Estimates for Nanocomposites Containing Multiple Nanoheterogeneities," Submitted to *Composites: Part B* (Under Review).

Conference Papers and Manuscripts in Preparation

1. Ricks, T.M., Lacy, T.E., Bednarcyk, B.A., and Arnold, S.M., "A Multiscale Modeling Methodology for Metal Matrix Composites Including Fiber Strength Stochastics," in the *Proceedings of the 53rd AIAA/ASME/ASCE/AHS/ASC Structures, Structural Dynamics, and Materials Conference*, Honolulu, Hawaii, April 23-26, 2012.
2. Jang C., Lacy, T.E., Gwaltney, S.R., Toghiani, H., and Pittman, Jr., C.U., "Molecular Dynamics Simulation of Vinyl Ester Resin Crosslinking," in the *Proceedings of the 53rd AIAA/ASME/ASCE/AHS/ASC Structures, Structural Dynamics, and Materials Conference*, Honolulu, Hawaii, April 23-26, 2012.
3. Yu, J., Lacy, T.E., Toghiani, H., and PittmanJr., C.U. "Micromechanically Based Effective Thermal Conductivity Estimates for Polymer Nanocomposites," in the *Proceedings of the 53rd AIAA/ASME/ASCE/AHS/ASC Structures, Structural Dynamics, and Materials Conference*, Honolulu, Hawaii, April 23-26, 2012.
4. Yu, J., Lacy, T., Toghiani, H., and Pittman Jr., C.U., "Micromechanically Based Effective Thermal and Electrical Properties Estimates for Polymer Nanocomposites," to appear in the *Proceedings of the American Society for Composites 27th Annual Technical Conference*, Arlington, Texas, October 1-3, 2012.
5. McWilliams, J.K., Ricks, T.M., Nall, J.N., Favaloro, A.J., Nouranian, S., Lacy, T.E., Toghiani, H., Pittman, Jr., C.U. "Flexural Response of Vapor Grown Carbon Nanofiber Enhanced Woven Fabric Composites," to appear in the *Proceedings of the American Society for Composites 27th Annual Technical Conference*, Arlington, Texas, October 1-3, 2012.
6. Nall, J.N., Ricks, T.M., Nouranian, S., Pittman, Jr., C.U., Zhang, Y., Lacy, T.E., Toghiani, H. "Vinyl Ester Reinforced with Oxidized Vapor-Grown Carbon Nanofibers Modified with a Methacrylate-based Coupling Agent," to appear in the *Proceedings of the American Society for Composites 27th Annual Technical Conference*, Arlington, Texas, October 1-3, 2012.
7. Lee, J., Nouranian, S., Torres, G.W., Lacy, T.E., Toghiani, H., Pittman, Jr., C.U., DuBien, J.L. "Flexural Properties of Vapor-Grown Carbon Nanofiber/Vinyl Ester Nanocomposites," To be submitted to *Journal of Applied Polymer Science* (Tentative submission date April 2012).
8. Yu, J., Lacy, T.E., Toghiani, H., and Pittman Jr., C.U. "Effective Electrical Conductivity Estimates for Nanocomposites Containing Multiple Nanoheterogeneities," To be submitted to *Mechanics of Materials* (Tentative submission date April 2012).
9. Hutchins, J.W., Sisti, J., Ricks, T.M., Nouranian, S., Lacy, T.E., Pittman, Jr., C.U., Toghiani, H. "Strain Rate Sensitivity of the Compressive Response of Carbon Nanofiber Reinforced Vinyl Ester," To be submitted to *Mechanics of Time-Dependent Materials* (Tentative submission date May 2012).
10. Yu, J., and Lacy, T.E., "Micromechanically Based Constitutive Models for the Nonlinear Viscoplastic Behavior of Polymer Nanocomposites," To be submitted to *Mechanics of Materials* (Tentative submission date June 2012).
11. Yu, J., and Lacy, T.E., "Micromechanically Based Constitutive Models for the Nonlinear Elastoplastic Behavior of Metal Matrix Composites," To be submitted to *Mechanics of Materials* (Tentative submission date July 2012).

ACTIONS PLANNED FOR THE NEXT QUARTER

1. Continue multiscale modeling development activities:
   - Continue molecular dynamics simulation activities for initiate the MD simulations for carbon nanofiber pull-out from the crosslinked VE matrix.
   - Determine micromechanically-based effective mechanical, thermal, and electrical properties for multi-phase nanocomposites containing different types of nanoreinforcements (nanofibers, nanoclay platelets, etc.) using EC-MAC.
   - Develop a nanocomposite strength estimation module within EC-MAC based upon Bowyer-Bader model.
   - Investigate the effect of inelastic matrix material behavior and fiber-matrix interphase on effective properties using the differential Self-Consistent method.
   - Develop a non-linear material modeling using EC-MAC for elastoplastic and viscoplastic materials.
2. Continue hybrid composite fabrication using VARTM:
   - Perform SEM imaging of hybrid composites to assess the degree of VGCNF filtering.
   - Conduct three-point bend tests of E-glass/VE and E-glass/VGCNF/VE flexural specimens in accordance with ASTM D7264.

SUBTASK 3.3: BIODEGRADABLE COMPOSITES

No report this quarter

SUBTASK 3.4: BIOMATERIALS

Team Members: L. Williams, *J. Liao, H. Rhee, Y. Mao, S. Patnaik (Ph.D student), M. Rougeau (M.S. student), N. Y. Lee (Ph.D. student)*

SUMMARY OF THE PROGRESS

The objectives were met by accomplishing the following:

1. Created the finite element mesh of patellar ligament;
2. Obtained compressive properties of fresh porcine lung tissues;
3. Carried out materials/mechanical properties tests of the woodpecker beak using transmission electron microscopy and compression test;
4. Carried out materials and mechanical properties tests and investigated structure-property relations of bream teeth using x-ray computed tomography, EDX and nano-indentation.

Developing a Model of the Ligament/Tendon

The finite element mesh of patellar ligament were developed from high resolution cryosection images obtained from the National Library of Medicine's Visible Human Project [1]. The cryosection images were resampled to 1 mm/pixel at 1 mm intervals. Using an image processing software (ScanIP, Simpleware, Ltd), the patellar ligament and bones were segmented with a combination of semi-automated and manual segmentation operations (threshold, flood fill, region growing, etc.) After the segmentation, realistic, high quality volumetric finite element mesh for patellar ligament (Figure 1) was generated using an image based meshing software (ScanFE, Simpleware, Ltd). The meshes contained hybrid volume elements including hexahedral elements within each part and tetrahedral elements on the surface to provide smooth along the boundaries.

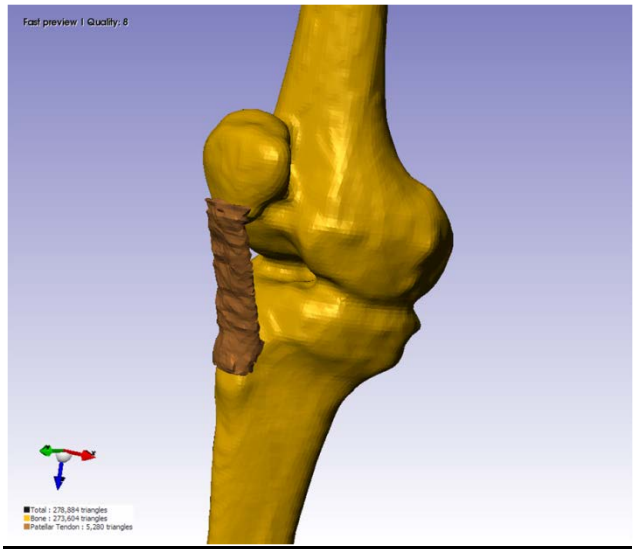

Figure 1. Finite element mesh of patellar ligament and bones.

Reference
1. Ackerman, M.J., The Visible Human Project. Proceedings of the IEEE, 1998. 86(3): p. 504-511.

Lung Literature Review and Mechanical Test Data

Introduction

Blast injuries are classified as primary (blast overpressure), secondary (flying objects), tertiary (body flying in air and hitting other objects due to explosion) and quaternary (all other injuries) (Mayorga 1997; Champion 2009; Wolf 2009). Primary blast injuries affect the air filled structures like the gastrointestinal tract, ears and lungs. Damage to these air filled structures due to blast over pressure or by a blast wave can be severe. Lung is the 2nd most affected organ in primary blast injuries (tympanic membrane being the most severe) (Choung 1985; Mayorga 1997). Although research on blast mechanisms have been performed for close to a century, it was only in the late 80's when the blast injury mechanics was formulated (Phillips III 1991). Choung et.al. conducted experimental studies on lungs and other soft tissues in the thoracic cavity, to understand the injuries caused due to blast (Choung 1985). He concluded that during propagation of a pressure wave, chest wall and ribs acts as barriers and cause additional damage to the thoracic region. Pleural surface (thin membrane covering the lung) is the first to be damaged and additional "rib markings" are produced by the impact of waves on the lungs. Various computational studies on the blast simulations and experimental studies on lung tissue have been performed, but the material was taken as homogenous without considering the effects of blood vessels, surface tension due to surfactants, airtubes and pleural membrane (which is not accurate) (Lee 1976; Vawter 1980; Rodarte 1982; Ligas 1984; Choung 1985; Ligas 1985; Stuhmiller 1988; Stuhmiller 1996; Stuhmiller 1997; Gao 2006). Thus, a detailed microstructural structure-property relationship study of the lungs tissue is needed which will be a useful input for future computational models and also for better representation of its mechanical responses.

Structure of Lungs

The structure of lungs is very complex. Although the structural details of lungs can be traced back to centuries, it is only after the electron microscopic studies in 1950's that led to the establishment of its microstructure. Lungs always occur in pairs in human and most mammals – left lungs and right lungs (Fig 1 (a)). Further the lungs are divided into compartments called lobes; left lung has three lobes and a right lung has two lobes. The distinct separation of lungs into lobes is by the presence of septa (a thick fibrous tissue). Lungs consist of stiff network of tubes embedded in porous soft tissue (lungs parenchyma). The soft tissue or the lungs parenchyma is made up of smooth muscle cells and various elastic fibers. A thin layered membrane called pleural membrane cover the lungs tissue and it is filled with pleural fluid. The trachea descends down to thoracic cavity and divides to unequal parts and tubes vary in shape and size (in order: bronchi – lobar bronchi - segmental - sub segmental bronchi – small bronchi – bronchioles – respiratory bronchioles), which further gives splits into alveolar ducts and ultimately alveoli (air sacs for gaseous exchange) (Fig 1 (b)).

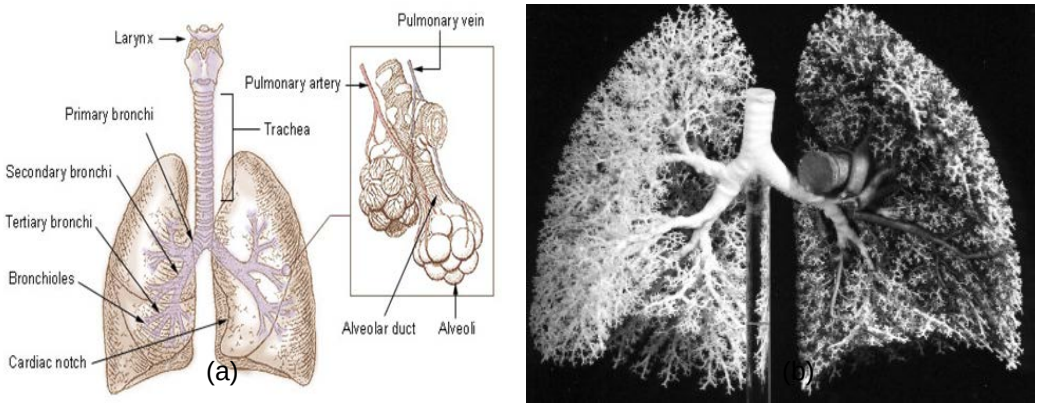

(Source: http://images-mediawikisites.thefullwiki.org/04/2/2/3/8149260198858287.jpg)

Figure 1. (a) Structure of lungs. (b) Airway structure of the entire lungs (distribution of tubes) (Adapted from Shields et.al (Shields 2000))

A thin film of liquid lines the alveoli and exerts surface tension. But this surface tension is countered by presence of surfactant in the lungs, of 0.15µm thickness, which ultimately allows the lungs to be stretched. Walls of airways are composed of cartilage which helps maintain their shape during breathing. They also contain smooth muscle cells but they don't have much role. On an average 23 branchings occur between trachea and alveoli, but variations do exist. Alveoli are the sites of gaseous exchange and are located in the alveolar ducts and respiratory bronchioles. These are composed of type I and type II epithelial cells. About 300 millions alveoli exist, the diameter of each alveolus varies from 0.1 to 0.3 mm and alveolar surface area may be 30-100 m^2. Alveoli and the septa make up majority of the lung parenchyma (i.e. bulk of the lung tissue).

Material Property of Lung Tissue (Lung Parenchyma)

Lung parenchyma is often described as randomly oriented, viscoelastic and pre-stressed compressible material which exhibits non linear stress-strain behavior (Lambert 1973; Lai-Fook 1977; Rodarte 1982; Ligas 1984; Ligas 1985; Gao 2006; Suki 2011). Most of the mechanical energy spent during inflation and thus is recovered in deflation & rest is dispensed throughout the structure (fluid and airtubes). Not only the components of the lung tissue (i.e. elastin and collagen) (Faffe 2006), but also its natural architecture is responsible for the mechanical properties (Mead 1961). Collagen fibers in the parenchyma form an axial network and extend from the pleura. At lower strains load bearing work is taken by elastin. On the other hand collagen fibers bear the load at higher strain rate and become stiffer (Mead 1961; Suki 2011). Tension forces cause of majority of the damage in the lung tissue rather the compressive forces, during blast wave propagation (Stuhmiller 1988; Stuhmiller 1996; Stuhmiller 1997; D'Yachenko 2006). Additionally, decompression of the lungs even for a short duration causes considerable damage to lungs tissue. In comparison to compressive forces, shear forces are less sensitive to increasing physiological pressure (i.e. shear modulus is insensitive to pressure changes) and thus play lesser role in lung damage (Stamenovic 1986). Overall, compression forces play vital role in primary blast injury and investigation of lungs tissue in compressive mode was selected for this study. Future studies will address the detail analysis of lungs tissue from different anatomical locations.

Mechanical Tests

Blast pressure wave creates a direct stress wave and accompanying transmitted wave which applies direct compression force of the thoracic cavity and ultimately the lungs (Stuhmiller 1988; Cooper 1991; Stuhmiller 1996; Stuhmiller 1997). Major issue with mechanical testing of lung :*in vivo* – filled with air ; *in vitro* – no air (J. W. Melvin 1974). Direct measurement of mechanical properties of excised lung parechanymal tissue can be done by performing uniaxial or biaxial tests in a water bath. Many authors support to the fact that *in vitro* mechanical test of excised lung tissue is almost an ideal representation of the *in vivo* tissue (Fust 2004; Gao 2006). Although gas pressure is not significant enough to apply any direct force on internal structure, there is some degree of deformation which leads to changes in stress (i.e. during the breathing cycle). Recent studies have shown that preconditioning and a mechanical test of lung tissue conducted in water bath (saline solution) does not require special rinsing and degassing procedures (Leite-Junior 2003). Vawter and co-workers reported that lung parenchyma was elastic is compression in higher strains as compared to tension (Vawter 1978). Within physiological limits, increasing surface tension increases the bulk modulus of the lung parenchyma and decreases above the physiological range (Stamenovic 1986).

Experimental Methods

The objective of this study was to quantify the compressive mechanical properties of fresh porcine lungs tissue (i.e. to study the viscoelastic mechanical response of the tissue). Directional dependence of the tissue was tested by resecting tissue samples from coronal, sagittal and transverse planes (Fig. 2). All tests were performed in a BSL2 certified laboratory at MSU Ag and Bio Eng Facility. Samples were obtained fresh from the local abattoir (Sansing Meat Service, MS). Tests were performed within 4-5 hours to remove any unfavorable effect of tissue degradation. Excess tissues attached to the lungs were removed. All tests were done using Mach 1 Micromechanical Testing System® (Biomomentum, Quebec, Canada) and in water bath as shown in Fig.2.

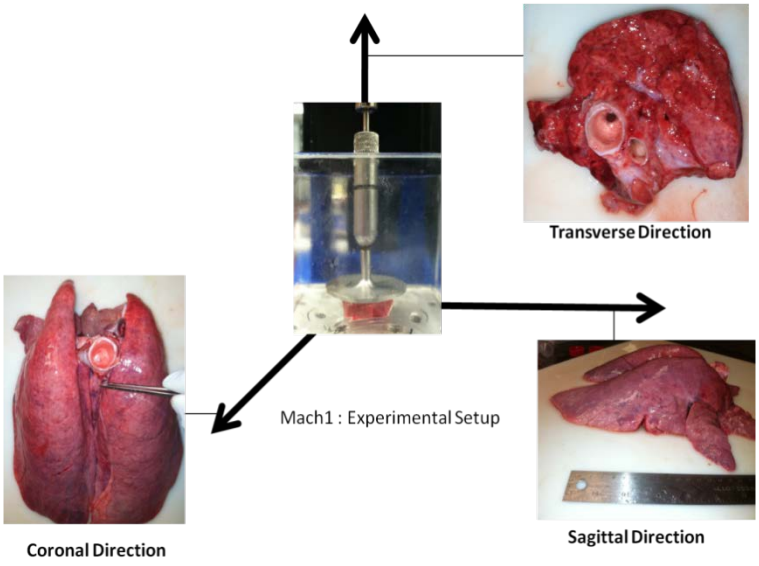

Figure 2. Mechanical testing setup and direction of testing.

Using scalpel blades, samples were cut in disc shape of aspect ratio of 20 mm:10 mm (diameter to thickness) (Fig. 3).

Compression Test

Sample for fresh porcine lung tissue sample was cut in a disc shape (Fig.3).

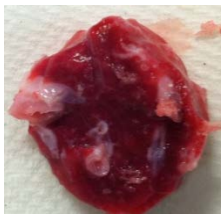

Figure 3. Disc shaped porcine lung tissue samples. Diameter to thickness-20 mm: 10mm

A flat disc shaped metal clamp was used for this test. The sample was glued at the bottom and top to avoid any tension created due to unloading of sample. Sample thickness was again measured using the "find contact" mechanism in the Mach1 Micromechanical Mach1 Micromechanical Testing System® (Biomomentum, Quebec, Canada) and the loading velocity was calculated accordingly.

$$\textit{Loading velocity} = \textit{Strain rate X Thickness (For compression only)}$$

Samples were submerged in Phosphate buffer saline (PBS) solution to simulate physiological conditions and prevent samples from drying during the test. Samples were pre-loaded at 2gm, pre-conditioned at 0.1/sec strain (10 times), compressed to 60% of load cell (at the constant rate of 0.1 /sec) and then unloaded.

Table 1. Test matrix. No. of test performed.

Tissue Type \Direction	Frontal	Sagittal	Transverse
Load	18	14	15
Unload	18	14	15
Strain Rate	0.1/s	0.1/s	0.1/s

Samples were collected from all three directions to study the directional dependent nature of porcine lungs tissue (Details represented in Table.1).

Results

The ultimate compressive stress on wet tissues during loading was in the range of 35,000-50,000 Pa. The ultimate compressive stress on the tissues during unloading was in the range of 30,000-40,000 Pa. The averaged loading and unloading results for the three orthogonal directions are shown below in Figures 4(a)-4(i).

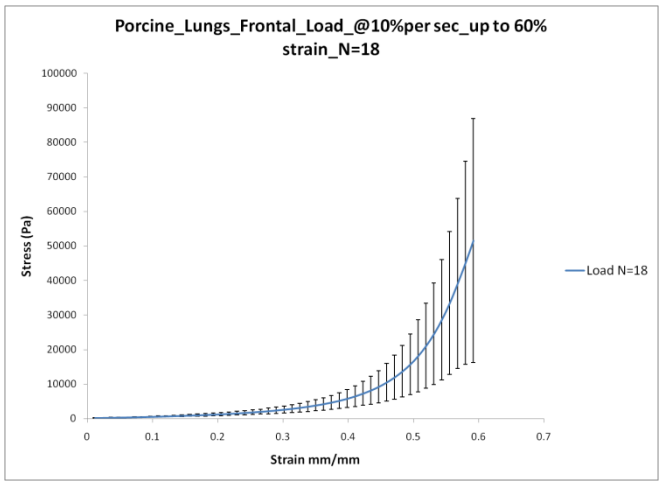

(a)

Figure 4 (a). Load Stress- Strain curve of fresh porcine lungs tissue in Frontal Direction compressed at the rate of 0.1 per sec up to 60% strain.

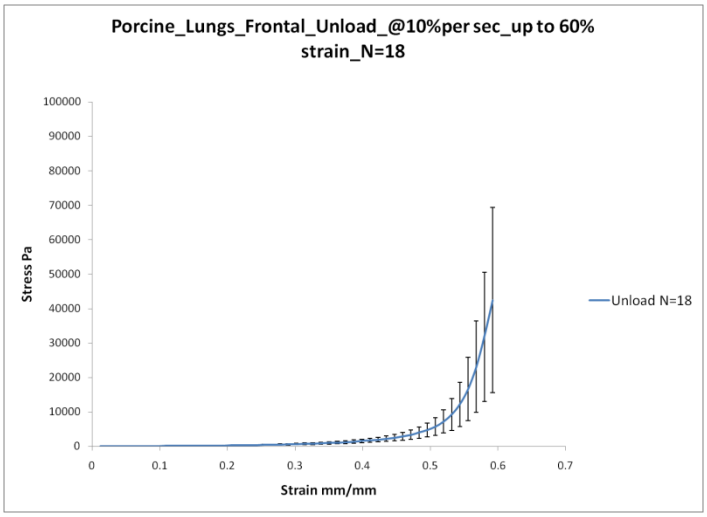

(b)

Figure 4 (b). Unload Stress- Strain curve of fresh porcine lungs tissue in Frontal Direction compressed at the rate of 0.1 per sec up to 60% strain.

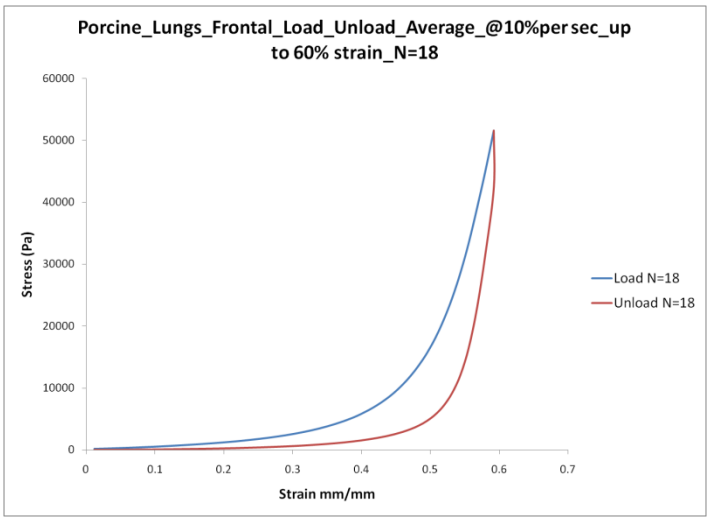

(c)

Figure 4 (c). Load Unload Average Stress- Strain curve of fresh porcine lungs tissue in Frontal Direction compressed at the rate of 0.1 per sec up to 60% strain.

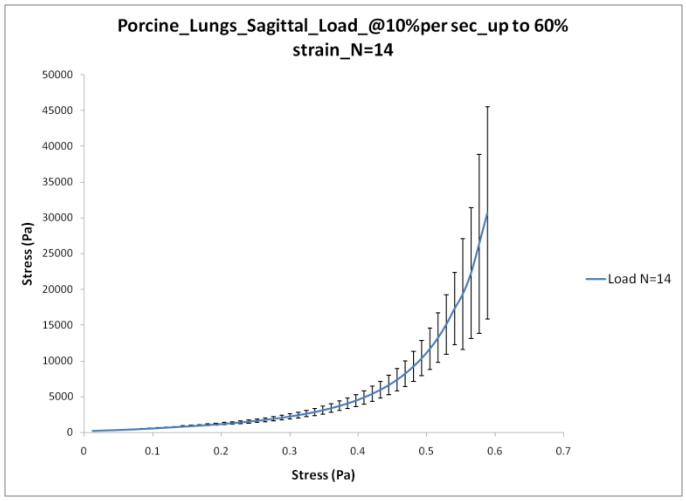

(d)

Figure 4 (d). Load Stress- Strain curve of fresh porcine lungs tissue in Sagittal Direction compressed at the rate of 0.1 per sec up to 60% strain.

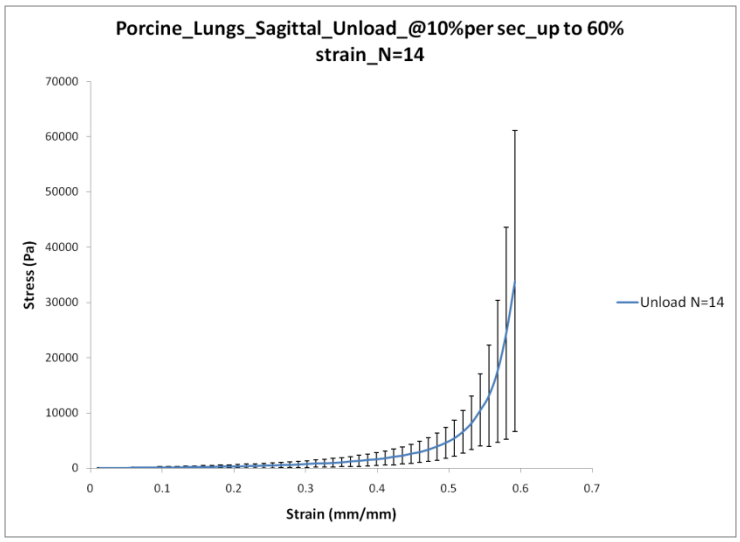

(e)

Figure 4 (e). Unload Stress-Strain curve of fresh porcine lungs tissue in Sagittal Direction compressed at the rate of 0.1 per sec up to 60% strain.

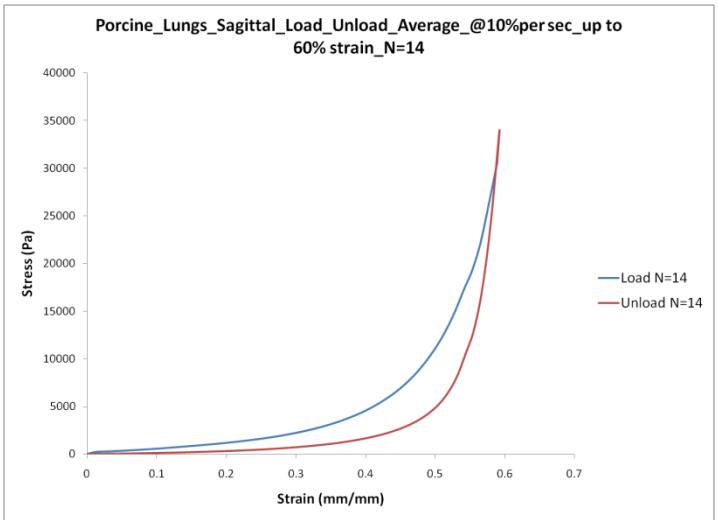

(f)

Figure 4 (f). Load Unload Average Stress-Strain curve of fresh porcine lung tissue in Sagittal Direction compressed at the rate of 0.1 per sec up to 60% strain.

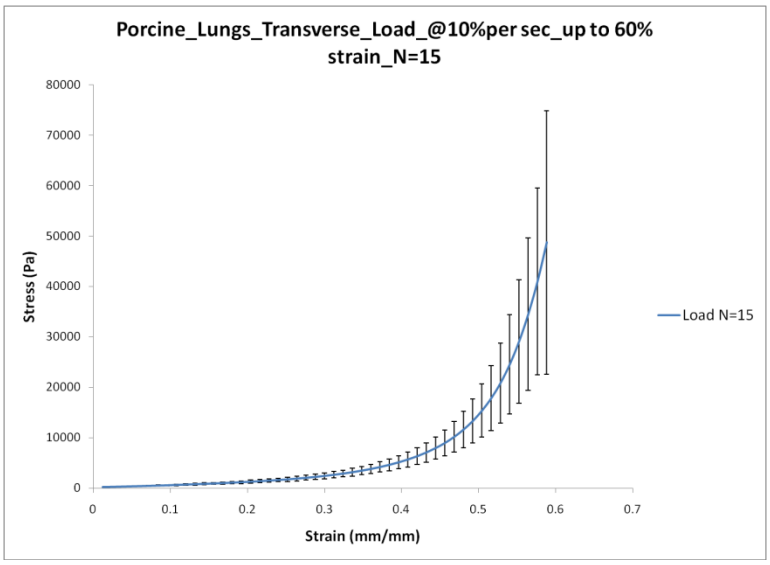

(g)

Figure 4 (g). Unload Stress-Strain curve of fresh porcine lungs tissue in Transverse Direction compressed at the rate of 0.1 per sec up to 60% strain.

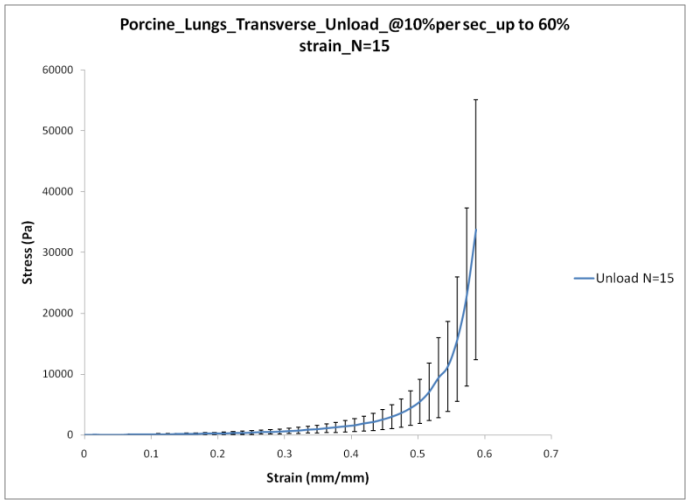

(h)

Figure 4 (h). Load Stress-Strain curve of fresh porcine lungs tissue in Transverse Direction compressed at the rate of 0.1 per sec up to 60% strain.

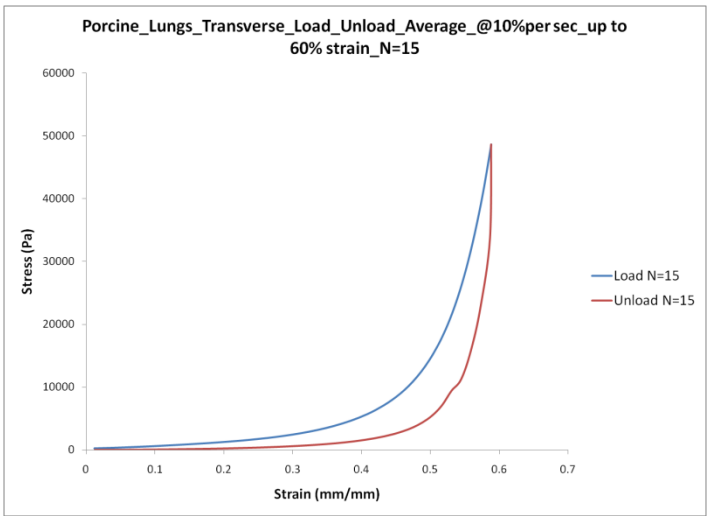

(i)

Figure 4 (i). Unload Stress- Strain curve of fresh porcine lungs tissue in Transverse Direction compressed at the rate of 0.1 per sec up to 60% strain.

References

Champion, H. R., Holcomb, J. B., Young, L. A. (2009). "Injuries from explosions: physics, biophysics, pathology, and required research focus." *The Journal of Trauma***66**(5): 1468-1477; discussion 1477.

Choung, C. J. (1985). Chacterization and Modeling of Thoraco - Abdominal Response to Blast Waves. *Biomechanical Model of Lung Injury Mechanisms*, San Deigo, CA. **6**.

Cooper, G. J., Townend, D. J., Cater, S. R., Pearce, B. P. (1991). "The role of stress waves in thoracic visceral injury from blast loading: modification of stress transmission by foams and high-density materials." *Journal of Biomechanics* **24**(5): 273-285.

D'Yachenko, A. I., Manyuhina, O. V. (2006). "Modeling of weak blast wave propagation in the lung." *Journal of Biomechanics* **39**(11): 2113-2122.

Faffe, D. S., D'Alessandro, Elizabeth S., Xisto, Debora G., Antunes, Mariana A., Romero, Pablo V., Negri, Elnara M., Rodrigues, Nilza R. D., Capelozzi, Vera L., Zin, Walter A., Rocco, Patricia R. M. (2006). "Mouse strain dependence of lung tissue mechanics: Role of specific extracellular matrix composition." *Respiratory Physiology & Neurobiology* **152**(2): 186-196.

Fust, A., Bates, J. H. T., Ludwig, M. S. (2004). "Mechanical properties of mouse distal lung: in vivo versus in vitro comparison." *Respiratory Physiology & Neurobiology* **143**(1): 77-86.

Gao, J., Huang, W., Yen, R. T. (2006). "Mechanical properties of human lung parenchyma." *Biomedical Sciences Instrumentation* **42**: 172-180.

J. W. Melvin, A. S. W. (1974). Thoracic Model Improvements (Experimental Tissue Properties) Vol 2. , Highway Safety Research Institute, Univeristy of Michigan.

Lai-Fook, S. J. (1977). "Lung parenchyma described as a prestressed compressible material." *Journal of Biomechanics* **10**(5-6): 357-365.

Lambert, R. K., Wilson, T. A. (1973). "A model for the elastic properties of the lung and their effect of expiratory flow." *Journal of Applied Physiology* **34**(1): 34-48.

Lee, G. C., Frankus, A., Chen, P. D. (1976). "Small distortion properties of lung parenchyma as a compressible continuum." *Journal of Biomechanics* **9**(10): 641-648.

Leite-Junior, J. H., Rocco, P. R., Faffe, D. S., Romero, P. V., Zin, W. A. (2003). "On the preparation of lung strip for tissue mechanics measurement." *Respiratory Physiology & Neurobiology* **134**(3): 255-262.

Ligas, J. R. (1984). "A non-linearly elastic, finite deformation analysis applicable to the static mechanics of excised lungs." *Journal of Biomechanics* **17**(8): 549-552.

Ligas, J. R., Saidel, G. M., Primiano, F. P., Jr. (1985). "Parameter estimation and sensitivity analysis of a nonlinearly elastic static lung model." *Journal of Biomechanical Engineering* **107**(4): 315-320.
Mayorga, M. A. (1997). "The pathology of primary blast overpressure injury." *Toxicology* **121**(1): 17-28.
Mead, J. (1961). "Mechanical Properties of Lungs." *Physiological Reviews* **41**(2): 281-330.
Phillips III, Y. Y., Richmond, D. R. (1991). Primary Blast Injury and Basic Research : Brief History, Department of Pulmonary and Critical Care Medicine Services, Walter Reed Army Medical Center, Washington, D.C**:** 221-241.
Rodarte, J. R. (1982). "Stress-strain analysis and the lung." *Federation Proceedings* **41**(1): 130-135.
Shields, T. W., LoCicero, J., Ponn, R. B., (2000). *General Thoracic Surgery*. Philadelphia, Lippincott Williams & Wilkins.
Stamenovic, D., Smith, J. C. (1986). "Surface forces in lungs. III. Alveolar surface tension and elastic properties of lung parenchyma." *Journal of Applied Physiology* **60**(4): 1358-1362.
Stuhmiller, J. H. (1997). "Biological response to blast overpressure: a summary of modeling." *Toxicology* **121**(1): 91-103.
Stuhmiller, J. H., Chuong, C. J., Phillips, Y. Y., Dodd, K. T. (1988). "Computer modeling of thoracic response to blast." *The Journal of Trauma* **28**(1 Suppl): S132-139.
Stuhmiller, J. H., Ho, K. H., Vander Vorst, M. J., Dodd, K. T., Fitzpatrick, T., Mayorga, M. (1996). "A model of blast overpressure injury to the lung." *Journal of Biomechanics***29**(2): 227-234.
Suki, B., Bates, Jason H. T. (2011). "Lung tissue mechanics as an emergent phenomenon." *Journal of Applied Physiology* **110**(4): 1111-1118.
Vawter, D. L. (1980). "A finite element model for macroscopic deformation of the lung." *Journal of Biomechanical Engineering* **102**(1): 1-7.
Vawter, D. L., Fung, Y. C., West, J. B. (1978). "Elasticity of excised dog lung parenchyma." *Journal of Applied Physiology* **45**(2): 261-269.
Wolf, S. J., Bebarta, Vikhyat S., Bonnett, Carl J., Pons, Peter T., Cantrill, Stephen V., (2009). "Blast injuries." *The Lancet* **374**(9687): 405-415.

Materials/Mechanical Properties Tests and Structure-Property Relations of the Woodpecker Hyoid Bone

Introduction

The avian beak is a structural biocomposite material. Generally, biological materials for a structure comprise brittle mineral and ductile protein components in complex structure, which are hierarchically organized, function-oriented suitable, and energy-efficient design [1, 2].

Bird's beaks composed of bone and a β-keratin sheath which covers bone and is called rhamphotheca[3, 4]. Between bone and a β-keratin, there is dermis within several mechanoreceptors to sense vibration and mechanic force, and these receptors locates in the beak bone as well [5, 6]. Since the work of Seki et al. [7-10], the nanostructure of the birds beak-toucans and hornbills- were elucidated. At nanoscale level, keratin scales are constituted of β–keratin filaments which have running direction, and there is a space between keratin scales in toucans and hornbills[8].

For the mechanical responses the tensile Young's modulus of rhamphotehca is ~1 GPa at toucans and hornbills. Compressive behavior of beaks largely depends on Young's modulus of bone and densification is occurred at 90% strain.

In here, particularly we examined the beaks of woodpeckers because woodpeckers show amazingly efficient shock absorption without any recorded damage to their beaks or brains while pecking trees. Since birds use light weight material for flying, this biological material can provide the inspiration for new, innovative material developments. From the motivation of studying woodpeckers' beaks, we are learning clues in solving human engineering problems related to the energy absorption and shock mitigation. In order to presents multiscale structure-properties relationship of the woodpecker beak, in this quarter, we examined nanostructure and macromechanical properties.

Experimental Approach

The beaks of the adult Red-bellied Woodpecker *Melanerpes carolinus* were studied by using transmission electron microscopy (TEM) and mechanical testing. The Red-bellied Woodpecker is a medium sized bird living in Southern United States, and it pecks trees for making a hole as a nest or seeking insects. Non-living woodpeckers were obtained from the collections of the Department of Wildlife, Fisheries and Aquaculture (Mississippi State University), and upper and lower beaks were separated from the body of woodpecker. The full length of the beak is about 4 cm, and samples for testing were dried, and the tests were carried out at room temperature and a humidity of approximately 70%.

In order to characterize the nanostructural, transmission electron microscopy (TEM) was used. Beak samples for TEM were fixed in 2.5% glutaraldehyde and post fixed in 2% osmium tetraoxide. Samples were then rinsed, dehydrated in a graded ethanol series. Fixed samples embedded in Spurr's resin, and ultra-thin sections (60-80 nm) were cut on a Reichert-Jung Ultra cut E ultramicrotome and were stained with uranyl acetate and lead citrate. Stained sections were examined by using a JEOL JEM-100CX II Transmission Electron Microscope at an acceleration voltage of 80 kV. Mechanical experiments were carried out via compression test. For compression test specimen, only the middle part of the beak was available because very tip of the beak has a shape of cone, so it could not stand on an anvil. The lower beak was cut into three parts with a height of 5 mm by using a diamond saw. For the cross-section area, the mean value of the top and bottom area was used for analysis. The test was carried out using Instron EM Model 5869 with 50kN load cell. Displacement was measured with an extensometer attached to the crosshead. The crosshead speed was 0.06 m/min.

Experimental Results

Fig. 1 shows the images of the transverse and longitudinal view of the rhamphotheca of the woodpecker beak garnered from a Transmission Electron Microscopy (TEM). The samples were taken from the tip part of the beak, and the cross-sectional view revealed that keratin scales are packed tightly at this level (Fig. 1(a)). At the middle part of beak, keratin scales are arranged side by side; however, at the tip part, they are closely packed relatively. Consequently, they have more of a round and cell-like shape instead an elongated shape. The size of the cell-shaped structures varies from 10 to 15 μm of a diameter. By zooming in the cell boundary, Fig. 1(b) revealed that the cell boundary is a wavy structure. The waviness (h / λ) was calculated from each period of wave and analyzed, and the mean waviness is 1.024 ± 0.322. In Fig. 1(c), it is observable that there is a narrow gap along the wavy line, which distance is 44.2 ± 19.2 nm. Figs. 1(d)-(f) depict the longitudinal view of the rhamphotheca at the same spot. In Fig. 1(d), we can see the side view of the keratin scales, and Fig. 1(e) is the boundary where two keratin

scales contact. It shows that the fiber of β-keratin has a direction running in parallel to the transverse orientation. Enlarging the contact point of two scales, Fig. 1(f) also shows the gap in the wavy line.

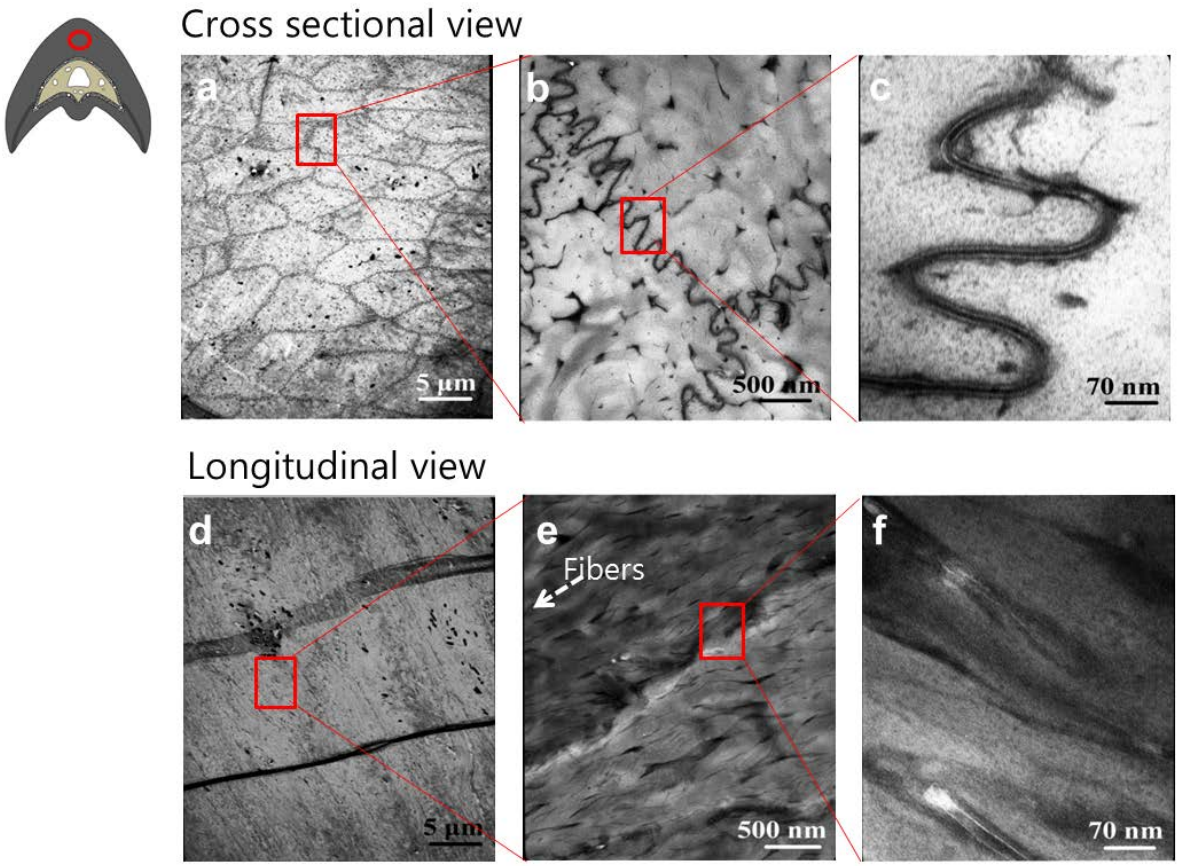

Figure 1. Nanostructure of the rhamphotheca of the woodpecker beak taken by a Transmission Electronic Microscope: (a) cross-sectional view revealing the keratin cells in the rhamphotheca; (b) cross-sectional view that shows the wavy lines at the cell boundary; (c) cross-sectional view that depicts a small gap in the wavy line; (d) a longitudinal view in the rhamphotheca; (e) a longitudinal view with the arrows indicating the running direction of the fiber; and (f) a longitudinal view showing the wavy line and gap.

Fig. 2 shows the nanostructure of the bony layer. As shown in Fig. 2(a), the bone layer has cells which have a round shape, and fibers are distributed. Fig. 2(b) illustrates that the direction of the fibers is not uniform unlike the β-keratin in the rhamphotheca. We can see the both direction of the longitudinal (L) and the cross-sectional (C) view of the fibril, and the different running direction at the longitudinal way as it indicated 'L1' and 'L2' as well. Fig. 2(c) shows the D period which is the apparent indication that the kind of fibril is the collagen. Fecchio et al. [7] suggested the foam part of the toucan beak is mineralized collagen or bone since the analysis of the amino acid composition shows this part is Glycine rich. Our nanostructure results support their suggestion strongly. Because the foam part of the toucan and the bony layer of the woodpecker is the similar or the same material, it also supports the claim that the material composing the foam layer is continuous from the material of the bony layer in a woodpecker's beak.

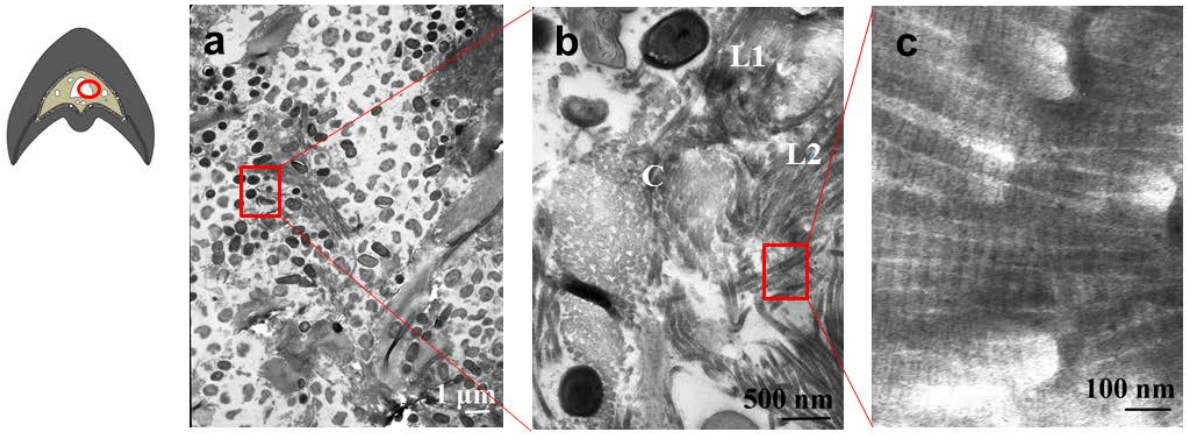

Figure 2. Nanostructure of the bony layer of the woodpecker beak taken by a Transmission Electronic Microscope: (a) it is illustrated that the distribution of the bone cells that have round shapes and short fibrils(grey); (b) the fibrils are running in both of the longitudinal (L) and cross-sectional (C) direction, also, at the longitudinal way, the fibrils have different running direction as indicated L1 and L2. The running direction of the fibrils is not uniform; and (c) the fibers have a D-period which refers that the fibrils are the collagen.

Compression tests were carried out on the three different location of the woodpecker beak; back(sample No.1), middle near back(sample No.2), and middle near tip(sample No.3). At the result of the compression test, the elastic modulus and the compressive yield strength are significantly different at the three locations. Each section has different Young's modulus such as back part of the beak has 7.923 GPa, the middle part has 3.676 GPa, and the tip part has 2.097 GPa, and different compressive yield strength at each sample as well. The graph in Fig. 3 describes the bumpy plateau at the samples of

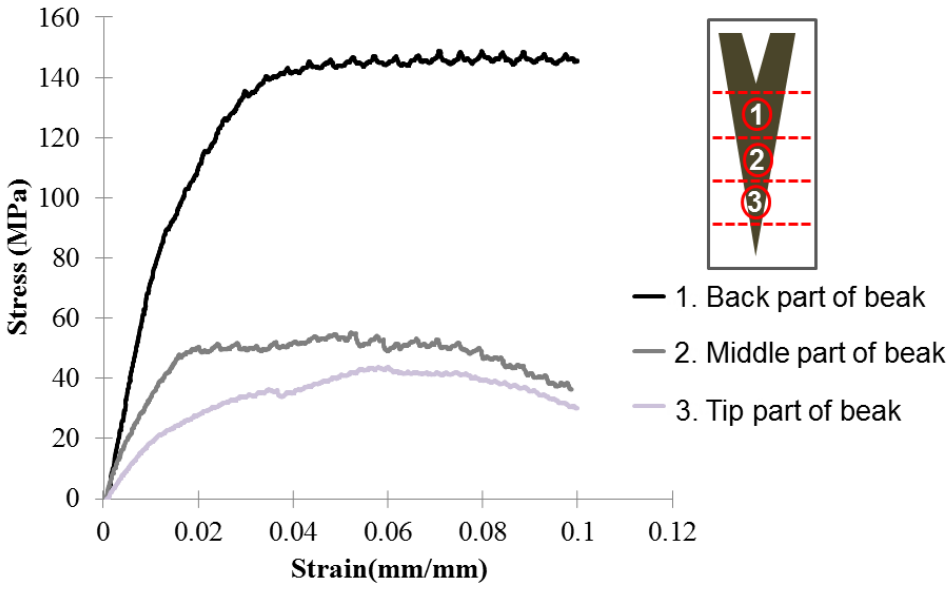

Figure 3. The stress-strain graph showing the results from the compression test on the woodpecker beak. The diagram shows that the elastic modulus of each part has different according to the location, which has different proportion of the rhamphotheca and bony layer.

1 and 2 in the graph, and it was occurred due to the buckling of the strut in bony layer during compression.

Discussion and Conclusions

In this study, we examined the structure and mechanical properties of beaks of Red-bellied Woodpecker, *Melanerpes Carolinus*. The woodpecker beak is structural biocomposite having three layers; rhamphotheca (exterior shell keratin), middle foam layer, and interior bony layer. Along the beak from posterior to interior, the area fraction of these layers is changed gradually, so the result of the compression tests shows the each different Young's modulus and compressive yield strength. At the result of the compression test, the elastic modulus and the compressive yield strength are not equal at the three locations; back, middle near back, and middle near tip. This is because each sample has different area fraction of the keratin and the bony material. According to the rule of mixture, which is developed for composite material and can be applied for explaining the layered material, we can explain the different stress with area fraction and strength at each sample (Eq. (1)).

$$(\sigma A)_{total} = (\sigma A)_{rhamphoteca} + (\sigma A)_{bony} \quad (1)$$

where 'A' represents the area and 'σ' represents stress.

From the TEM images, the geometry of the wavy line shown at the keratin cell boundary is similar to a suture line, which has a role of energy absorption in cranial bone [11]. Suture morphology relates to the load, especially compressive loads, and arrangement of the fibers in the suture [12]. Thus, this wavy line is also assumed to have the energy absorption role at the tip of the woodpecker beak. Bony layer has a structure analogous to synthetic fiber-resin system. This is efficient structure for load bearing with light weight.

References

1. Meyers, M.A., et al., *Structural biological composites: an overview.* JOM Journal of the Minerals, Metals and Materials Society, 2006. **58**(7): p. 35-41.
2. Sanchez, C., H. Arribart, and M.M.G. Guille, *Biomimetism and bioinspiration as tools for the design of innovative materials and systems.* Nature Materials, 2005. **4**(4): p. 277-288.
3. Bonser, R.H.C., *The mechanical properties of feather keratin.* Journal of Zoology, 1996. **239**(3): p. 477-484.
4. Shames, R.B., et al., *Keratinization of the outer surface of the avian scutate scale: Interrelationship of alpha and beta keratin filaments in a cornifying tissue.* Cell and tissue research, 1989. **257**(1): p. 85-92.
5. Stettenheim, P.R., *The integumentary morphology of modern birds—An overview.* American Zoologist, 2000. **40**(4): p. 461-477.
6. Gentle, M.J. and J. Breward, *The bill tip organ of the chicken (Gallus gallus var. domesticus).* Journal of anatomy, 1986. **145**: p. 79.
7. Fecchio, R., et al., *Mechanical behavior of prosthesis in Toucan beak (Ramphastos toco).* Materials Science and Engineering: C, 2010. **30**(3): p. 460-464.
8. Seki, Y., S.G. Bodde, and M.A. Meyers, *Toucan and hornbill beaks: A comparative study.* Acta Biomaterialia, 2010. **6**(2): p. 331-343.

9. Seki, Y., et al., *The toucan beak: structure and mechanical response.* Materials Science and Engineering: C, 2006. **26**(8): p. 1412-1420.
10. Seki, Y., M.S. Schneider, and M.A. Meyers, *Structure and mechanical behavior of a toucan beak.* Acta materialia, 2005. **53**(20): p. 5281-5296.
11. Jaslow, C.R., *Mechanical propertise of cranial sutures.* J Biomechanics, 1990. **23**(4): p. 313-321.
12. Krauss, S., et al., *Mechanical Function of a Complex Three Dimensional Suture Joining the Bony Elements in the Shell of the Red Eared Slider Turtle.* Advanced Materials, 2009. **21**(4): p. 407-412.

Structure-Property Relations of Bream Teeth

Introduction

Structures and mechanical properties of human teeth [1-5] and various fish teeth [6-8] were reported in the literature. These studies provided insight into basic structure of enamel and dentin and also modulus values under different strain condition. A research study by Zeravaki, et al. [9] revealed the microhardness of tooth enamel as 307 Hv and that of dentin to be 43 Hv, thus they concluded the hardness and modulus values varied with depth. The hardness of enamel was found to be around 3.5 GPa (~356.9 Hv) and that of interior dentin to be 1.5 GPa (~153 Hv) by Roy, et al. [4]. They also reported that the variation in hardness values is partially dependent upon the mineral concentration in enamel and dentin, with a possible dependence also on local microstructural features such as enamel rod orientation and dentinal tube density. The microsturucture of human tooth plays a vital role in determining the mechanical properties like hardness, modulus, etc. [1]. The difference in hardness values of dentin and enamel is mainly due to difference in percentage of organic and inorganic materials in enamel and dentin and not due to the content of Na, Mg, or Cl [10]. The shark teeth were also studied by Whitenack, et al. [6] for their Young's modulus and mechanical properties and they conducted research on osteodentine (*c.taurus*) and orthodentine (*c. tiburo*). Both hardness and modulus values were higher for osteodentine than orthodentine. One reason explained is that the arrangement of tubules (i.e., macroanatomy) plays an important role in determining the hardness of the tooth. Also, the chemical composition varied in osteodentine and orthodentine; the earlier had more calcium content whereas the later had more sodium and phosphate percentage. The reported hardness values for shark tooth (3.20~3.53 GPa) fall within the range of mammalian hardness values. These studies provided insight into basic structure of enamel and dentin, and also modulus values under different strain conditions.

Experimental Approach

Multiscale structures and mechanical properties were quantified under different length scales by using top and bottom teeth of king bream. The enamel and dentin layers of the king bream teeth were observed by using a scanning electron microscope (SEM), and their chemical compositions were analyzed by an energy dispersive x-ray (EDX) spectroscopy technique, respectively. X-ray computed tomography (CT) was also carried out to observe the internal structure of the bream tooth. The x-ray CT was conducted by using a v|tome|x by phoenix|x-ray. Mechanical tests in this research included nano-indentation tests. In nano-Indentation tests, indentations were particularly made in a specific region of enamel and dentin to gain knowledge about the modulus and hardness of the respective regions. These

tests were performed with Hysitron® TriboIndenter at room temperature using a Berkovich type indenter under load control that included a 20 second loading segment, a 5 second constant load hold time, and a 20 second unloading segment. A 1000 µN force was used and the unloading segment was used for analyzing the hardness and the reduced modulus values of the tooth at the region of indenting point.

Experimental Results

The internal structure and porous nature of bream tooth was studied using X-ray CT and the images are provided in Figure 1. When viewed from the frontal face, the bream tooth showed unleveled upper topography. As depicted in Figure 1 (b), the upper surface has a raised portion on the outer edge of tooth.

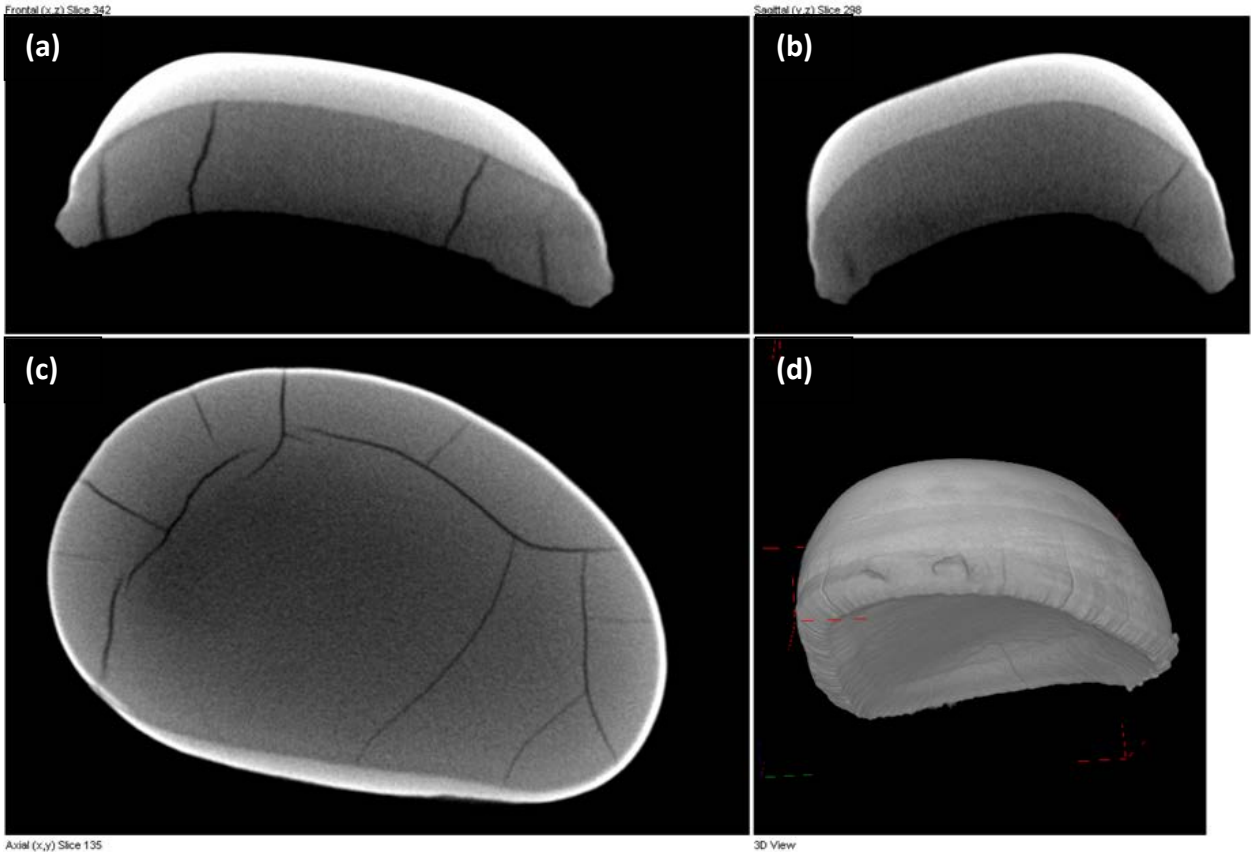

Figure 1. X-ray CT images of bottom bream tooth; (a) sagittal view, (b) Frontal, (c) Axial, and (d) 3D view.

Figure 2 shows the chemical analysis results obtained from various surfaces of the bream tooth. The results of EDX spectroscopy performed on entire enamel showed that the enamel mostly consists of oxygen (O), carbon (C), fluorine (F), calcium (Ca), and phosphorous (P). Small amounts of potassium (K) and sodium (Na) were also traced. The presence of all these elements is justifiable because of the bream's aquatic inhabitance. The chemical analysis results for whole dentin showed the presence of C, O, P, Na, and Ca. The analysis of chemical composition on human tooth enamel showed that the wt % of CaO and P_2O_5 decreased from outer rim of enamel to dentin-enamel junction (DEJ) [10]. The chemical analysis results obtained from different regions of dentin and DEJ are shown in Figure 2 (c) and (d),

respectively. The localized tests mainly showed the presence of C, O, Ca, and P. A research on hardness of different shark species by Whitenack, et al. [6] showed that the microanatomy of dentinal tubules could affect the hardness values considerably, thus the mineral content and microanatomy are mainly responsible for varying hardness in fish tooth.

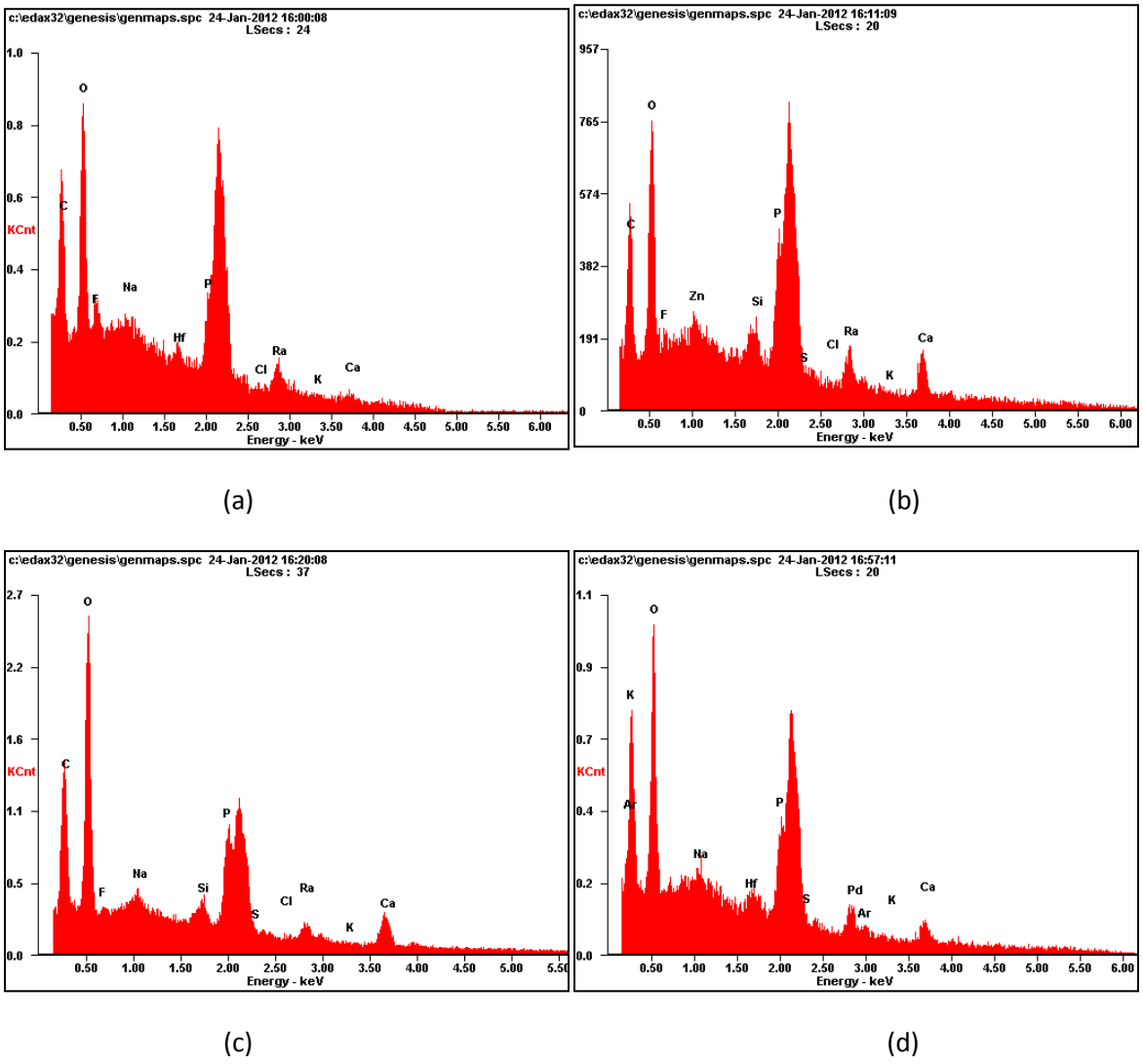

Figure 2. Chemical analysis results obtained from different surfaces of King Bream tooth; (a) enamel, (b) DEJ, (c) region right below DEJ, (d) dentin.

Figure 3 shows the nano-indentation test results on the King Bream tooth. The hardness and reduced elastic modulus (Er) values obtained from enamel layer decreased from outer surface to DEJ whereas those from dentin layer showed comparable values. Similar trends in the hardness profile have also been observed from micro-indentation tests in prior studies. The micro-hardness values of human tooth also decrease with the depth [4,10].

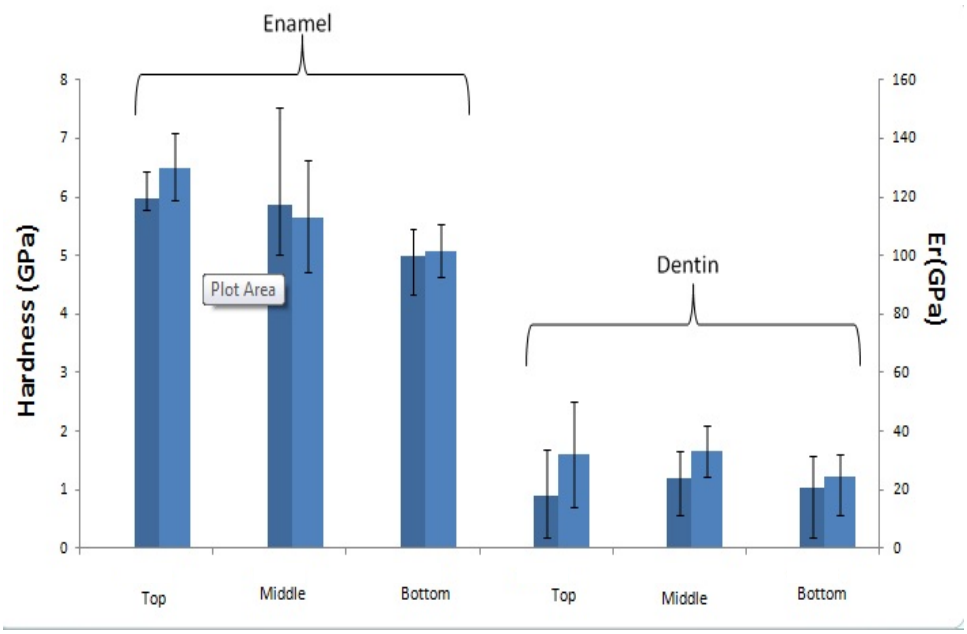

Figure 3. Nano-Indentation test results obtained from the bottom bream tooth.

References

1. H.H.K. Xu, D.T. Smith, S. Jahanmir, E. Romberg, J.R. Kelly, V.P. Thompson, E.D. Rekow, "Indentation damage and mechanical properties of human enamel and dentin," *J. Dent. Res.* 77 (1998) 472-480.
2. L.H. He, M.V. Swain, "Understanding the mechanical behavior of human enamel from its structural and compositional characteristics," *Journal of the Mechanical Behavior of Biomedical Materials I* (2008) 18-29.
3. D. Bajaj, D.D. Arola, "On the R-curve behavior of human tooth enamel," *Biomaterials* 30 (2009) 4037-4046.
4. S. Roy, B. Basu, "Mechanical and tribological characterization of human tooth," *Materials Characterization* 59 (2008) 747-756.
5. J. Malinowska, "Mechanical properties of human tooth approximated with overdamped oscillators," *Acta of Bioengineering and Biomechanics*, 7 (2005) 59-67.
6. L.B. Whitenack, D.C. Simkins Jr., P.J. Motta, M. Hirai, A. Kumar, "Young's modulus and hardness of shark tooth biomaterials," *Archives of Oral Biology*, 55 (2010) 203-209
7. I. Sasagawa, M. Ishiyama, H. Yokosuka, M. Mikami, T. Uchida, "Tooth enamel and enameloid in actinopterygian fish," *Front. Mater. Sci. China*, 3 (2009) 174-182.
8. J. Song, C. Ortiz, M.C. Boyce, "Threat-protection mechanics of an armored fish," *Journal of the Mechanical Behavior of Biomedical Materials*, 4 (2011) 699-712.
9. A. Zervaki, G.N. Haidemenopoulos, A. Giannakopoulos, "On the microhardness and Young's modulus of human teeth," *Proc. Int. Conference on Manufacturing Engineering (ICMEN)*, Thessaloniki, Greece, 1-3 October, 2008.
10. M. del P. Gutierrez-Salazar, J. Reyes-Gasga, "Microhardness and chemical composition of human tooth," *Materials Research*, 6 (2003) 367-373.
11. J.R. Paxton, W.N. Eschmeyer, *Encyclopedia of Fishes*, Academic Press, San Diego, CA (1998).

PUBLICATIONS/PRESENTATIONS

A publication in preparation: Energy Absorption Structure-Property Relationships of the Melanerpes Carolinus (Red-bellied Woodpecker) Beak

ACTIONS PLANNED FOR THE NEXT QUARTER

1. ***Lung Tissue***: Future studies will include histological analysis, which will provide us with a better understanding of the structure-property relationship & ultimately provide input for our multi-scale computational models
2. ***Woodpecker Beak***: Run the finite elements simulations on the wavy line, which is shown at the woodpecker beak, and examine the energy absorbing capacity with respect to geometry.
3. ***Bream Teeth***: Mesh generation of bream tooth for finite element simulations.

SUBTASK 3.5: CYBERINFRASTRUCTURE

Please refer to Task 1, Subtask 1.2 Report.

SUBTASK 3.6: DESIGN OPTIMIZATION

Please refer to Task 1, Subtask 1.6 Report.

MISSISSIPPI STATE UNIVERSITY

Southern Regional Center for Lightweight Innovative Design

Phase IV
Quarterly Report
January – March 2012

For compliance with contract requirements of
Award DE-FC26-06NT42755

TASK 4
K-12 OUTREACH PROGRAM

Submitted April 30, 2012

TABLE OF CONTENTS

Center for Advanced Vehicular Systems, Mississippi State University

Date: April 30, 2012

From: Paul Wang, Mark Horstemeyer

RE: SRCLID Phase IV Quarterly Report – January-March 2012

TASK 4: K-12 OUTREACH PROGRAM

Principal Investigator: N. Eric Heiselt
Director, Outreach and Support Programs
Bagley College of Engineering
Mississippi State University (MSST)
Box 9544
Mississippi State, MS 39762
(662) 325 - 1360; fax: (662) 325-8573; *e-mail:* nericheiselt@bagley.msstate.edu

Carol Schutte: Technology Area Development Manager
e-mail: carol.schutte@ee.doe.gov

Joseph Renk: Project Officer
email: joseph.renk@netl.doe.gov

Contractor: *Mississippi State University (MSST)*
Contract No.: *DE-FC26-06NT42755*

***Team Members:* N.E. Heiselt**, *M.F. Horstemeyer*

SUMMARY OF THE PROGRESS

1. Last competitions held in December. One hundred sixty-two students competed.
2. SAE is planning to use the Mission Eggcellence Program in their "World in Motion" Program. Contact with SAE is ongoing.

ACTIONS PLANNED FOR THE NEXT QUARTER

1. Working with SAE.